UNIVERSITY OF CALIFORNIA,

IRVINE

Uncovering Minimal Pathways in Melanoma Initiation

DISSERTATION

Submitted in partial satisfaction of the requirements for the degree of

DOCTOR OF PHILOSOPHY

in Mathematical, Computational, and Systems Biology

by

Karen Hui Xiao

Dissertation Committee:

Professor Anand K. Ganesan, Chair

Professor John S. Lowengrub

Professor Xing Dai

2025

DEDICATION

To God, through whose grace everything was made possible.

To my husband, Jalen Jiaming Liu, whose love and support have been my anchor.

TABLE OF CONTENTS

LIST OF FIGURES

LIST OF TABLES

ACKNOWLEDGEMENTS

I would like to dedicate this section to thank the people and resources made all the work possible. First and foremost, I would like to thank my Ph.D. advisor, **Dr. Anand K. Ganesan,** for his continuous support and guidance, not only in science but also in life. I joined the Lab in the summer of 2020, a difficult time amongst the first few months of the covid outbreak. I thank him for being willing to taking me in, as a fourth rotation student who had a hard time finding a lab, with very little knowledge about mouse work, sequencing, or cancer biology. I thank him for his patience and guidance shaping me as a skin cancer researcher and bioinformatician I am today, for always encouraging me and giving me opportunities to present my work at conferences, for spoiling me and letting me go skiing during the winter season, and for not only being a great mentor but also a passionate scientist that I always look up to.

The members of the Ganesan Lab have been amazing and supportive in every way throughout my PhD journey. I deeply thank each one of them for their kindness, collaboration, and encouragement, which have contributed immensely to my growth as a researcher. First, I would like to thank **Chi-Fen Chen,** who has been my "lab mom" since my very first day in the lab. Chi-Fen has taught me so much valuable knowledge in the field of cell biology, and introduced me to the world of mouse work, where my literal nighttime dreams of chasing mice in lab originated. She was always there for me whenever I encountered problems I couldn't solve on my own. I am grateful to Chi-Fen for her genuine care and unwavering support. Her optimism in life has been a constant source of inspiration. I thank **Dr. Jessica Shiu** for being my personal Cantonese coach and a role model of how to balance being an independent scientist and junior faculty. Collaborating with Jess has been an incredible experience, and I will always remember the times we worked together until 8pm long flow cytometry runs and the massive tumor measurement sessions.

I am also deeply grateful to **Dr. Rolando Ruiz-Vega**, a former graduate student in the lab and later a collaborator at the Lander Lab. Rolando, together with Chi-Fen, started the melanoma mouse model project in Chapter 2 long before I joined. He patiently guided me through the Bioinformatics basics, helping me build the foundational skills needed for a Bioinformatician. Although our time working together was brief, Rolando always made himself available to answer my questions, even after leaving UCI, and often checked in to ensure I was on the right track. His support has been invaluable to my growth as a researcher. I would like to thank **Sahil S. Telang**, now an MD candidate at USC, for being a great co-worker during his gap years in our lab. Sahil worked closely with Jess and me, formed our very own mouse harvest "assembly-line", and contributing his remarkable skills, intelligence, and collaborative spirit to our project.

I thank **Terry Nguyen** and **Dr. Sohail Jahid** for their help when I first joined the lab. Their guidance and assistance during those early days made the transition smoother and helped me find my footing in a new environment. I thank **Dr. Linh M. Vuong** and **Noel Salvador** for their creativity and enthusiasm in coming up with ideas for lab activities such as the anti-cancer challenge and CRI annual baking competition. Their efforts created so many fun memories for the Ganesan Lab, fostering a sense of camaraderie and making the lab a truly enjoyable place to work. I thank **Dr. Katie Hinchee-Rodridguez** and **Dr. Hira Rizwi** for always being willing to help me check Dr. Ganesan's availability schedule when I could not find him. Also, as physicians, they were always willing to provide me with clinical insights on various matters, which greatly enriched my perspective and understanding of my research.

Dr. Jenny Jie Wu from the UCI GRT Hub also provided tremendous guidance and support in the data analysis aspects of my project. She was always kind and patient, willing to sit down with me to address the reviewers' concerns and work through complex challenges. This project would not have been possible without Jenny's invaluable expertise in genomics and bioinformatics, and I am incredibly thankful for her contributions.

I thank the funding agencies throughout my PhD journey, including National Institutes of Health (NIH, CA217378) and California Institute for Regenerative Medicine (CIRM, EDUC4-12822). I thank the UCI core facilities, including GRT Hub, the Beckman Laser Institute, and the Stem Cell Center. My work would not have been possible without the invaluable resources provided by them.

I am deeply grateful to my collaborators, **Dr. Arthur D. Lander**, **Dr. Qing Nie**, and **Dr. Peijie Zhou**, for their expertise in systems biology and computational biology, which greatly enriched this project. I also thank my committee members: **Dr. Xing Dai, Dr. John S. Lowengrub,** Dr. Roberto Tinoco, and Dr. Min Zhang, for their constructive feedback on the project. Additionally, I am thankful to **Dr. Bogi Anderson** and **Dr. Peter Donovan** for their support and guidance during my CIRM training period. I would like to thank my home department CCBS (Dr. Emi Embler, Karen Y. Martin, Austin Berryman, Caroline Vu, Tina Rimal) and Abbie Enriquez from the Stem Cell Center, for their help on logistics and administrative matters through my PhD journey.

As I wrap up my PhD journey, I would like to thank the mentors who guided and inspired me at an earlier stage of my life. I am thankful for Mr. Bob Rip, my high school AP Biology teacher, whose fun lab sessions sparked my interest in Biology and led me to major in it during my undergraduate studies. Mr. Rip's recognition of my potential, through awarding me the "Outstanding Student in Science of the year", had planted the seed of becoming a scientist in my mind. I also extend my heartfelt thanks to my undergraduate research advisor, **Dr. Zhefeng Guo**, for taking me in as an undergraduate Bio99 student, teaching me essential hands-on skills, fostering a critical and independent scientific mindset, and encouraging me through the graduate school application process. His mentorship and support were instrumental in my admission to graduate school, and for that, I am forever thankful.

Finally, I thank my family and friends. I thank my husband, **Jalen Jiaming Liu**, for his understanding for my long working hours, sudden change of experimental plans, and unpredictable graduation timeline. I thank him for patiently waiting for me for the past eight years, first to graduate undergrad, then to apply for graduate school, and finally now to graduate my PhD. I thank him for always putting me first in his life, for being my rock, and shaping me into a better person. Words cannot express how grateful I am. I simply could not do this without him. I thank my aunt **Denise Dan Xiao**, for taking care of me from day-to-day throughout high school and encouraging me coming to the U.S. to study in the first place. I thank my middle school besties **Zoe Wang, Jenny Meng, Rose Tong,** and **Juli Zhu**, who still managed to care for me even being far apart in five different time zones. I thank my high school, college, and grad school friends **Cathy Luo, Elaine Li, Shirley You, Zheming He,** and **Lulu Lai**, for their continuing support. Specially, I have been deeply grateful for **Dr. Cindy Cheng**, **Dr. Junyan Duan**, and **Dr. Joann Chen**, for sharing this PhD journey with me and understanding my frustrations and joy as graduate students. I also thank my two tabbies, **Bolo** and **Yumi**, who brought endless joy to our family.

The past five and a half years have been challenging yet absolutely rewarding, and I am deeply thankful to those who have believed in me along the way. Your unwavering support has been my greatest motivation. As I move on to the next chapter of my life, I will always remember the journey that brought me here, and I dedicate this achievement to you all.

VITA
Karen Hui Xiao

EDUCATION

- **University of California, Irvine** *2025*
  Ph.D.: Mathematical, Computational, and Systems Biology Irvine, CA
- **University of California, Los Angeles-Extension** *2019*
  Certificate Program: Systems Analysis Los Angeles, CA
- **University of California, Los Angeles** *2018*
  B.S.: Biology Los Angeles, CA

RESEARCH EXPERIENCE

- **Dr. Anand Ganesan's Laboratory at UC Irvine** *2020 - 2024*
  Graduate Student Researcher Irvine, CA
  - Conducted **DNA-sequencing**, **Single-cell RNA-sequencing** , and **Spatial transcriptomics** to investigate **tumorigenesis** in mouse melanoma models
  - Performed extensive **Bioinformatic** analysis on **gene signature comparisons**, **RNA velocity**, and **transition states**, revealing the underlying cellular transitions
  - Identified a distinct cell type termed LNM (Low-pigment, Neural, and Matrix-enriched) that might serve as a potential **non-genetic transition** in tumor formation
  - Examined the role of **immune cells** and **endothelial** cells in the tumor microenviornment (TME) by identifying potential **ligand-receptor** interactions.
- **Dr. Zhefeng Guo's Laboratory at UCLA** *2017 - 2019*
  Undergraduate Student Researcher Los Angeles, CA
  - Executed comprehensive **structural analysis** of **Aβ40 protein** associated with **Alzheimer's disease** using site-directed spin labeling and EPR spectroscopy
  - Characterized static and dynamic disorder across fibril residues, pinpointing highly ordered regions essential for understanding fibril stability
  - Revealed more ordered packing in Aβ40 fibrils compared to Aβ42, highlighting significant C-terminal disorder in Aβ42 protein

PUBLICATIONS

[1] **Xiao, H.**, Shiu, J., Chen, C. F., Wu, J., Zhou, P., Telang, S. S., Ruiz-Vega, R., Nie, Q., Edwards, R. A., Lander, A. D., Ganesan, A. K. (2024). **Uncovering Minimal Pathways in Melanoma Initiation**. *Nature Communications*, under revision. DOI: 0.1101/2023.12.08.570336

[2] **Xiao, H.**, Duo, L., Zhen, J., Wang, H., Guo, Z. (2021). **Static and dynamic disorder in Aβ40 fibrils**. *Biochemical and Biophysical Research Communications*, 610, 107–112. DOI: 10.1016/j.bbrc.2022.04.036

[3] Cui, Y., Cui, Z., Xu, J., Hao, D., Shi, J., Wang, D., **Xiao, H.**, Duan, X., Chen, R., Li, W. (2020). **NG-Circos: next-generation Circos for data visualization and interpretation**. *NAR genomics and bioinformatics*, 2(3), lqaa069. DOI: 10.1093/nargab/lqaa069.

ORAL PRESENTATIONS

[1] Xiao, H. ***Uncovering Minimal Pathways in Melanoma Initiation***
- Society of Investigative Dermatology (SID), Dallas, TX *May 2024*

[2] Xiao, H. ***Uncovering Core Cell Lineages that Generate Melanoma Tumors***
- International Pigment Cell Conference (IPCC), Bilbao, Spain *May 2023*

[3] Xiao, H. ***Identifying Signaling Networks in Melanoma Tumors that Promote the Uncontrolled Growth of Braf Mutant Melanocytes***
- Society of Investigative Dermatology (SID), Portland, OR *May 2022*
- CSBC/PS-ON/BD-STEP NCI Junior Investigator Meeting, Remote *Aug 2022*

[4] Xiao, H. ***Single-cell Transcriptomics Revealed Potential Cell-cell Communications in Mouse Melanoma Tumor Microenvironment***
- SoCal Systems Biology Symposium, Los Angeles, CA *Apr 2022*

Poster Presentations

[1] **Xiao, H.**, Shiu, J., Chen, C. F., Wu, J., Zhou, P., Telang, S. S., Ruiz-Vega, R., Nie, Q., Lander, A. D., Ganesan, A. K.
Uncovering Minimal Pathways in Melanoma Initiation
- Society of Investigative Dermatology (SID), Dallas, TX *May 2024*

[2] **Xiao, H.**, Shiu, J., Chen, C. F., Wu, J., Zhou, P., Telang, S. S., Ruiz-Vega, R., Nie, Q., Lander, A. D., Ganesan, A. K.
Uncovering Core Cell Lineages that Generate Melanoma Tumors
- CSBC Annual Investigators Meeting, Denver, CO *Mar 2023*
- UCI Annual Skin Symposium, Irvine, CA *Jan 2024*

[3] **Xiao, H.**, Shiu, J., Chen, C. F., Wu, J., Telang, S. S., Ruiz-Vega, R., Lander, A. D., Ganesan, A. K.
Identifying Signaling Networks in Melanoma Tumors that Promote the Uncontrolled Growth of Braf Mutant Melanocytes
- Society of Investigative Dermatology (SID), Portland, OR *May 2022*
- CSBC/PS-ON/BD-STEP NCI Junior Investigator Meeting, Remote *Aug 2022*
- UCI Annual Skin Symposium, Irvine, CA *Jan 2023*

[4] **Xiao, H.**, Shiu, J., Chen, C. F., Wu, J., Telang, S. S., Ruiz-Vega, R., Lander, A. D., Ganesan, A. K.
Characterizing the Role of Cell-cell Communications in Mouse Melanoma Tumorigenesis Using Single-cell Transcriptomics
- CSBC/PS-ON/BD-STEP NCI Junior Investigator Meeting, Remote *Aug 2021*
- PASPCR Annual Meeting, Lexington, KY *Sept 2021*
- Southern California Systems Biology Symposium, Los Angeles, CA *Apr 2022*

[5] Lander, A. D., **Xiao, H.**, Caldwell, M., Ruiz-Vega, R., Shiu, J., Chen, C., Ganesan, A. K.
Mice, Moles, and Melanoma: Probing the Origins of Cancer
- CSBC Annual Meeting, Remote *Sept 2021*

[6] Shiu, J., **Xiao, H.**, Ruiz-Vega, R., Chen, C., Lander, A. D., Ganesan, A. K.
Flow Cytometry and Single-Cell Transcriptomics Reveal Enrichment of Trem2-Expressing Macrophages in Melanoma
- CSBC/PS-ON/BD-STEP NCI Junior Investigator Meeting, Remote *Aug 2021*

Fellowships and Awards

- California Institute of Regenerative Medicine (CIRM) **Predoctoral Fellowship** *2022-2024*
- UC Irvine Associated Graduate Students Conference Travel Award *2023*
- People's Choice Award, *NCI Junior Investigator Annual Meeting* *2022*
- Dean's Honors list, *UCLA* *2018*
- Valedictorian, *Ontario Christian High School* *2014*

Teaching Experience

- **Teaching Assistant** *2021-2022*

  UCI California State Summer School for Mathematics and Science (COSMOS)Program
  - Taught 90-minute lectures on **Cancer Biology** and **Computational Biology** to high school students during the summer program
  - Assisted students in preparing for their final scientific poster presentations
  - Facilitated discussions and learning in break-out rooms, encouraging active engagement and understanding
- **Learning Assistant** *2016 - 2018*

  UCLA Life Sciences Department
  - Supported instruction for LS23L: Introduction to **Laboratory and Scientific Methodology**
  - Presented mini lectures on course material and developed exam questions to enhance student comprehension
  - Fostered student learning by engaging in interactive discussions during lab sections

ABSTRACT OF THE DISSERTATION

Uncovering Minimal Pathways in Melanoma Initiation

by

Karen Hui Xiao

Doctor of Philosophy in Mathematical, Computational, and Systems Biology

University of California, Irvine, 2025

Professor Anand K. Ganesan, Chair

Melanomas are genetically heterogeneous, displaying MAP kinase mutations and homozygous loss of tumor suppressor genes. Mouse models combining such mutations produce fast-growing tumors. In contrast, rare, slow-growing tumors arise in mice combining *Braf* activation with heterozygous loss of *Pten* or, as we show here, in albino mice bearing only a *Braf* mutation. Incidence kinetics suggest a stochastic event underlies tumorigenesis, yet de novo mutations or structural variants that could explain the incidence of most tumors could not be found. Single-cell transcriptomics of tumors identified a cell type resembling “neural crest-like” cells in human and mouse melanomas. These exist in normal mouse skin, expand upon *Braf* activation, and persist through serial transplantation; analyses of gene expression suggest they serve as precursors of malignant cells. This state may serve as an intermediate on a slow path to malignancy that may provide a diagnostically and therapeutically important source of cellular heterogeneity.

CHAPTER 1: INTRODUCTION

Melanoma: Causes, Treatment, Mouse models, and Heterogeneity

Karen Hui Xiao and Anand K. Ganesan

An Overview of Melanoma

Melanoma is the most aggressive form of skin cancer, arising from the uncontrolled proliferation of melanocytes—the pigment-producing cells located in the basal layer of the epidermis[1]. Although melanoma accounts for a relatively small proportion of skin cancer cases, it is responsible for the majority of skin cancer-related deaths due to its high aggressiveness[1]. It can occur anywhere on the body, including areas not typically exposed to the sun, such as the soles of the feet, palms of the hands, and mucous membranes[1]. The pathogenesis of melanoma involves both genetic predisposition and environmental risks[1-2].

The primary environmental risk factor for melanoma is UV radiation, with intermittent or chronic sun exposure leading to sunburns being particularly detrimental[2]. The global incidence of melanoma varies widely, with the highest rates occurring in regions where fair-skinned populations are exposed to significant ultraviolet (UV) radiation, such as Australia and New Zealand[2-3].

Early detection greatly improves the 5-year survival rate. However, the prognosis declines sharply once the disease metastasizes to distant organs, with the 5-year survival rate being 99% in localized melanoma, and only 32% in metastatic melanoma[3-5]. These statistics underscore the urgent need for prevention, early diagnosis, and effective treatments. Recent research has revealed the critical roles of genetic mutations, tumor microenvironment interactions, and immune evasion mechanisms in disease progression[1-3]. However, whether genetic mutation is the only pathway remains uncertain. A comprehensive understanding of melanoma tumorigenesis is essential to uncover alternative pathways. This study aims to contribute to this growing body of knowledge by examining whether melanoma initiation really always requires new mutations and whether it can be initiated by non-genetic transitions. Understanding these transitions may provide additional insight and inform future therapeutic development.

Clinical Diagnosis and Staging

Melanoma typically presents as a new or evolving skin lesion, often arising from an existing mole. The ABCDE criteria—Asymmetry, Border irregularity, Color variation, Diameter greater than 6 mm, and Evolution over time—serve as a widely recognized diagnostic guideline for identifying suspicious lesions[5-7]. Additional concerning features include lesion elevation, firmness, and rapid growth, which may indicate a more aggressive phenotype [6-7].

Clinically, melanoma staging follows the TNM classification system, which evaluates three critical factors: Tumor (T), describing the thickness and ulceration characteristics of the lesion; Nodes (N), determining if cancer has spread to the lymph nodes; and Metastasis (M), identifying distant spread status[8]. The TNM system helps to clinically stage patients from early localized disease (Stage I) to advanced metastatic melanoma (Stage IV), which directly influences prognosis and treatment decisions[8].

Genetic Mutations in Melanoma

Melanoma tumorigenesis is multifactorial, driven by a combination of genetic, epigenetic, and environmental factors. All together, these factors lead to its rapid progression and high metastasis potential[9]. Though hereditary melanomas are rare, most melanomas have a high number of somatic mutations[9]. Large-scale sequencing technologies have enhanced the study of melanoma mutations, providing a comprehensive view of its genetic landscape.

Among the most frequently driver mutations include *BRAF*, *NRAS*, and *KIT*, all of which play critical roles in activating the mitogen-activated protein kinase (MAPK) pathway, a central driver of cell proliferation and survival[10]. The MAPK pathway is the most disrupted signaling pathway in cutaneous melanoma, with abnormal activation occurring in up to 90% of cases[9-10].

BRAF mutations, particularly the V600E variant are present in approximately 50% of cutaneous melanomas[11]. This mutation results in a valine (V) to glutamic acid (E) substitution at position 600[11]. Similarly, *NRAS* mutations are found in approximately 15-20% of melanomas, also frequently resulting in missense mutations affecting codon 61[9-12]. *KIT* mutations are more common in acral and mucosal melanomas, which are less associated with UV exposure, but still drive oncogenic pathways[12]. Frequent mutations found in these genes led to the development of kinase inhibitors targeting the MAPK pathway as a treatment for melanoma[12-13].

Whole exome sequencing (WES) studies have revealed a large share of the mutations are C>T transitions at dipyrimidine sites, a UV signature found commonly in primary and metastatic melanomas, suggesting UV exposure is a key driver of somatic mutations[12, 14]. On the other hand, Whole genome sequencing (WGS) has enabled the identification of important non-coding regions, which may play regulatory roles in melanoma development[14]. More specifically, the comprehensive WGS study by Hayward and colleagues identified unique genomic landscapes in major melanoma subtypes[17]. Cutaneous melanoma exhibited a high UV mutational burden, frequently harbor *BRAF*, *NRAS*, *CDKN2A*, and *TP53* mutations, whereas acral and mucosal melanomas are less associated with UV radiation but displayed more structural variations and chromosomal rearrangements[17]. Besides these, TERT promoter mutations were the most prevalent non-coding mutation amongst all[17]. These findings emphasize the complexity of melanoma tumorigenesis, where both coding and non-coding mutations, along with distinct mutational processes across subtypes contributing to its heterogeneity, making it challenging to pinpoint universal drivers and therapeutic targets.

Despite these advances, there are still several challenges in using genomic data to fully understand melanoma. One issue is tumor heterogeneity, meaning tumor composition might vary within different regions of the same tumor or due to intrinsic differences between patients, making it difficult to pinpoint universal drivers [9,11]. Without understanding the fraction of cells

that are actually tumors, it is difficult to know whether a particular mutation identified is really strictly in the tumor cells themselves. Second, there is a syllogism between a mutation being present at a particular fraction and its requirement for being involved in initiating tumors. For example, a mutation may be acquired late in tumorigenesis, and then accumulate in tumors but that does not necessarily mean it causes the tumors to form or even that it promotes the growth of melanoma. This sort of syllogism has generated an abundance of confusion in the field as to what mutations cause melanoma. Finally, it is important to recognize how much of the genome we do not know about. It is well established that many of the mutations identified through WGS occur in non-coding regions of the genome, and their biological significance is often unclear [11].

Epigenetic Modifications in Melanoma

Besides these driver mutations, epigenetic modifications such as DNA methylation and histone acetylation can also affect melanoma progression, regulating gene expression without altering the DNA sequence[18-20]. Hypermethylation of tumor suppressor gene promoters, such as *CDKN2A*, leads to gene silencing, resulting in uncontrolled cell proliferation and evasion of apoptosis[18]. On the contrary, global hypomethylation can activate oncogenic pathways and promote genomic instability[18-20]. These DNA methylation alterations are critical in melanoma pathogenesis [18-20].

Histone modifications, such as acetylation and methylation, regulate chromatin structure and gene expression, and can therefore also impact melanoma progression[21]. For example, aberrant histone methylation H3K27me3 is frequently observed in melanoma and is linked to tumor progression and poor prognosis[22]. As noted above, many of these modifications are not detected by WES, and may not be easily detected by WGS depending on sequencing coverage.

Treatment Strategies

Early detection and accurate diagnosis are vital for effective treatment, as the prognosis of melanoma is closely linked to the stage at which it is diagnosed[23]. For localized early-stage

melanomas, surgical excision remains the main treatment, where lesions are removed surgically with adequate margins to reduce recurrence[24]. In these localized cases, surgery can be highly effective, particularly when combined with sentinel lymph node biopsy to assess the spread of the disease[24].

For advanced melanoma, where the cancer cells already spread to lymph nodes and distant organs, targeted therapies have become crucial, especially for tumors harboring specific mutations like *BRAF*^{V600E}.[24] Drugs such as *BRAF* inhibitors (vemurafenib, dabrafenib) and MEK inhibitors (trametinib) are designed to block the MAPK/ERK pathway, which is often activated in melanoma[24-25]. These therapies have significantly improved survival rates, though resistance can develop over time, necessitating further research into more effective combinations and new targets[16].

Immunotherapy has also shed lights on the treatment of melanoma, especially for cases that are metastatic or cannot be surgically removed[24]. Immune checkpoint inhibitors, such as pembrolizumab and nivolumab (targeting PD-1) and ipilimumab (targeting CTLA-4), boost the immune system's capacity to identify and eliminate cancer cells[24]. While these therapies have led to durable responses in some patients, not every patient responds, and researchers continue to investigate ways to improve response rates and overcome resistance[24].

Melanoma Mouse Models

Mouse models are invaluable for studying melanoma, providing researchers with a controlled environment to explore tumorigenesis, metastasis, and therapeutic responses. These models also enable the generation of reliable tumors, thus facilitating the studies of melanoma[26]. Genetically Engineered Mouse Models (GEMMs) are designed to replicate the genetic mutations commonly observed in human melanoma, such as mutations in *BRAF*, *NRAS*, and *PTEN*[26]**.** One prominent GEMM is the Bosenberg model (Tyr::CreER; *Braf*^{CA}; *Pten*$^{\Delta/\Delta}$), which combines a

conditional *Braf*^{V600E} mutation with *Pten* loss[27]. This model closely mimics the development and progression of human melanoma, including metastasis, within an immunocompetent environment[27].

Other GEMMs include the HGF/SF transgenic mouse model, which overexpresses hepatocyte growth factor/scatter factor (HGF/SF), leading to the development of UV-induced melanoma. This model is useful for studying environmental risk factors, such as UV radiation, and how they interact with genetic predispositions[28]. Additionally, *NRAS* -driven melanoma models, such as the *Tyr*:: *NRAS*^{Q61K} mouse, are used to study the effects of *NRAS* mutations, which are present in approximately 20% of human melanomas[29].

Besides GEMMs, Patient-Derived Xenograft (PDX) models involve direct implantation of melanoma tissues from patients into mice, preserving the tumor's histological and genetic characteristics[30]. These models are valuable for preclinical drug testing and identifying resistance mechanisms, making them more predictive of clinical outcomes.[30]

Braf **mutation in Growth-arrested Nevi and Melanoma**

The *BRAF*^{V600E} mutation is prevalent in both melanocytic nevi (moles) and melanomas, yet these lesions exhibit markedly different behaviors[9,33]. Approximately 80% of benign nevi harbor the *BRAF*^{V600E} mutation, which initiates melanocyte proliferation but typically leads to a stable, growth-arrested state. In contrast, about 50% of melanomas carry the same mutation, resulting in uncontrolled cell proliferation and malignancy[31-32].

Traditionally, the arrest in nevi growth has been attributed to oncogene-induced senescence (OIS), a cell-autonomous mechanism where the oncogenic mutation triggers a permanent cessation of cell division[34]. Along the same line, melanoma tumorigenesis is also proposed as a multi-step model, where the *BRAF V600E* mutations, common in benign nevi, drive initial melanocyte proliferation but induce OIS and stop growing. Progression to melanoma requires

additional mutations, such as *CDKN2A* loss, *PTEN* deletion, or *TERT* promoter activation, which bypass OIS and allow tumors to form[9,33].

However, recent studies have challenged this notion: previous study from our lab utilized a mouse model to investigate *BRAF*-driven nevus formation and found no significant evidence of senescence markers in nevus cells compared to other skin cells[35]. Their findings suggest that growth arrest in nevi may result from collective cell behavior and intercellular interactions rather than intrinsic senescence mechanisms[36].

Complementing this perspective, McNeal et al. examined human melanocytes and proposed that external environmental cues such as TPA, rather than cell-intrinsic factors, play a pivotal role in halting the proliferation of *BRAF*-mutant melanocytes[37]. Their research indicates that signals from the surrounding tissue microenvironment contribute to the growth arrest observed in nevi, providing an alternative explanation to the OIS model[37].

Finally, it is important to highlight an additional flawed piece of the OIS model. In the OIS model, for a tumor to arise, an arrested cell must accumulate additional mutations that allow it to escape growth arrest[9, 33-35]. If these cells are truly growth arrested, then they are not undergoing active DNA replication, and existing literature indicates that arrested cells have a very low likelihood of accumulating additional mutations[9, 33-35]. Thus, it is quite unlikely that they would accumulate new mutations to form melanoma. Why that maybe part of the reason the transformation of nevi to melanoma occurs at a very low rate, one must at least bring up the question as to whether these cells are really arrested and if their transformation requires a new mutation.

In conclusion, these studies collectively highlight the complexity of melanocyte behavior in the presence of oncogenic *BRAF* mutations. They underscore the importance of both cell-extrinsic factors and intercellular interactions in determining whether a melanocyte harboring a *BRAF*

mutation will enter a benign, growth-arrested state as in nevi, or progress to malignant melanoma.

Complex Melanoma Cell States and Heterogeneity

The advent of single-cell transcriptomics has revolutionized our understanding of cellular heterogeneity in melanoma. Several studies leveraging human melanoma samples, mouse models, and cell lines have identified distinct gene expression programs that define a spectrum of melanoma cell states[38-42]. These states have been variably categorized as pigmented, proliferative, invasive, neural crest (NC)-like, mesenchymal, intermediate, and *BRAF* inhibitor-resistant states, underscoring the phenotypic plasticity of melanoma cells[38-42].

This plasticity allows melanoma cells to transition between states, driving tumor progression and therapy resistance[38]. For instance, pigmented and proliferative states align with melanocytic differentiation, while invasive and mesenchymal states reflect dedifferentiation[38,40]. Intermediate states may serve as transitional populations, facilitating phenotypic switching[38]. Understanding these shifts is crucial for improving treatment strategies and predicting therapy responses. While these gene expression signatures provide a framework for understanding melanoma cell state heterogeneity, there is significant divergence among findings from different studies [41-42]. This inconsistency raises questions about whether these differences reflect true biological variability or are artifacts introduced by differences in methodologies[40].

While diverse cell states provide insights into melanoma heterogeneity, the ability of melanoma cells to shift between states may suggest that tumor initiation may occur in the absence of a new mutation. This suggestion, when coupled with a confusing literature that fails to elucidate a defined pathway to initiate melanoma tumors and the fact that any such mutation must occur in an arrested cell, at least raises the possibility that initiation may not require mutations in addition to *Braf*. This indicates that non-genetic factors, such as epigenetic modifications and

microenvironmental cues that could shape cell state transitions, need to be further explored to define their contribution to melanomagenesis. The following chapter focuses on whether mutations are indeed required for melanoma initiation and explores whether common cell states may be important in initiating melanoma tumors.

REFERENCES

1. Centers for Disease Control and Prevention. (2021). U.S. cancer statistics: Data visualizations. Retrieved from https://www.cdc.gov/cancer/uscs/dataviz/index.html

2. Whiteman, D. C., Green, A. C., & Olsen, C. M. (2016). The Growing Burden of Invasive Melanoma: Projections of Incidence Rates and Numbers of New Cases in Six Susceptible Populations through 2031. The Journal of investigative dermatology, 136(6), 1161–1171. https://doi.org/10.1016/j.jid.2016.01.035

3. American Cancer Society. (2024). Survival rates for melanoma skin cancer by stage. Retrieved from https://www.cancer.org/cancer/types/melanoma-skin-cancer/detection-diagnosis-staging/survival-rates-for-melanoma-skin-cancer-by-stage.html

4. Cancer Treatment Centers of America. (2024). Melanoma stages. Retrieved from https://www.cancercenter.com/cancer-types/melanoma/stages

5. international Agency for Research on Cancer (IARC). (2020). Globocan 2020 fact sheet: Melanoma of the skin. Retrieved from https://gco.iarc.who.int/media/globocan/factsheets/cancers/16-melanoma-of-skin-fact-sheet.pdf

6. Garbe, C., & Leiter, U. (2009). Melanoma epidemiology and trends. Clinics in dermatology, 27(1), 3–9. https://doi.org/10.1016/j.clindermatol.2008.09.001

7. Tsao, H., Olazagasti, J. M., Cordoro, K. M., Brewer, J. D., Taylor, S. C., Bordeaux, J. S., Chren, M. M., Sober, A. J., Tegeler, C., Bhushan, R., & Paller, A. S. (2015). Early detection of melanoma: Reviewing the ABCDEs. Journal of the American Academy of Dermatology, 72(4), 717–723. https://doi.org/10.1016/j.jaad.2015.01.025

8. Ogata, D., Namikawa, K., Takahashi, A., & Yamazaki, N. (2021). A review of the AJCC melanoma staging system in the TNM classification (eighth edition). Japanese journal of clinical oncology, 51(5), 671–674. https://doi.org/10.1093/jjco/hyab022

9. Shain, A. H., & Bastian, B. C. (2016). The genetic evolution of melanoma from precursor lesions. The New England Journal of Medicine, 374(20), 1926–1936. https://doi.org/10.1056/NEJMoa1502583

10. Gosman, L. M., Ţăpoi, D. A., & Costache, M. (2023). Cutaneous melanoma: A review of multifactorial pathogenesis, immunohistochemistry, and emerging biomarkers for early detection and management. International Journal of Molecular Sciences, 24(21), 15881. https://doi.org/10.3390/ijms242115881

11. Newell, F., Wilmott, J. S., Johansson, P. A., Nones, K., Addala, V., Mukhopadhyay, P., ... & Hayward, N. K. (2022). Comparative genomics provides etiologic and biological insight into melanoma subtypes. Cancer Discovery, 12(12), 2856–2879. https://doi.org/10.1158/2159-8290.CD-22-0603

12. Hodis, E., Watson, I. R., Kryukov, G. V., Arold, S. T., Imielinski, M., Theurillat, J. P., ... & Garraway, L. A. (2012). A landscape of driver mutations in melanoma. Cell, 150(2), 251–263. https://doi.org/10.1016/j.cell.2012.06.024

13. Akbani, R., Akdemir, K. C., Aksoy, B. A., Albert, M., Ally, A., Amin, S. B., ... & Bastian, B. C. (2015). Genomic classification of cutaneous melanoma. Cell, 161(7), 1681–1696. https://doi.org/10.1016/j.cell.2015.05.044

14. Cancer Genome Atlas Network. (2015). Genomic classification of cutaneous melanoma. Cell, 161(7), 1681–1696. https://doi.org/10.1016/j.cell.2015.05.044

15. Tsao, H., Chin, L., Garraway, L. A., & Fisher, D. E. (2012). Melanoma: From mutations to medicine. Genes & Development, 26(11), 1131–1155. https://doi.org/10.1101/gad.191999.112

16. Dahl, C., & Guldberg, P. (2007). The genome and epigenome of malignant melanoma. APMIS : acta pathologica, microbiologica, et immunologica Scandinavica, 115(10), 1161–1176. https://doi.org/10.1111/j.1600-0463.2007.apm_855.xml.x

17. Hayward, N. K., Wilmott, J. S., Waddell, N., Johansson, P. A., Field, M. A., Nones, K., ... & Scolyer, R. A. (2017). Whole-genome landscapes of major melanoma subtypes. Nature, 545(7653), 175–180. https://doi.org/10.1038/nature22071

18. Guo, W., Xu, T., Lee, J. J., Murphy, G. F., & Lian, C. G. (2015). Epigenetic markers in melanoma. Melanoma management, 2(4), 367–382. https://doi.org/10.2217/mmt.15.30

19. Micevic, G., Theodosakis, N. & Bosenberg, M. Aberrant DNA methylation in melanoma: biomarker and therapeutic opportunities. Clin Epigenet 9, 34 (2017). https://doi.org/10.1186/s13148-017-0332-8

20. Giunta, E. F., Arrichiello, G., Curvietto, M., Pappalardo, A., Bosso, D., Rosanova, M., Diana, A., Giordano, P., Petrillo, A., Federico, P., Fabozzi, T., Parola, S., Riccio, V., Mucci, B., Vanella, V., Festino, L., Daniele, B., Ascierto, P. A., Ottaviano, M., & On Behalf Of Scito Youth (2021). Epigenetic Regulation in Melanoma: Facts and Hopes. Cells, 10(8), 2048. https://doi.org/10.3390/cells10082048

21. Orouji, E., Utikal, J. Tackling malignant melanoma epigenetically: histone lysine methylation. Clin Epigenet 10, 145 (2018). https://doi.org/10.1186/s13148-018-0583-z

22. Zingg, D., Debbache, J., Schaefer, S. et al. The epigenetic modifier EZH2 controls melanoma growth and metastasis through silencing of distinct tumour suppressors. Nat Commun 6, 6051 (2015). https://doi.org/10.1038/ncomms7051

23. American Cancer Society. (2020). Cancer facts & figures 2020. American Cancer Society. https://www.cancer.org/research/cancer-facts-statistics/all-cancer-facts-figures/cancer-facts-figures-2020.html

24. Garbe, C., & Eigentler, T. K. (2007). Diagnosis and treatment of cutaneous melanoma: state of the art 2006. Melanoma research, 17(2), 117–127. https://doi.org/10.1097/CMR.0b013e328042bb36

25. Hauschild, A., Grob, J. J., Demidov, L. V., Jouary, T., Gutzmer, R., Millward, M., Rutkowski, P., Blank, C. U., Miller, W. H., Jr, Kaempgen, E., Martín-Algarra, S., Karaszewska, B., Mauch, C., Chiarion-Sileni, V., Martin, A. M., Swann, S., Haney, P., Mirakhur, B., Guckert, M. E., Goodman, V., … Chapman, P. B. (2012). Dabrafenib in BRAF-mutated metastatic melanoma: a multicentre, open-label, phase 3 randomised controlled trial. Lancet (London, England), 380(9839), 358–365. https://doi.org/10.1016/S0140-6736(12)60868-X

26. Pérez-Guijarro, E., Day, C. P., Merlino, G., & Zaidi, M. R. (2017). Genetically engineered mouse models of melanoma. Cancer, 123(S11), 2089–2103. https://doi.org/10.1002/cncr.30684

27. Dankort, D., Curley, D. P., Cartlidge, R. A., Nelson, B., Karnezis, A. N., Damsky, W. E., … & McMahon, M. (2009). Braf^V600E^ cooperates with Pten loss to induce metastatic melanoma. Nature Genetics, 41(5), 544–552. https://doi.org/10.1038/ng.356

28. Noonan, F.P., Dudek, J., Merlino, G. and De Fabo, E.C. (2003), Animal Models of Melanoma: An HGF/SF Transgenic Mouse Model May Facilitate Experimental Access to UV Initiating Events. Pigment Cell Research, 16: 16-25. https://doi.org/10.1034/j.1600-0749.2003.00014.x

29. Ackermann, J., Frutschi, M., Kaloulis, K., McKee, T., Trumpp, A., & Beermann, F. (2005). Metastasizing melanoma formation caused by expression of activated N-RasQ61K on an INK4a-deficient background. Cancer Research, 65(10), 4005–4011. https://doi.org/10.1158/0008-5472.CAN-05-0036

30. Xiao, M., Rebecca, V. W., & Herlyn, M. (2019). A Melanoma Patient-Derived Xenograft Model. Journal of visualized experiments : JoVE, (147), 10.3791/59508. https://doi.org/10.3791/59508

31. Davies, H., Bignell, G. R., Cox, C., Stephens, P., Edkins, S., Clegg, S., … & Stratton, M. R. (2002). Mutations of the BRAF gene in human cancer. Nature, 417(6892), 949–954. https://doi.org/10.1038/nature00766

32. Pollock, P. M., Harper, U. L., Hansen, K. S., Yudt, L. M., Stark, M., Robbins, C. M., … & Meltzer, P. S. (2003). High frequency of BRAF mutations in nevi. Nature Genetics, 33(1), 19–20. https://doi.org/10.1038/ng1054

33. Michaloglou, C., Vredeveld, L. C., Mooi, W. J., & Peeper, D. S. (2008). BRAF(E600) in benign and malignant human tumours. Oncogene, 27(7), 877–895. https://doi.org/10.1038/sj.onc.1210704

34. Huang, J. M., Chikeka, I., & Hornyak, T. J. (2017). Melanocytic Nevi and the Genetic and Epigenetic Control of Oncogene-Induced Senescence. Dermatologic clinics, 35(1), 85–93. https://doi.org/10.1016/j.det.2016.08.001

35. Bennett, D. Human melanocyte senescence and melanoma susceptibility genes. Oncogene 22, 3063–3069 (2003). https://doi.org/10.1038/sj.onc.1206446

36. Ruiz-Vega, R., Chen, C. F., Razzak, E., & Lander, A. D. (2020). Dynamics of nevus development implicate cell cooperation in the growth arrest of transformed melanocytes. eLife, 9, e61026. https://doi.org/10.7554/eLife.61026

37. McNeal, A. S., Liu, K., Nakhate, V., Natale, C. A., Dereure, O., Redmer, J. B., ... & Judson-Torres, R. L. (2021). Environmental cues drive melanocyte nevi formation and regression in vivo. eLife, 10, e70385. https://doi.org/10.7554/eLife.70385

38. Wouters J, et al. Robust gene expression programs underlie recurrent cell states and phenotype switching in melanoma. Nat Cell Biol 22, 986-998 (2020).

39. Rambow F, et al. Toward Minimal Residual Disease-Directed Therapy in Melanoma. Cell 174, 843-855 e819 (2018).

40. Rambow F, Marine JC, Goding CR. Melanoma plasticity and phenotypic diversity: therapeutic barriers and opportunities. Genes Dev 33, 1295-1318 (2019).

41. Tirosh, I., Izar, B., Prakadan, S. M., Wadsworth, M. H., Treacy, D., Trombetta, J. J., ... & Regev, A. (2016). Dissecting the multicellular ecosystem of metastatic melanoma by single-cell RNA-seq. Science, 352(6282), 189-196. https://doi.org/10.1126/science.aad0501

42. Jerby-Arnon, L., Shah, P., Cuoco, M. S., Rodman, C., Su, M. J., Melms, J. C., ... & Regev, A. (2018). A cancer cell program promotes T cell exclusion and resistance to checkpoint blockade. Cell, 175(4), 984-997.e24. https://doi.org/10.1016/j.cell.2018.09.006

CHAPTER 2:

The Non-genetic Transition of *Braf*-mutant Melanoma Tumorigenesis

Karen Hui Xiao, Jessica Shiu, Chi-Fen Chen, Jie Wu, Peijie Zhou, Sahil S. Telang, Rolando Ruiz-Vega, Robert A. Edwards, Qing Nie, Arthur D. Lander, Anand K. Ganesan

INTRODUCTION

Melanomas exhibit DNA alterations involving multiple oncogenes and tumor suppressor genes[1, 2, 3]. However, because melanocytes possess a high background of mutation, it has been difficult to identify a specific sequence of events that inexorably leads to melanoma[4]. Whereas activating *BRAF* mutations are commonly observed driver mutations in melanomas, occurring in 60% of cases [5], the same mutations are also found in nearly all non-malignant growth-arrested melanocytic nevi [6]. This result, together with the observation that expressing activated *Braf* in mouse melanocytes primarily generates nevi, has led to the view that MAP kinase pathway activation (through mutation of *Braf* or, alternatively, *Nras*) is necessary to initiate melanoma but generally not sufficient.

When activated *Braf* (or *Nras*) in mouse melanocytes is combined with complete loss of function mutations of tumor suppressor genes (*Pten*, *p53*, *Ink4a*, *Cdkn2a*), melanomas arise rapidly[7, 8, 9]. It has been hypothesized that, without the help of these additional mutations, activation of *Braf* or *Nras* leads to oncogene induced senescence (OIS) and cell cycle arrest, explaining why only nevi are formed[10, 11]. Recent studies cast doubt on this hypothesis and show both that *Braf* activation does not induce melanocyte senescence *in vivo*[12], and that nevus cells remain competent to proliferate[13]. At present, the mechanism behind growth arrest following *Braf* activation remains unknown but may involve feedback loops normally involved in melanocyte homeostasis[12].

When activated *Braf* is expressed in the melanocytes of mice, in some cases (depending on the expression construct and genetic background[7, 9]), rare melanomas do arise, amongst a background of abundant nevi. While it seems plausible that the spontaneous acquisition of additional mutations explains malignant transformation, that hypothesis has not been tested. Indeed, such melanomas are far less studied than either human melanomas, or mouse melanomas produced when multiple mutations (typically three or more) are introduced simultaneously[14].

While mouse melanomas that combine many mutations can be expected to model advanced human disease, by the same token, they may not be a good model for elucidating the stepwise progression that occurs between normal melanocytes and melanoma.

Recent studies suggest that such progression is likely to involve not only the accumulation of mutations but also transitions among cell states. Melanomas display a high degree of intratumoral heterogeneity, both in cellular behaviors and epigenetic modification[15], and stochastic switching between melanoma cell states has been directly observed *in vitro* [16, 17, 18, 19, 20] and proposed to occur *in vivo*. In some cases, it has been argued that specific states serve as necessary waystations on the path to therapeutic resistance[21, 22]. Little is known, however, about what drives transitions between states, nor the extent to which mutational or other processes influence them.

With the advent of methods for assessing transcriptomes at the single cell level, several groups have attempted to define the landscape of cellular heterogeneity in melanoma. Based on analyses of human melanomas, mouse models, and cell lines, gene expression signatures have been proposed to define cell states that have been variously categorized as pigmented, invasive, proliferative, neural crest (NC)-like, mesenchymal, intermediate, and *BRAF* inhibitor resistant[19, 22, 23]. Signatures derived in different studies are often divergent, and it is unclear whether this reflects real biological differences or variations in data quality or informatic approaches. A complicating factor is that most data come from the analysis of melanomas bearing different combinations of driver mutations (including in some cases ones that were not fully characterized) in a variety of genetic backgrounds.

Here we clarify the cellular complexity of melanoma during early stages of tumor development by focusing on two mouse models of "minimal" induction in which melanocytes are engineered to express only activated *Braf*, or activated *Braf* plus a single null allele of the tumor suppressor *Pten*. On a genetic background that allowed for rare melanoma emergence even when only *Braf* was

mutated, the kinetics of tumor appearance were consistent with a requirement for a single stochastic event. We found little evidence that this event involved a consistent DNA mutation or common copy number variation, although we could not rule out the possibility that multiple different mutations might exist that have similar effects in different tumors, or that certain kinds of mutations were missed. Analysis by single cell RNA sequencing of tumors, as well as adjacent and normal skin, revealed that the major cell types in minimally-mutated melanomas expressed relatively low levels of pigmentation genes, and the resulting tumors were indeed hypomelanotic. Through direct comparison of gene expression signatures, it was possible to identify major cell states in such tumors that was similar to a state specifically thought to play a role in the development of therapy resistance[22]. Intriguingly, one of the states we observed was also detected in tumor-free skin, suggesting it is not obligatorily malignant when it is present alone. Using new informatic tools we predicted that this cell may act as a direct source of more abundant types of tumor cells. We discuss the possible relationship of cell states we identify here to events in human melanoma initiation and progression.

RESULTS

Braf activating mutations induce rare melanomas in both *Pten*-heterozygous and wild-type albino mice

We used a *Tyrosinase::CreERT2; Braf*$^{CA\text{-}fl/+}$ construct[24] in transgenic mice to specifically activate *Braf* in melanocytes by topically applying tamoxifen at postnatal days 2-4 (Fig 1A). On a C57BL/6 background, such mice developed abundant nevi in a matter of weeks, but no melanomas. In contrast, when a single floxed allele of *Pten* was introduced into this background, creating a heterozygous *Pten* mutation in melanocytes, sporadic tumors arose, an average of three per animal (Fig 1A-C). Both gross (Fig 1A) and histologic (Fig 1D) analysis of these tumors strongly suggested they did not arise by loss of heterozygosity of the wild type *Pten* allele. For example, whereas melanomas generated by activating *Braf* together with loss of both *Pten* alleles

(*Pten*$^{\Delta/\Delta}$), are strongly pigmented[7, 25] (Fig 1C, right lower image), these tumors display very little pigment either visually (Fig 1A, S1A) or histologically (Fig 1C). In addition, immunofluorescence staining of *Pten*$^{\Delta/+}$ tumors confirmed that they expressed Pten protein (Fig 4).

We also examined the outcome of expressing *Braf*$^{CA/+}$ in the melanocytes of albino mice (congenic with C57BL/6, Fig S1C). We found that, on an albino background (*Tyr*$^{c\text{-}2J}$), *Braf*$^{CA/+}$ alone produced melanoma in about 2/3 of animals, with no animals displaying more than one tumor (Fig 1A-C). Combining *Braf*$^{CA/+}$ with *Pten* heterozygosity in albino mice increased the numbers of tumors per animal to a level similar to that seen in black *Braf*$^{CA/+}$ *Pten*$^{\Delta/+}$ mice (Fig 1B-C). Albino *Braf*$^{CA/+}$ tumors also displayed immunologically detectable Pten (Fig 4).

The rarity of tumors when *Braf* is activated either alone or together with a single loss of function allele of *Pten* suggests at least one additional event is required to produce melanoma. The distribution of times at which tumors become detectable in such mice strongly suggests that the event is statistically random, i.e. occurs with a constant, small probability. As shown in Figure 1B, plots of tumor-free survival over time are fit by single declining exponential functions, consistent with "single-hit kinetics", i.e., the expectation of a process with a constant probability per unit of time. Because of the need for tumors to exceed a threshold size before being detected, we cannot rule out the possibility of *more* than one random event being required for tumor initiation, but based on the application of the single-hit model, we may extract from the final slopes of logarithmic plots a "half-time" ($t_{1/2}$) for tumor initiation (the expected time for tumors to arise in 50% of animals) equal to ~33 weeks in albino *Braf*$^{CA/+}$ mice, ~15 weeks in albino *Braf*$^{CA/+}$ *Pten*$^{\Delta/+}$ mice, and ~6 weeks in black *Braf*$^{CA/+}$ *Pten*$^{\Delta/+}$ mice. It is important to note that, on such plots, the rate of tumor growth is reflected only in the initial lag-time and not the eventual slope, which is a measure of when initiating events occur. Nonetheless, it is clear that pigmentation status and *Pten* gene dosage both influence the probability of melanoma initiation in *Braf*$^{CA/+}$ and *Braf*$^{CA/+}$ *Pten*$^{\Delta/+}$ mice.

To investigate whether the random, initiating event required to produce albino *Braf*$^{CA/+}$ tumors is a shared *de novo* DNA mutation, we performed whole genome sequencing (WGS) on three such tumors (Fig 2A-B). Tumors were dissected from the overlying skin, and DNA was prepared along with control DNA from spleen and skin of the same animals. Sequencing was performed to an average of 80X coverage (within mappable regions, >99% of nucleotides were covered at least 40 fold). A Bayesian somatic genotyping model (Mutect2) was used to identify tumor-specific somatic variants as those present in tumor samples but absent from the spleen of the same animal. Based on the levels of unrecombined and recombined *Braf*$^{CA/+}$ alleles detected in each sample, we estimated (see Methods) that the fraction of DNA that was tumor-derived in each sample was 19%, 55%, and 36%, for tumors 1, 2, and 3, respectively, in Fig 2A-B. As a heterozygous mutation required for malignant transformation should have been observed at half these allele frequencies, the probability, even assuming only 40X coverage, of failing to observe a mutation in one of the three tumors would have been 2%, 0.00025%, and 0.036% respectively.

Overall, we observed between 4,000 and 14,100 mutations per sample, including single nucleotide variants (SNVs), insertions, deletions, substitutions, and stop gains. Many were present at low frequency (compared with the expected proportion of tumor genomes in each sample; Tables 1, 3 and 5), very few were exonic, and only a handful of those were nonsynonymous (Fig 2B; Tables 2, 4 and 6). Of these, no gene was mutated across all three tumors. We noted two genes in which mutations were seen in 2/3 tumors sequenced (Table 7). One of these genes, *Pira6*, a gene that is involved in osteoclast function[26], was not expressed in the tumor (no reads in *Pira6* gene were detected in any of the cells in the tumor single cell RNAseq dataset, discussed below) and was thus not investigated further. A second gene, *Flna*, had a mutation near exon 21 in 1/3 tumors and a second mutation in exon 45 in 1/3 tumors. Given the incidence of *Flna* mutations, we further explored the prevalence of Flna mutations using our single cell RNAseq data (see below for description of our dataset). We observed Exon 21 *Flna* mutations in 2/7 tumors subjected to scRNAseq (Table 8). We observed no Exon 45 *Flna* mutations in tumors in our single cell RNAseq

dataset (Table 8). Published studies identified the region around exon 21 of *Flna* as a mutation hotspot in mouse melanoma tumors, with 20-33% of tumors that arose in the absence of UV having a *Flna* mutation around exon 21 regardless of initiating mutation [27, 28]. This is consistent with our results here, where we observed *Flna* mutation in 3/10 tumors. According to the three-dimensional structure of the Flna protein[29], the *Flna* Exon 45 mutation removes three amino acids in a flexible loop between two beta-strands in one of the filamin repeats. Whether this would have functional consequences for that domain is difficult to say without direct structure/function studies, but this site was not identified as a hotspot in the other mouse melanoma studies[27, 28]. We specifically checked, and did not find, mutations in sequences upstream of *Tert* that correspond to sites of promoter mutations in human melanoma[30]. Mutational signatures were also examined using SigProfiler[31] (Fig 5). Interestingly, C to T mutation changes were more frequent than other changes even though these mice were not intentionally exposed to UV light (the frequency of these changes was lower than typically observed after UV treatment[27]).

Since the above methods do not detect DNA changes on a larger scale than the sizes of the sequenced fragments, we also used paired-end whole genome sequencing to identify breakpoints and infer copy number variations (CNVs) and structural variations (SVs). We used the *BreakDancer*[32] pipeline to identify CNVs that were unique to the tumor and not observed in the spleen or skin of the same animal (allowing for a false discovery rate of 0.05, a relatively lenient cutoff). We grouped CNVs by the gene bodies to which they were closest. Only one gene, *Thrb,* had CNVs near the gene body in all three tumors sequenced (Fig 2A, Table 9, 12, 15), and the three observed mutations were all small, intronic, and did not overlap, and thus seemed unlikely to have an impact on gene expression (Fig 2C). We also did not observe expression of *Thrb* in tumor cells by single cell gene expression (Fig 8C), suggesting it would be unlikely for a mutation in this gene to contribute to tumor initiation. Of note, we did not observe CNVs in genes that have been identified to display copy number variations in human *Braf* mutant tumors, including tumor suppressor genes *Pten, Cdkn2a, Tert, Nf1, Tp53, Rac1* and *Cdk4*[3].

We also used *CNVkit*[33] to search for potential CNVs in the same tumor samples. CNVkit predicts deletions and duplications from contiguous regions of difference in coverage (read depth), relative to a reference sample (in this case control spleen DNA), adjusted for tumor cell frequency. Because read-depth based algorithms have high false positive rates[34], we used spleen-spleen comparisons to estimate rates of false discovery, and identified generous parameters expected to limit false discoveries to a few hundred per tumor sample (see Methods). CNVs were identified in all tumors but the involved genes overlapped poorly with each other, and even less well with those identified in any tumor by Breakdancer (Table 11, 14, 17). No gene known to display copy number alteration in human *Braf* mutant tumors was identified among CNV calls that were shared across tumors. In four cases Breakdancer detected a SNV near those calls in a single tumor, but the breakpoints were inconsistent with the CNV changes suggested by CNVkit, which were therefore judged likely to be false positives.

To better depict the level of structural variants and copy number variants, we plotted the observed structural variants identified by BreakDancer on CIRCOS plots (Fig 6A) and copy number variants identified by CNVkit on scatterplots (Fig 6B), as described[33]. When comparing CIRCOS plots depicting structural variants present in skin when compared to spleen and tumors after skin and spleen were subtracted, we observed that the level of detected structural variants was similar and most of the structural variants identified did not overlap (Table 10, 13, 16). In fact, the total number of structural variants in the tumor were 1-3% greater than the number of variants identified in the spleen (Table 10, 13, 16), indicating that the number of structural variants in tumors was not significantly greater than the degree of background structural variants observed in skin. Similarly, scatterplots of segment copy number inferences failed to identify any copy number segment alterations conserved between tumors (Figure 6B).

Finally, we used a third method to search for CNVs in albino *Braf* mutant tumors, which involved searching in single cell transcriptomic data for contiguous blocks of gene expression

displaying greater or lower than expected transcript numbers (these data are discussed below in the next section on single cell RNA sequencing). Even when adjusted to a relatively high false discovery rate, this method also failed to identify shared or overlapping structural variants among tumors.

Identifying Melanocytic Cell States.

The possibility that a non-genetic transition—e.g. an epigenetic cell state change or a collective cell transition—may drive melanoma initiation, at least in albino *Braf*$^{CA/+}$ animals, is interesting given that non-genetic, stochastic switching between cell types has been described among melanoma cells *in vitro*[20]. If such switching plays a role in tumor initiation in *Braf*$^{CA/+}$ and *Braf*$^{CA/+}$ *Pten*$^{\Delta/+}$ mouse models, we reasoned that evidence of it might be found by analyzing the cell types or states within tumors. For example, we might observe a cell state in melanoma tumors that was also found in skin in which tumors had not yet arisen.

To explore this possibility, we performed single cell RNA sequencing on a total of 47 skin and tumor samples from 36 animals: 15 wildtype skin samples, 10 black *Braf*$^{CA/+}$ skin samples (which contain only nevi), 3 albino *Braf*$^{CA/+}$ tumors, 4 albino *Braf*$^{CA/+}$ *Pten*$^{\Delta/+}$ tumors, 4 black *Braf*$^{CA/+}$ *Pten*$^{\Delta/+}$ tumors, and 11 sample-matched tumor-adjacent-skin samples collected alongside each of the 11 tumor samples (Fig 7A, 7D, Table 18). After combining samples using the merge function of Seurat, performing quality control, and normalizing using scTransform, a total of 345,427 cells were identified. Using unsupervised clustering, based on highly variable genes and marker genes known to identify cell types, we identified 18 cell types, including melanocytes (*Dct*+, *Pmel*+, *Mitf*+, and *Mlana*+), Schwann-cells (*Mpz*+, *Dhh*+), fibroblasts (*Pdgfra*+, *Col3a1*+, *Sparc*+) and macrophages (*Adgre1*+, *Cd74*+, *Ctss*+) (Fig 2B-C, Table 19). Specifically within tumor samples, we observed an abundant cell type that expressed markers commonly seen in melanoma, including the markers *Plp1, Gpm6b, Postn, Mcam, S100b*[35] (Fig 7B, 8B).

We then subsetted the cells in all samples that were judged to have a potential lineage

relationship to melanocytes. These included melanocytes themselves, Schwann cells (thought to share a common precursor with melanocytes[36]), and any cell types in which we could document recombination driven by the *Tyr-CreERT2* transgene (in a subset of samples, the mTmG reporter system[37] was used so that expression of GFP marked cells in which Cre-mediated recombination had occurred); the latter included the abundant cell type in tumor samples that expressed melanoma markers.

These 35,527 cells, which we refer to as "NC-derived", were re-normalized using ScTransform and subclustered (Fig 8A, 8C, Table 20). We identified within this group melanocytes, which produce a high level of pigmentation genes (*Ptgds*, *Pmel*, *Mlana*) consistent with the highly pigmented nature of nevus melanocytes [12]; a Schwann cell population (marked by *Mpz*); and several tumor-enriched cell populations that clustered separately from melanocytes, and expressed melanoma markers (*Plp1, Gpm6b, Postn, Mcam*[35]) (Fig 8B-C). A distinct population of cells was observed primarily, but not exclusively, in tumor samples and could be distinguished by weak but detectable expression of pigmentation genes (*Mlana, Tryp1*), expression of multiple "neural" genes (*Bche, Sema3b*), and expression of genes encoding structural components of the extracellular matrix. We termed these LNM (Lightly pigmented, Neural, extracellular Matrix) cells. Other markers of LNM cells included *Aqp1, Dhh,* and *Igf1* (Fig 8B-C). Although LNM cells were relatively abundant in tumor samples, they were also observed in normal skin, and their numbers increased substantially in the tumor-free skin of $Braf^{CA/+}$ mice (Fig 8D). We calculated the Euclidean distance in principal component space between LNM cells, the principal tumor cluster, Schwann cells and melanocytes and observed that the LNM cells were closer to principal tumor cells than to the Schwann cells or melanocytes (Fig 8E, Table 22). Immunohistochemical staining for Aqp1 indicated that LNM cells were sparse in normal skin, located in or around nevi in black $Braf^{CA/+}$ skin, and were observed throughout the dermis in $Braf^{CA/+}$ tumors (Fig 8F).

Principal tumor cells, defined by the expression of known melanoma marker genes *Postn*+,

Mcam+, *Plp1+*, *Gpm6b+*[35], were observed in tumors from all three genotypes (Fig 7E). These cells could be subclustered into four distinct subsets. Two included cells of all three genotypes, which we refer to as "shared" and "proliferative". The remaining two corresponded to groups unique to either *Pten*$^{\Delta/+}$ or *Pten*$^{+/+}$ tumors (the latter necessarily being albino) (Fig 8A-C). The shared cluster was marked by expression of extracellular matrix related genes (*Vcan, Col20a1*) and low expression of pigmentation genes (*Mitf*, *Dct*, *Pmel*)[38] (Fig 7E, 8B) consistent with the observation that pigment in these tumors was not readily apparent visually or histologically, even in black mice (Fig 1A,1D). The proliferative cluster was marked by the expression of proliferation markers *Top2a*[39], *Mki67*[39], and *Hmgb2*[40] (Fig 8B-C). The *Pten*$^{\Delta/+}$-specific cluster was distinguished by expression of genes associated with cell stress (*Fos, Jun*)[41], whereas the albino *Pten*$^{+/+}$-specific cluster was marked by expression of genes that have been suggested to mark "neural crest stem cells" (*Aldh1a1, Ngfr, Reln*) [19, 42] (Fig 8B-C).

We also identified and subclustered fibroblastic and immune cells in both skin and tumor samples. Cancer-associated fibroblasts (CAFs) and tumor-associated macrophages (TAMs) were specific to tumor tissue (Fig 7B); their gene expression profiles were consistent across tumor genotype (*Braf*$^{CA/+}$ *Pten*$^{+/+}$ vs. *Braf*$^{CA/+}$ *Pten*$^{\Delta/+}$) (Fig 7E). CAFs expressed markers that had been previously identified in other cancer types (*Mgp*, *Col1a1a*, *Pdgfrb*, *Pdgfa* [43]) (Fig 10A). TAMs shared the expression of some macrophage specific markers with tissue macrophages, but failed to express other markers characteristic of tissue macrophages (*Cxcl2*[44] and *Retnla*[45] (Fig 10B)).

The ability to isolate cells of different types using scRNAseq provided an additional opportunity to look for DNA structural changes specific to tumor cells. In this case, inferCNV (https://github.com/broadinstitute/inferCNV) was used to search for large, contiguous blocks of genes that collectively display higher or lower than expected levels of gene expression in principal tumor cells versus tumor fibroblasts, macrophages and other non-malignant cells. This approach has been used by others to identify conserved CNVs amongst different prostate tumors that drive

tumor growth[46]. Here, we used it to search for CNVs involving genes or groups of genes conserved across the three tumors. To minimize the chances of missing any shared CNVs, we increased the sensitivity of the algorithm so that a 20% false discovery rate was accepted. Under these conditions, several regions were flagged as CNVs in macrophages in all samples (Fig 9), which most likely represent false discovery due to high expression of multiple closely-linked genes (e.g. the MHC locus on chromosome 17)[47]. Under such conditions, we did not observe any conserved inferred CNVs in tumor cells from the three albino tumors (Fig 9). We did observe a putative copy number gain in one tumor in chromosome 6. In addition to carrying the *Braf* gene, chromosome 6 carries several genes that are highly expressed in the LNM and tumor populations (*Aqp1*, *Col1a2*, *Cav1*, *Cav2*, *Ptn*, *RaRes2*, *Fkbp9*, *Actg2*, *Ybx3*, *Mgp*, *Sox5*, *Kcna1*, and *Ptms*). Thus, observations in chromosome 6 could be skewed by the high expression of genes characteristic of the LNM and tumor populations, representing an artifact similar to what was observed with macrophages[47]. In summary, these results fail to identify an inferred CNV that affects all three tumors examined.

LNM Cells Persist after Tumor Transplantation

Single cell RNA sequencing identified LNM cells as a population present at low levels in normal skin, enriched in $Braf^{CA/+}$ skin (Fig 8D) and highly enriched in tumors (Fig 8F). To assess whether LNM cells are an integral part of the tumor microenvironment, we subjected tumors to serial transplantation, using an approach developed for propagating patient derived xenografts[48] (Fig 11A). *Braf* mutant *(*albino $Braf^{CA/+}$ and black $Braf^{CA/+}$ $Pten^{\Delta/+}$*)* tumors were readily transplantable, with the highest rate of success occurring when immune deficient (NSG) hosts were used. Interestingly, the time delay to initiate the growth of melanoma tumors shortened after rounds of serial transplantation (Fig 11B), consistent with enrichment for tumor generating populations. Single cell transcriptomics was used to quantify numbers of cells of different types after different rounds of transplantation (Fig 11A).

After integrating single cell data from transplants and the primary tumors from which they derived (using Harmony [49]), and clustering by gene expression, we identified four NC-derived clusters: a principal tumor cluster, a melanocyte cluster, and two LNM clusters (Fig 11C-D, Table 16). The principal tumor cluster shared many of the same markers as the parental tumors, such as *S100b*, *Postn*, and *Mcam* (Fig 11E). The "LNM1" population in the transplanted tumors had a similar gene expression profile as the LNM cells in the parental tumors (*Aqp1*, *Igf1*, *Sema3b*) (Fig 11E). We also identified a separate "LNM2" population, which had decreased expression of some of the markers of parental LNM cells (*Aqp1*, *Ptn*) and expressed some marker genes that were not present in the parental LNM population (*Spp1*, *Igfbp3*) (Fig 11E). The proportion of LNM cells increased after successive rounds of transplantation (Fig 11F, Fig 12A), from 10.7% in round 1 to 95.6% in round 2, with the majority of the expansion attributable to LNM2. Of note, LNM2 cells were nearly absent from primary tumors in immunocompetent mice, indicating that their abundance maybe somehow influenced by the immunocompromised environment. When we calculated the Euclidean distance between all NC-derived cell types we observed that both tumors and melanocytes are slightly closer to LNM2 than LNM1, and LNM1 and LNM2 cells were equidistant from each other (Fig 11G, Table 23). We note that *Aqp1* is expressed in 60% of endothelial cell populations as previously described[50], but also in 95% of LNM1 cells, 34% of LNM2 cells, but only 3% of tumor cells (Fig 12A, Table 21). *Sox2*, on the other hand, is expressed in LNM1, LNM2 cells, and tumor cells, but not in melanocytes or other cell lineages in our dataset. Thus, despite the observed gene expression differences between LNM1 and LNM2, these populations shared the expression of *Sox2* and *Aqp1*, and these markers were not co-expressed in other cell populations in skin.

A role for *Sox2* in melanoma initiation

We noted that LNM cells were specifically enriched in the expression of the stemness-associated transcription factor *Sox2,* with greater than 30% of LNM cells expressing *Sox2* (Fig

11C-F, Fig 12A, 12C). *Sox2* is also detected in human melanomas[51] and has been described as enriched in melanoma-initiating cells[52], but studies in mouse models thus far failed to support a role for it in melanoma formation. For example, it has been reported by other groups that, in mice bearing either combined $Braf^{CA/+}$ $Pten^{\Delta/\Delta}$ [53] or $Nras^{Q61K/+}$ $Ink4a^{\Delta/\Delta}$ [54] mutations, loss of *Sox2* did not prevent tumor formation. When we crossed conditional alleles of *Sox2* ($Sox2^{fl}$) into the $Braf^{CA/+}$ $Pten^{\Delta/+}$ background, however, we observed a different result. When $Braf^{CA/+}$ $Pten^{\Delta/+}$ $Sox2^{fl/fl}$, $Braf^{CA/+}$ $Pten^{\Delta/+}$ $Sox2^{fl/+}$, $Braf^{CA/+}$ $Pten^{\Delta/+}$ $Sox2^{+/+}$ mice were treated with tamoxifen at p2-4, a marked *Sox2* gene dosage-dependent decrease in tumor incidence was observed (Fig 12B, Fig 12D). Immunohistochemistry demonstrated that tamoxifen treatment successfully deleted *Sox2* expression in tumor cells (Fig 12E). As LNM cells express the highest levels of *Sox2* and *Sox2* expression is largely absent from melanocytes (<1%) and present at a low level in tumors (17%), these results are consistent with the contention that the *Sox2* expressing LNM cell may be the cell that initiates $Braf^{CA/+}$ $Pten^{\Delta/+}$ tumors.

Comparative Analysis of Single-Cell RNA-seq Data between Mouse and Human Tumors

Unlike mouse models, in which oncogenic mutations are usually introduced simultaneously, the order in which mutations (as well as other heritable changes) arise in human melanomas is unknown, and potentially differs from individual to individual. This prompted us to compare the cellular states that we detect in $Braf^{CA/+}$ and $Braf^{CA/+}$ $Pten^{\Delta/+}$ mouse melanomas with those described for human melanoma samples, several of which have now been subjected to analysis by single cell RNA sequencing [18], as well as those identified in other mouse melanoma tumors. Although comparison of gene expression states across species can be problematic, we took advantage of the fact that a variety of gene expression signatures have been proposed as markers of human melanoma cell states.[55] To facilitate the mapping of agreement with these signatures onto our scRNAseq data, we developed a "membership score" pipeline that weights the

contributions of genes according to their degree of differential expression among the NC-derived cells in our samples (see Methods). Given a set of genes, and a collection of cells, the method assigns each cell a score representing an aggregate of how far above or below the average each gene's expression is. To minimize batch artifacts, the NC-derived cells of each tumor genotype (Albino *Braf*$^{CA/+}$, Albino *Braf*$^{CA/+}$ *Pten*$^{\Delta/+}$, and black *Braf*$^{CA/+}$ *Pten*$^{\Delta/+}$) were analyzed separately. In Fig 14A, cells are displayed on individual UMAPs, and five clusters—principal tumor cells, proliferating tumor cells, melanocytes, Schwann cells, and LNM cells—are highlighted. Membership scores were calculated on a cell-by-cell basis for signatures (Table 24-25) that have been reported for treatment-naïve human melanoma biopsies[55] (including patients with both primary and metastatic human melanomas); patient-derived xenografts grown in immune deficient mice and subjected to *Braf*-inhibitor treatment[22]; melanoma cell lines (commercially available and stepwise CRISPR-edited)[19, 56]; and other mouse melanoma models (*Nras*$^{Q61K/+}$ *Ink4a*$^{\Delta/\Delta}$, *Braf*$^{CA/+}$ *Pten*$^{\Delta/\Delta}$[18], and stepwise CRISPR-edited[56]).

Mapping these scores onto the UMAP plots in Figure 13 revealed some similarities between the cell types identified in our mice and these signatures. Specifically, the principal tumor cells had features resembling the "neural crest-like", "antigen-presenting", and "mesenchymal" signatures of human melanomas; the "invasion" signature of human xenografts; the "mesenchymal" and "partial-EMT" signatures of *Braf*$^{CA/+}$ *Pten*$^{\Delta/\Delta}$ mouse tumor cells, the "stem-like" signature of *Nras*$^{Q61K/+}$ *Ink4a*$^{\Delta/\Delta}$ mouse tumor cells; the "EMT" signature of CRISPR-edited in-vitro and in-vivo tumor cells; and the "mesenchymal" signature in melanoma cultures (Fig 13A-B). In contrast, LNM cells most closely resembled the "Interferon-alpha-beta response", "mitochondrial", and "stress" sets of human melanomas; the "intermediate" signature in melanoma cultures; and the "neural crest", "neural crest stem cell like", and "Interferon/TGF" signatures of xenografts and other mouse models (Fig 13B), signatures that overlapped only weakly with principal tumor cells.

Although both LNM and principal tumor cells expressed pigmentation genes at low levels, there was scant pigment visible on the surface of black *Braf*$^{CA/+}$ *Pten*$^{\Delta/+}$ tumors (Fig 1D), a finding also reported by others[57], which motivated us to examine whether gene expression of any of the cells in these tumors aligned with the *Mitf*-high pigmentation signature that has been identified in other mouse and human melanomas. Membership scoring showed that *Mitf*-high "melanocytic", "melanocyte", "Interferon/p53", "Myc/mTORC1/OxPhos", "OxPhos", and "β-catenin/MITF" signatures identified by others in human biopsies, xenografts, cell cultures, and pigmented mouse melanomas were observed mainly in skin melanocytes, only very weakly detected in principal tumor cells, and essentially absent from LNM cells in our tumors (Fig 13C, 14C).

Prediction of Cell State Dynamics Between LNM Cells and Principal Tumor Cells.

Despite being distinct from principal tumor cells, several characteristics of LNM cells suggest they play a role in tumor formation and growth—for example, the importance of *Sox2*, which is most strongly expressed in LNM cells (Fig 12A), in tumor formation (Fig 12B); the persistence of LNM cells during serial transplantation (Fig 11C-F); and the expression within LNM cells of gene signatures associated with human and mouse melanoma cell states (Fig 13B). Two approaches were taken to test the possibility that LNM and principal tumor cells represent potentially interconverting states.

First, we applied RNA velocity analysis, using scVelo[58], to the NC-derived cells of individual tumors (Fig 15A-D, Table 26). RNA velocity uses levels of spliced and un-spliced transcripts to infer cell state dynamics, ordering cells based on the principle that high proportions of unspliced reads indicate recently induced genes while low proportions indicate genes recently turned off. We also analyzed cells using MuTrans, a pipeline that uses dynamical systems concepts to infer transient cells and cell-fate transitions from snap-shot single cell transcriptome datasets [59] (Fig 15E-H, Table 27). To minimize batch-related artifacts, analyses were performed separately on

individual black *Braf*$^{CA/+}$ *Pten*$^{\Delta/+}$ tumor samples. These tumors contained a higher fraction of LNM1 cells but only rare LNM2 cells. To increase the probability of detecting transitions, we also analyzed two sets of tumors obtained after rounds of serial transplantation (Fig 11C-F). These tumors contain a high fraction of LNM2 cells and rare amounts of LNM1 cells.

In every sample analyzed, both RNA velocity and MuTrans independently supported the conclusion that transitions occur between LNM cells and principal tumor cells (Fig 15B-D, Fig 15H). Among all possible transitions identified by MuTrans, the path from cells that express high levels of *Aqp1* to primary tumor was also consistently identified as the most likely of all possible transition paths (Fig 15B-D, Fig 15H).

DISCUSSION

Genetic heterogeneity, epigenetic modifications, and a panoply of cell states are characteristic of melanoma[23], yet the background rate of mutation in human skin[60, 61] makes it difficult to ascertain relationships between cell state landscapes, individual mutations and non-genetic factors. In addition, melanomas in individual patients can differ markedly in histological characteristics, and can include the absence of pigmentation[62] as well as the expression of different degrees of "neural" phenotype[63].

Mouse models have thus played an important role in providing insights into how melanomas arise[14]. In mice, combining gain of function oncogene mutations (*Braf* and *Nras*) with homozygous loss of function mutations in tumor suppressor genes (*Cdkn2a, Pten, Ink4a*) provides an efficient route to the rapid generation of melanoma[64, 65]. Here we focus on melanomas generated either solely by *Braf* activation, or by *Braf* activation in combination with heterozygous loss of function of *Pten*. Such melanomas arose slowly and rarely, with kinetics indicating the requirement for a low-probability, random event. Interestingly, the incidence data imply that, even though tumor formation in response to *Braf* activation alone is much more probable in

albino than black mice (essentially absent in the latter, although occasionally reported by others[9]), when one allele of *Pten* is also inactivated, tumors arise somewhat sooner in black than albino mice (Fig 1). Taken together, the data suggest that the albino allele can exert both positive and negative effects on tumor initiation in the models described here.

The tumors produced by *Braf* activation in combination with heterozygous loss of function of *Pten* (retaining expression of the remaining *Pten* allele) grew slowly and were hypomelanotic. The LNM cells described here overlapped substantially in gene expression with very lowly-pigmented "neural crest" and "neural crest stem cell-like" signatures seen in other mouse and human tumors. Interestingly, in human xenograft models, this slow-growing state is seen in substantial numbers only after treatment with *Braf* inhibitors. It has been proposed that these cells serve as an intermediate on the way to a final, *Braf*-inhibitor resistant tumor cell type[22, 66]. Based on comparisons with those and other studies, we propose a model that describes how tumors can arise in melanocytes with *Braf* activation alone or *Braf* activation in combination with heterozygous loss of function of *Pten* (Fig 16).

The starting point of the model is the observation that normal skin contains both pigment-producing melanocytes and LNM cells—the latter potentially corresponding to various types of neural crest or melanocytic precursor cells that have been described in normal skin [36, 67]. These cell types may exhibit a precursor-product relationship, or even interconvert, but this hypothesis remains to be tested. Introduction of an activating *Braf* mutation into melanocytes and/or LNM cells is sufficient to drive the rapid formation of growth-arrested nevi. In mice at least, *Braf* activation also leads to an expansion of LNM cells (Fig 8D). A rare, stochastic event could then allow for the initiation of slow-growing, hypomelanotic tumors, potentially from Braf transformed LNM cells, whose phenotype such tumors resemble. It could involve a new mutation, but evidence for any mutation that was consistent across all tumors, or known to play a role in tumor initiation in melanoma, was not found. Although the molecular nature of that event is as yet unknown, it

can be accelerated in the context of an albino genotype, or the loss of a single allele of *Pten*, suggesting it is sensitive to even subtle changes in the growth properties of cells. It is possible that the stemness-associated transcription factor *Sox2,* which is required for tumor formation by this route 3), itself plays a role in the transition to malignancy, however it is also possible that *Sox2* is simply required for LNM cell growth or survival.

It is important to note that, when human xenografts were subjected to Braf inhibition, a distinct subset of cells survived and acted as a precursor to the development of inhibitor-resistant tumors. This subset was described as slow growing, poorly-pigmented, and characterized by a NC-like signature resembling the gene expression pattern of LNM cells (for example, such cells are marked by *Aqp1*). Although they were described as arising in response to inhibitor treatment, it seems likely these cells pre-existed as a minor population; indeed, a minor population with signatures overlapping with LNM cells can be found in primary human melanomas (Fig 13B), and *Aqp1*+ cells are observed histologically (Fig 8F)[55]. Here, using two different approaches (scVelo, muTRANS) in primary and transplanted tumors, we demonstrate that the LNM state may serve as an initial, or ongoing, source of tumor cells.

As for the question of whether mutation-dependent process is required for tumor initiation in the albino $Braf^{CA/+}$ tumors, we did our best to characterize any mutations that were shared among tumors. There are scenarios we cannot rule out. For example, we cannot rule out the possibility that multiple different mutations might exist that have similar effects in different tumors, or that certain kinds of mutations were missed, nor could we be certain that any mutation that we observe at high frequency in a tumor didn't arise after tumorigenesis and, for reasons having to do either with a fitness effect or neutral drift, came to dominate the tumor cell population. One difficulty in distinguishing these possibilities is that each method to identify mutations has caveats: short-read sequencing misses many structural variants; the power of bulk methods is diminished by the presence of non-tumor cells in tumor samples; inference of CNVs from gene expression data

can produce false positive results when groups of nearby genes exhibit cell-type specific expression; and methods designed to identify variants with high confidence (i.e. with few false positives) are not necessarily well-powered statistically to rule out the presence of variants (i.e. display few false negatives).

Despite these caveats, we do report that no established melanoma driver gene, besides *Braf*, is mutated in these tumors, which we believe to be important. Furthermore, we show that tumor incidence in the albino $Braf^{CA/+}$ model behaves as a single-step stochastic process with a half-time of approximately 33 weeks (Fig 1B). As we and other have reported previously[9, 11, 12], $Braf^{CA/+}$-transformed melanocytes become growth arrested within about 2 weeks of $Braf^{CA}$ activation *in vivo*, implying that whatever stochastic processes is leading to tumor formation likely takes place in non-dividing cells. In contrast, while new genetic variants are not conserved between the tumors, the cell state and cell state transition proposed to initiate melanoma tumors was seen in every case studied here.

Melanoma can be cured if detected early and removed[68], but it is often difficult to distinguish from benign lesions using clinical examination, histology, [69] or DNA alterations [4, 70]. It is intriguing to note that, in the present study, LNM cells accumulated in $Braf^{CA/+}$ $Pten^{fl/+}$ and $Braf^{CA/+}$ mice even in skin in which tumors had not yet developed (or could not do so). The detection of these cells in biopsies may represent a clinically useful marker of malignant potential as it appears that they are conserved across multiple different melanoma models in mice and humans. Furthermore, to the extent that these cells may ultimately act as a progenitor to tumor cells, they may also represent a target for development of preventive therapies. If the malignant transformation of these cells involves an epigenetic, rather than a genetic change, a wider range of therapeutic modalities could be explored than are usually considered in skin cancer prevention, which is currently focused on reducing mutation burden.

MATERIALS AND METHODS

Key resources table

Reagent type/resource	Designation	Source or reference	Identifiers	Additional information
Gene (Mus musculus)	Braf	Mouse Genome Informatics (MGI)	MGI:88190	
Gene (Mus musculus)	Pten	MGI		
Gene (Mus musculus)	Cre	MGI	MGI:3641203	MGI Transgene name: GeneTg(Tyr-cre/ERT2)13Bos
Mouse strain	C57BL/6J	Jackson Laboratory	000664	
Mouse strain	Albino B6(Cg)-*Tyr*$^{c-2J}$/J	Jackson Laboratory	000058	
Mouse strain	NSG	Jackson Laboratory	005557	
Sequence-based reagent	Braf_F	IDT	PCR primer	5'-TGAGTATTTTTGTGGCAACTGC -3'
Sequence-based reagent	Braf_R	IDT	PCR primer	5'-CTCTGCTGGGAAAGCGCC -3'
Sequence-based reagent	Pten_F	IDT	PCR primer	5' AAAAGTTCCCCTGCTGATGATTTG T 3'
Sequence-based reagent	Pten_R	IDT	PCR primer	5' TGTTTTTGACCAATTAAAGTAGGCTGT G 3'
Sequence-based reagent	Cre_F	IDT	PCR primer	5'- GGTGTCCAATTTACTGACCGTACA -3
Sequence-based reagent	Cre_R	IDT	PCR primer	5'- CGGATCCGCCGCATAACCAGTG - 3'
Chemical compound, drug	4-hydroxytamoxifen	Sigma-Aldrich	68047-06-3	
Primary Antibody	Aqp1 (1:200-400)	EMD Millipore	AB2219	Used for immunohistochemistry
Primary Antibody	Sox2 (1:500)	Abcam	Ab97959	Used for immunohistochemistry

Primary Antibody	Pten (1:100)	Cell Signaling	9559S	Used for immunofluorescence
Secondary Antibody	Alexa Fluor 594 goat anti-Rabbit IgG (1:1000)	Life Technologies	A11037	Used for immunofluorescence
RNAscope probe	Aqp1	ACD Bio	504741-C2	Used for RNAscope FISH
RNAscope probe	Sox2	ACD Bio	401041-C3	Used for RNAscope FISH
RNAscope fluorophores	Opal-620	Akoya Biosciences	FP1495001KT	Used for RNAscope FISH Channel 2
RNAscope fluorophore	Opal-650	Akoya Biosciences	FP1496001KT	Used for RNAscope FISH Channel 3
Software	Cell Ranger	10X genomics	RRID:SCR_017344	
Software	Seurat	Stuart et al., 2019	RRID:SCR_016341	
Software	Harmony	Korsunsky et al., 2019	RRID:SCR_022206	
Software	scVelo	Bergen et al., 2020	RRID:SCR_018168	
Software	MuTrans	Zhou et al., 2021		https://github.com/cliffzhou92/MuTrans-release
Software	BreakDancer	Tattini et al., 2015	RRID:SCR_001799	
Software	Trimmomatic	Bolger et al., 2014	RRID:SCR_011848	
Software	FastQC	Andrews et al., 2010	RRID:SCR_014583	
Software	InferCNV	Patel et al., 2014	RRID:SCR_021140	https://www.bioconductor.org/packages/release/bioc/html/infercnv.html
Software	SigProfiler	Khandekar et al., 2023	RRID: SCR_023122	https://github.com/AlexandrovLab/SigProfilerMatrixGenerator
Software	CNVkit	Talevich et al., 2016	RRID:SCR_021917	https://github.com/etal/cnvkit
Software	Annovar	Wang et al., 2010	RRID:SCR_012821	http://www.openbioinformatics.org/annovar/

Generation of *Braf*$^{CA/+}$ melanoma and nevi bearing mice

Conditional allele *Braf*^{CA}, *Tyr::CreER*, and/or *Pten*$^{lox4\text{-}5/+}$ mice (RRID:MGI:5902125, from Dr. Martin McMahon) were backcrossed with C57BL/6J (JAX 000664) for greater than 5 generations. Conditional allele *Braf*^{CA}, *Tyr::CreER*, and/or *Pten*$^{lox4\text{-}5/+}$ congenic C57BL/6J mice were then crossed with Albino B6(Cg)-*Tyr*$^{c\text{-}2J}$/J (JAX 000058) to create albino *Braf*$^{CA/+}$ melanoma and nevi bearing mice. Mice were genotyped by PCR as previously described (Bosenberg et al., 2006; Dankort et al., 2007). The primers used in this study are: Braf forward 5'-TGAGTATTTTTGTGGCAACTGC -3', Braf reverse 5'-CTCTGCTGGGAAAGCGCC -3', Pten forward 5'-AAAAGTTCCCCTGCTGATGATTTGT -3', Pten reverse 5'-TGTTTTTGACCAATTAAAGTAGGCTGTG -3'. Cre forward 5'-GGTGTCCAATTTACTGACCGTACA -3' and Cre reverse 5'- CGGATCCGCCGCATAACCAGTG -3'. Albino mice were identified by their coat color. All mice used in the study were heterozygous for the *Tyr::CreER* allele. The breeding schemes used to generate albino *Braf*$^{CA/+}$ and *Braf*$^{CA/+}$*Pten*$^{\Delta/+}$ mice are shown in Figure S1C; based on these we estimate the chances that tumor development in albino *Braf*$^{CA/+}$ mice could have depended on the presence of an unknown modifier gene present in founder albino mice to be small. Specifically, if an unlinked homozygous modifier had been present in both founder animals, we calculate the probability of it appearing in homozygous form in all tumor bearing mice at less than 1/10,000, and the probability of it appearing in heterozygous form at <7.5%.

Topical 4-hydroxytamoxifen (4-OHT; 25 mg/mL or 75 mg/mL in DMSO; 98% Z-isomer, Sigma-Aldrich) was administered to pups on their back at ages P2-P4. Mice were euthanized if the volume of their tumors exceeded 10% of total body volume, if tumors were significantly ulcerated, if mice were moribund, if they lost weight, if they were lethargic, or if they were unable to ambulate. All mouse procedures were approved by UCI's IACUC.

Tissue Harvest for Whole-genome Sequencing

Melanoma-bearing albino *Braf*$^{CA/+}$ mice (n=3, aged postnatal day 90 to 325) were euthanized, shaved, and depilated. Tumor (25mg), skin (25mg), and spleen (10mg) were then collected from each mouse and cut into small pieces with a scalpel, and the fat scraped off from the underside of the skin. Collected tissues were then stored in -80^{o}C freezer until sample preparation day. DNA materials were extracted using the Qiagen blood and tissue Kit, following protocols described for purification of total DNA from animal tissues. Briefly, approximately 25 mg of tissue was obtained and digested with ATL buffer and proteinase K. Ethanol was added to the lysate and passed through a DNeasy spin column. DNA was eluted with AE buffer.

Library Preparation for Whole-genome Sequencing

Library construction was performed using the NEXTflex Rapid DNA-Seq kit v2 and the NEXTflex Illumina DNA barcodes. Using the Covaris S220, 50ng of gDNA was sheared using settings to target 400bp. The sheared gDNA was end repaired and adenylated. The reaction mixture was cleaned up using AMPure XP magnetic beads and Illumina barcoded adapters were ligated onto the blunt-end/adenylated product. The adapter ligated product was cleaned using AMPure XP beads and then amplified for adapter ligated products using 5 cycles of PCR. The resulting library was cleaned with AMPure XP beads with double sided size selection and then quantified by qPCR with Kapa Sybr Fast universal for Illumina Genome Analyzer kit. The library size was determined by analysis using the Bioanalyzer 2100 DNA HighSensitivity Chip. The library was sequenced on the NovaSeq 6000 Sequencer, using an S4 flowcell chemistry and PE100 cycles with additional cycles for the index read. Sequences were obtained as paired-end 100 bp reads. The NovaSeq control software was v1.6.0 and the real time analysis software (RTA v3.4.4) converted the images into intensities and base calls. Post-processing of the run to generate the FASTQ files was performed at the UCI Institute for Genomics and Bioinformatics (UCI IGB).

Estimation of *Braf* Allele Recombination Frequency

In the mice used in this study, expression of constitutively active Braf was achieved through the recombination of an engineered allele in response to a melanocyte lineage-specific Cre[24]. In cells that do not undergo recombination, two loxP sites are present, each flanked by unique sequences (unrecombined loxP), whereas in cells that have recombined, a single loxP site remains, bringing together the flanking sequences from each of the two original sites (recombined loxP). In principle, one can use genome sequence data to estimate the fraction of cells in a tumor sample that underwent *Braf* recombination by examining the proportions of recombined and unrecombined loxP sequences in any sample.

Briefly, for each tumor, all sequences were extracted that matched the entire 34 bp loxP sequence and also contained at least two nucleotides at either end, allowing unambiguous assignment of recombined vs. unrecombined status. The fraction of recombined cells in each tumor sample was then calculated as the number of recombined sequences divided by the sum of the number of recombined sequences and half the number of unrecombined sequences (half because unrecombined cells have twice the number of loxP sites as recombined ones). In the three tumors analyzed here, the total number of loxP sequences used in the calculation was between 106 and 194. As a control, we also assessed recombination status in spleen and skin. In spleen, no recombined loxP sequences were detected in any tumor, as expected. In skin, no recombined sequences were detected in two cases, while two were detected in a single sample, implying a recombination frequency of 1.3%; this is consistent with the fact that melanocytes (which had the potential to recombine) are present at about this frequency in normal skin.

Whole Genome Sequencing Single Nucleotide Variant (SNV) Analysis

For SNV analysis**,** raw reads were transferred, and quality analyzed using *FastQC* tool (v0.11.9). Low quality bases and adapter sequences were trimmed using *Trimmomatic* (v0.39)[71]. Trimmed reads were then aligned to the mouse reference genome (build mm10) using the Burrows-Wheeler Aligner (*BWA mem*, v0.7.12)[72]. Duplicated reads were removed using *Picard tools*

MarkDuplicates (v1.130*)*. Local realignment and base quality recalibration was done on each chromosome using the Genome Analysis Toolkit (*GATK* v4.0.4.0) best practices. SNVs and indels were detected and filtered using GATK with HaplotypeCaller function. The output files were generated in the universal variant call format (VCF).

Somatic mutations were identified and filtered using mutect2(v4.1.3.0)[73] and bcftools (v1.15.1)[74]. To estimate the fraction of DNA in each sample that was derived from *Braf*$^{CA/+}$-expressing cells (as opposed to fibroblasts, immune cells, etc.), we identified all reads that mapped to the loxP sequence and that included at least three bases on either side. From the sequences up- and downstream of loxP we were able to uniquely assign each read to one of three categories: an un-recombined 5' loxP site, and unrecombined 3' loxP site, and a recombined loxP site. Unrecombined cells should contain one each of the sequences of the first two types, whereas recombined cell should contain a single sequence of the third type. Thus, the ratio of the observed number of sequences of the third type to the average of the number of sequences of the first two types provided an estimate of the ratio of recombined to unrecombined cells.

Variant Annotation with Annovar

Mutect2 called VCF files from each sample were first filtered with bcftools (v1.10.2) to retain variants with "PASS" flag. The filtered VCF files were then indexed, normalized with bcftools, and then annotated using Annovar (version date 2020-06-07) gene annotation function (*annotate_variation.pl*). This identified variants as compared to the RefSeq gene database that were a consequence of stop loss or stop gain or that hosted non-synonymous mutations or variable splice sites. The resulting variants were annotated as far as their type, i.e. exonic, UTR5/UTR3; intronic; or intergenic.

Structural Variant Calling Copy Number Variation (CNV) Analysis

For structural variant calling**,** BreakDancer (v1.1.2)[75] was used to analyze mapping results from

whole genome sequencing and classify structural variations in five categories: deletion, insertion, inversion, intrachromosomal translocation and interchromosomal translocation. Genomic regions with statistically significant amounts of anomalous read pairs (split reads and their depth) are considered supporting structural variations breakpoints. A Poisson model was implemented to incorporate the number of supporting anomalous reads, the size of the region, and the genomic coverage in order to compute a confidence score. The default set of parameters was used for BreakDancer.

We followed the recommended BreakDancer protocols[32] and analyzed the matched tumor, skin and spleen samples for each of the 3 animals. BreakDancer was run 3 times, each with 3 genomes from the same animal. In order to get somatic CNVs, the identified breakpoints were then filtered so that only those from the tumor are preserved (Tumor-skin-spleen). The 3 identified CNV lists from the 3 animals were then annotated with gene symbols if overlapping with a gene body. The 3 resulting gene lists were intersected to identify plausible recurrent somatic CNVs.

Coverage based Copy Number Variation (CNV) analysis

CNVKit [33] (v0.9.11), a read depth-based approach, was used to call and visualize copy number variants in tumor samples using the matched normal samples as background. Specifically, CNVkit attempts to detect structural variants based on differences in sequence coverage when compared with a reference sample. Aligned BAM files from both tumor and normal samples were imported to calculate copy number ratios that deviate from the expected by an amount consistent with structural alteration in a fraction of the genomes equal to the (known) tumor cell fraction. Segments assigned copy number (cn) values less than or greater than 2 are potential sites of deletion or duplication. Because CNVkit is prone to making false positive calls, particularly with whole genome sequencing and especially for indels <1 Mb, we also used CNVkit to compare each spleen against the other two spleens (where we do not expect to see high-frequency structural variants). We found that use of a cutoff score (weight) of 100 kept the

number of autosomal genes with CNV calls in spleen samples below 101. Under these conditions, tumors 1, 2 and 3 displayed 13.6, 6.9 and 3.5 times as many genes in potential CNV regions, respectively, as their matched spleen samples, but even so the overlap between the three tumors was small and did not involve any genes known to be mutated, deleted or amplified in human melanoma[1] (Table 8, S10, S12). Only four genes, *Hdac1*, *Khdrbs1*, *Zcwpw1*, and *Mta3*, overlapped with any CNVs identified by BreakDancer in any tumor, and in each case the overlap was in only one tumor. The breakpoints identified by BreakDancer in three of these cases were supported by only two or three reads, suggesting a low frequency event, and in all cases the intervals predicted by BreakDancer (Table 7, S9, S11) differed greatly in size from those predicted by CNVkit (Table 8, S10, S12).

Mutational Signature Detection with SigProfiler

The COSMIC SigProfiler[31] tool was used to explore mutational signatures in each tumor. Filtered VCF files from mutect2 somatic mutation calling were imported and Single base substitution (SBS) matrices were generated and visualized using the SigProfilerMatrixGenerator function in Python (v3.8). Default parameters were used to generate the data reported in Fig S2B.

Cell isolation for single-cell RNA sequencing

Nevi-bearing *Braf*^{WT}, *Braf*$^{CA/+}$, and *Braf*$^{CA/+}$ *Pten* $^{\Delta/+}$ mice were harvested at P30 and P50 (n = 3 of each genotype). Melanoma bearing *Braf*$^{CA/+}$ (albino coat color), *Braf*$^{CA/+}$ *Pten* $^{\Delta/+}$ (albino and black coat color), and transplanted tumors were harvested when tumors reached a size that affected the health of the animal, as described above, complying with IACUC regulations. The mice were euthanized, shaved, and depilated. For non-tumor bearing samples, a 2 by 3 cm section of the back skin was retrieved, and the fat scraped off from the underside. For melanoma-bearing samples, the skin sample on top of the tumor piece was also collected, with the mouse-matched adjacent skin next to the tumor (termed “tumor-adjacent skin”) as sample-matched control.

The tumor or skin sample was then physically minced, and suspended in a gentle-macs C-tube dissociation buffer (5mL of RPMI, 50 µL of liberase 0.25 mg/mL, 116 µL of Hepes 23.2 mM, 116 µL of Sodium Pyruvate 2.32 mM, 500 µL of Collagenase :Dispase 1 mg/mL) for 50 min at 37°C incubation with gentle agitation at a speed of 85-90rpm. After initial 50 minute digestion i, 10 µL of DNaseI (23 µL was added for another 10 min of 37°C agitated incubation and then inactivated with 400 µL of fetal bovine serum and 10 µL of EDTA (1 mM). The tissue suspension was further dissociated mechanically with GentleMACS by running the setting m_imptumor_04.01 twice. The digested suspensions were filtered twice through a 70 mm strainer and dead cells removed by centrifugation at 300 x g for 15 min. The live cells were washed with 0.04% UltraPure BSA:PBS buffer, gently re-suspended in the same buffer, and counted using trypan blue and cell counter.

Library preparation for single-cell RNA sequencing

Libraries were prepared using the Chromium Single Cell 3' v2 protocol (10X Genomics). Briefly, individual cells and gel beads were encapsulated in oil droplets where cells were lysed and mRNA was reverse transcribed to 10X barcoded cDNA. Adapters were ligated to the cDNA followed by the addition of the sample index. Prepared libraries were sequenced using paired end 100 cycles chemistry for the Illumina HiSeq 4000. FASTQ files were generated from Illumina's binary base call raw output with Cell Ranger's (v2.1.0; RRID:SCR_017344) 'cellranger mkfastq' command and the count matrix for each sample was produced with 'cellranger count'.

Single-cell RNA sequencing analysis of *Braf*$^{CA/+}$; *Braf*$^{CA/+}$ *Pten*$^{\Delta/+}$ mice

47 samples *from the genotypes: wild type; Braf*$^{CA/+}$*; Braf*$^{CA/+}$ *Pten*$^{\Delta/+}$*; and Pten*$^{\Delta/+}$ were aggregated using the Seurat built-in "Merge" function to produce one count matrix. Downstream bioinformatic analysis was conducted using Seurat[76]. For quality control, cells with fewer than 200 detected genes and genes detected in less than 3 cells were discarded. We calculated the percent mitochondrial gene expression and kept cells with less than 15% mitochondrial gene expression, and cells with fewer than 4000 genes per cell. A total of 345,427 cells from the whole

skin samples passed the quality control. Each cell was then normalized using scTransform. In the final preprocessing step, we regressed out cell-cell variation driven by mitochondrial gene expression and cells with few genes captured using the number of detected UMI. To identify cell-type clusters, principal component analysis using highly variable genes, Louvain clustering, and visualization with Uniform Manifold Approximation and Projection (UMAP) was used. For generating differentially expressed gene heatmaps, cells were downsampled to 200 cells. The Euclidean distances between clusters was calculated using the average principal component (PC) embedding for each cluster, from the top 10 PCs.

Copy Number Variant Inference Analysis

InferCNV package (version 1.20.0) was used to infer CNVs from single-cell RNA sequencing profiles from three Albino *Braf*$^{CA/+}$ mice with tumors were used, along with their mouse-matched skin samples. Fibroblasts were used as the reference cell group, whereas melanocytes, LNM cells, tumor cells, endothelial cells, erythrocytes, T cells, and macrophages are used as observation cell groups. To minimize noise from sparse matrices, cells with less than 6300 UMI counts were filtered out, and the *Braf* gene was removed from the count matrix as the expression of this gene would be altered by recombination. As advised (https://github.com/broadinstitute/inferCNV), cut-off was set as 0.1. All other default parameters were used except for window_width = 151 to facilitate visualization and BayesMaxPNormal = 0.2 to include only those inferred CNVs with high confidence.

Immunofluorescence

Formalin fixed paraffin embedded sections were sectioned 6 μm and placed on poly-L-Lysine glass slides (New Erie Scientific LLC, NH). Slides were dried overnight, and paraffin was removed with xylene followed by rehydration. Antigen retrieval was carried out by heating slides to 80°C for 50 min in 0.1M Tris-based (pH 9.0) (Vector Lab, CA). Melanin bleaching was performed using 3% H2O2 overnight at room temperature, followed by stop reaction using 1%

of acetic acid. True black lipofuscin autofluorescence quencher was then applied for 30 second. Protein block was carried out using either 10% normal goat serum in 1x PBS for 1 hr. Samples were then incubated with primary antibody *Pten* (1:100) (Cell Signaling Tech, MA) overnight at 4°C, followed by incubations with Alex fluor 594 secondary antibodies (1:1000) (Life technology, CA) and 0.5ng/ml of DAPI for 1 hour at room temperature. Slides were washed with 1X PBS three times before mounting with prolong gold antifade reagent. Slides were viewed using the Keyence BZ-X810 Wide-Field Microscope in the Stem Cell Research Center at the University of California, Irvine (UCI). Images were captured at high resolution with the same exposure time.

Histopathology and Immunohistochemistry staining

For immunohistochemistry, formalin fixed paraffin embedded sections were sectioned around 5µm - 8 µm thick onto poly-L-Lysine coated slides in a tissue water bath at a temperature of 31 to 37°C. Slides were deparaffinized with Xylene and dehydrated in a series of ethanol washes with increasing concentration. Antigen retrieval was performed with 10 mM citric acid buffer at pH 6.0 for 50 min in a 80°C water bath, then left to cool overnight at room temperature. All samples were next incubated with the primary antibody overnight at 4°C. Samples were washed and incubated with the appropriate secondary antibody. H and E staining was performed using standard histopathological methods[77].

RNAscope Fluorescence In Situ Hybridization

RNAscope Fluorescence In situ hybridization[78] was performed using the RNAscope Multiplex Fluorescent Reagent Kit v2 (catalog 320293). Briefly, formalin fixed paraffin embedded sections were sectioned around 7 µm thick onto poly-L-Lysine coated slides in a tissue water bath at a temperature of 37°C. Slides were dried overnight in a 37°C incubator, baked at 60°C for 2 hours,

and then deparaffinized two times with xylene for 5 minutes, and two times with 100% EtOH for 2 minutes. After H202 treatment at room temperature for 10 minutes, samples were boiled for target retrieval for 15 minutes, and permeabilized using protease at 40°C for 30 minutes. Samples were then incubated with Aqp1 (C2) and Sox2 (C3) probes at 40°C for 2 hours. The C2 and C3 signals were detected using Opal-620 (Akoya Biosciences) and Opal-650 (Akoya Biosciences) respectively. Dapi was used to stain the nuclei and prolong gold solution was used to mount the slides. Images were acquired using a Leica SP8 Microscope (25× water objective).

Congenic Tumor Transplantation

Melanoma-bearing Albino *Braf*$^{CA/+}$ and Black *Braf*$^{CA/+}$ *Pten* $^{\Delta/+}$ donor mice were euthanized, shaved, and depilated when tumors reached around 10% of body weight. After each tumor was collected, it was cut into pieces (weighing around 0.02g-0.06g) in a cake-slice pattern to preserve tumor structural heterogeneity; this was performed in a biosafety cabinet to ensure a sterile environment. The pieces were then washed twice with 70% EtOH, and once with 1x PBS, each for 10 seconds. They were then transferred to RPMI + 10% FBS media on ice until transplantation.

NSG recipient mice (JAX 005557) were anesthetized using Isoflurane. The tumor piece was transplanted to the back flank skin by cutting a small incision and slipping the tumor tissue in together with 100 µL of Matrigel into the skin. This was done after the mouse was shaved and sanitized with 100% EtOH and chlorhexidine diacetate disinfectant solution. Transplantation shams were also included (n=1-2 per group) by only transplanting 100 µL of Matrigel to the mouse back. 10 µL of lidocaine was applied to the wound for three consecutive days after the procedure. Tumor size was measure weekly.

Single-cell RNA sequencing Data Integration of Transplanted NSG tumors

A total of 15 scRNA-seq samples from primary Albino *Braf*$^{CA/+}$ *Pten* $^{\Delta/+}$ tumors (n=4), tumor transplantation series 1 (donor: Albino *Braf*$^{CA/+}$ mice, n=3; host: NSG mice; 1 round of transplants;

n=2) and Tumor transplantation series 2 (donor: Black *Braf*$^{CA/+}$ *Pten*$^{\Delta/+}$; host: NSG ; 2 rounds of transplants; n=2 for each) were merged using Seurat Merge function and integrated with Harmony[49] (v1.2.0).The remaining pre-processing and bioinformatic analysis were performed as described above. The Euclidean distances between clusters was calculated using the average Harmony embedding for each cluster, from the top 30 Harmony space embeddings.

Generation of *Braf*$^{CA/+}$ *Pten*$^{\Delta/+}$ *Sox2*-deficient mice

Sox2-floxed mice were purchased from Jackson laboratories (STOCK Sox2tm1.1Lan/J strain#:013093) and crossed to *Braf*$^{CA\text{-}fl/+}$ *Pten*$^{fl/+}$ mice. These mice were backcrossed into a pure C57BL/6 background for greater than six generations to generate *Braf*$^{CA\text{-}fl/+}$ *Pten*$^{fl/+}$ *Sox2*$^{fl/fl}$ mice. Induction of tumors in these mice was performed as described above.

Membership score analysis

To quantify how well cell types identified by single cell RNA sequencing fit a proposed gene expression signature, we first converted gene expression values to modified, corrected Pearson residuals, as described[79]. We then empirically determined estimates for the coefficient of variation of biological gene expression noise of 0.55, 0.65, 0.65 respectively, for *Albino Braf*$^{CA/+}$, *Albino Braf*$^{CA/+}$ *Pten*$^{\Delta/+}$, and *Black Braf*$^{CA/+}$ *Pten*$^{\Delta/+}$ samples, respectively. Residuals were then standardized, essentially converting them to z-scores. The average of the z-scores for all of the genes in any proposed gene signature was then calculated for each cell, and this value was plotted as a color-score on the UMAP diagram of the cells. The compared signatures are in Table 19-20.

RNA velocity analysis

The scVelo package[58] (version 0.2.5) was used for RNA velocity analysis. To estimate the velocity based on unspliced and spliced counts, we applied "dynamical" mode which uses differential equations to model the transient dynamics of gene expression and splicing, with other parameters set as default. Pseudotime was calculated by the "velocity_pseudotime" function with default parameters. The streamlines of velocity were visualized using "velocity_embedding_stream"

function with parameter density set as 1. Cell lineage analysis was then performed by Partition-based graph abstraction (PAGA) (provided in scVelo package) based on the calculated velocities.

MuTrans analysis

For MuTrans analysis[59], we used all cells in the Black *Braf*$^{CA/+}$ *Pten*$^{\Delta/+}$ sample and subsampled 20% cells from the two transplanted NSG mouse tumor samples. The number of attractors were determined by EPI (eigen-peak index) of MuTrans. The cellular random walk was constructed using cosine similarity of gene expression as the input to MuTrans. The dynamical manifold was constructed using default parameters based on UMAP dimension reduction coordinates as the initial values. Transition gene analysis was performed using the "GeneAnalysis" module in MuTrans, with parameter "thresh_de_pvalues" set as $5e^{-4}$ and all other parameters kept as default.

Statistical analysis

Kaplan Meier survival curves were generated, and significance assessed using the log-rank test, an unpaired t-test, or a two-way ANOVA test. Other data were analyzed by GraphPad Prism6 statistical analysis software using an unpaired t-test or two-way ANOVA test. Significance levels were as indicated.

Author contributions

ADL and AKG conceptualized the study. HX, JS, CC, SST, and RRV curated the data. HX, JS, CC, JW, PZ, SST, RRV, and ADL conducted the formal analysis. HX, JS, and CC carried out the investigation. HX, ADL, and AKG wrote the original draft. HX, JW, PZ, ADL, and AKG reviewed and edited the manuscript. ADL and AKG acquired funding for the project. ADL, PZ, JW, and QN developed the methodology. ADL and AKG administered the project.

Acknowledgement and Funding

This work was supported by NIH CA217378, CA244571, and P30AR075047. HX was supported by CIRM under Award EDUC4-12822. RRV was supported by the UC Presidents fellowship and a

FORD Foundation Fellowship. QN was partly supported by supported by NSF grants DMS1763272 and a Simons Foundation grant (594598). This work was made possible, in part, through access to the Genomics High Throughput Facility Shared Resource of the Cancer Center Support Grant (CA-62203) at the University of California, Irvine and NIH shared instrumentation grants 1S10RR025496-01, 1S10OD010794-01, and 1S10OD021718-01. Biorender was used for schematics.

Data Availability

The WGS and scRNA-seq data that support the findings of this study are available in the SRA repository under BioProject

accession code PRJNA1172319 and in the GEO repository under accession code GSE279468.

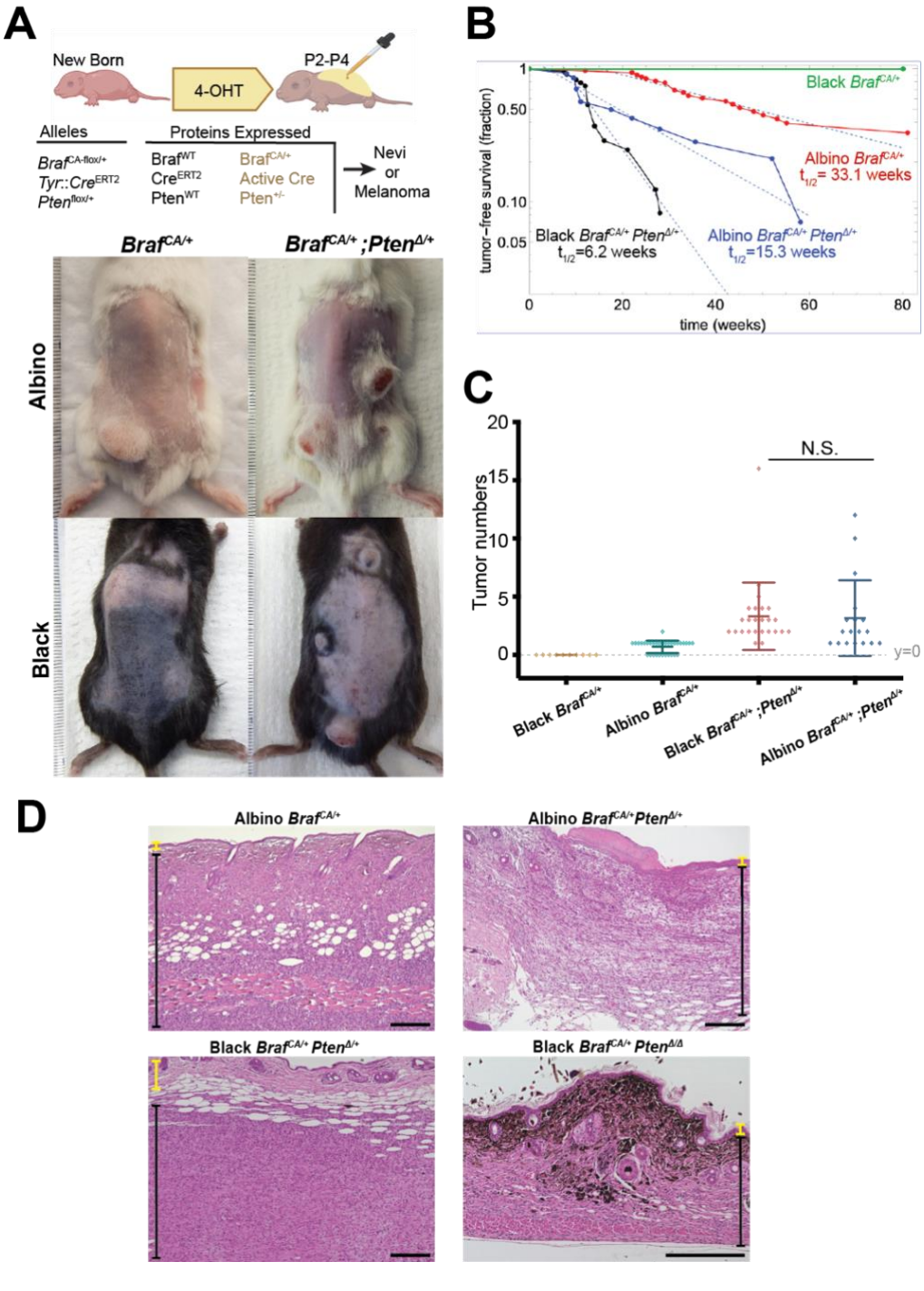
A
New Born
4-OHT
P2-P4
Alleles
Proteins Expressed
Nevi or Melanoma
Albino
Black
B
Black Braf
Albino Braf
t1/2= 33.1 weeks
Black Braf Pten
t1/2=6.2 weeks
Albino Braf Pten
t1/2=15.3 weeks
tumor-free survival (fraction)
time (weeks)
C
N.S.
Tumor numbers
y=0
D
Albino Braf
Albino Braf Pten
Black Braf Pten
Black Braf Pten

Figure 2.1. The *Braf*$^{CA/+}$ mutation can induce melanomas in mice, in an albino background, or with another allele loss in *Pten* tumor suppressor gene. A. Images and **B.** tumor-free survival curves for *Braf*$^{CA/+}$ and *Braf*$^{CA/+}$;*Pten*$^{\Delta/+}$ mice in different coat-color backgrounds. Albino *Braf*$^{CA/+}$ mice develop tumors not observed in congenic black *Braf*$^{CA/+}$ mice. **C.** Numbers of tumors per animal of *Braf*$^{CA/+}$ and *Braf*$^{CA/+}$; *Pten*$^{\Delta/+}$ models in different coat-color backgrounds. **D.** H&E staining of tumors. Yellow and black brackets on the side denote tumor-free and tumor-containing regions, respectively. Note that different tumor genotypes differ markedly in pigmentation. *Pten*$^{\Delta/\Delta}$ tumors are highly pigmented whereas *Pten*$^{\Delta/+}$ tumors largely lack pigment. Scale bar: 200um.

A

CNV type	Tumor #1	Tumor #2	Tumor #3
Deletion	46	99	88
Insertion	0	197	0
Inversion	365	279	264
Intrachromosomal translocation	111	157	457
Shared CNV	*Thrb* - inconsistent variants, does not affect enhancer or coding sequence		

B

Mutation	Tumor #1	Tumor #2	Tumor #3
Total mutations	14056	4114	4735
Intergenic	7928	2768	3188
Intronic	5229	1061	1240
Exonic	110	27	25
- Nonsynonymous	42	21	12
- Shared nonsynonymous	0		

C

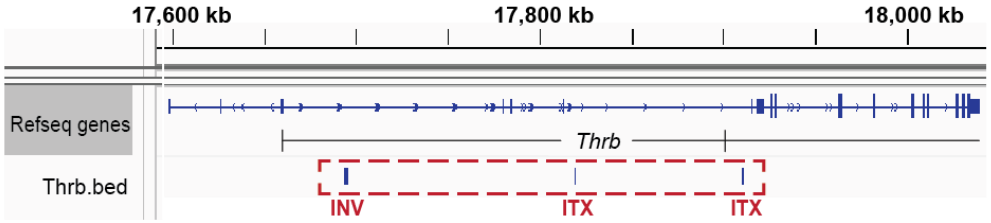

Figure 2.2. The albino *Braf*$^{CA/+}$ tumors arise independently of additional mutations. A. Whole-genome sequencing (WGS) was performed on three albino *Braf*$^{CA/+}$ tumors (80X coverage). Observed mutations (intergenic, intronic, exonic, and non-synonymous), including single nucleotide variant (SNV), insertion, deletion, substitution, and stop gain are reported. No non-synonymous mutations were shared amongst the tumors. **B.** The nearest gene bodies to detected copy number variants in albino *Braf*$^{CA/+}$ tumors were determined. Only one gene, *Thrb*, has CNVs close to the gene body in all three tumors. The locations of these CNVs did not suggest functional significance and did not overlap. **C.** Mapping of *Thrb* structural variants described in Fig. 2B. Note the variant types are inconsistent and the variant regions do not overlap. INV: Inversion. ITX: Intrachromosomal translocation. *Thrb* expression in the tumor cells of these samples is only barely detectable and is much lower than in other cell types (see Fig 7C).

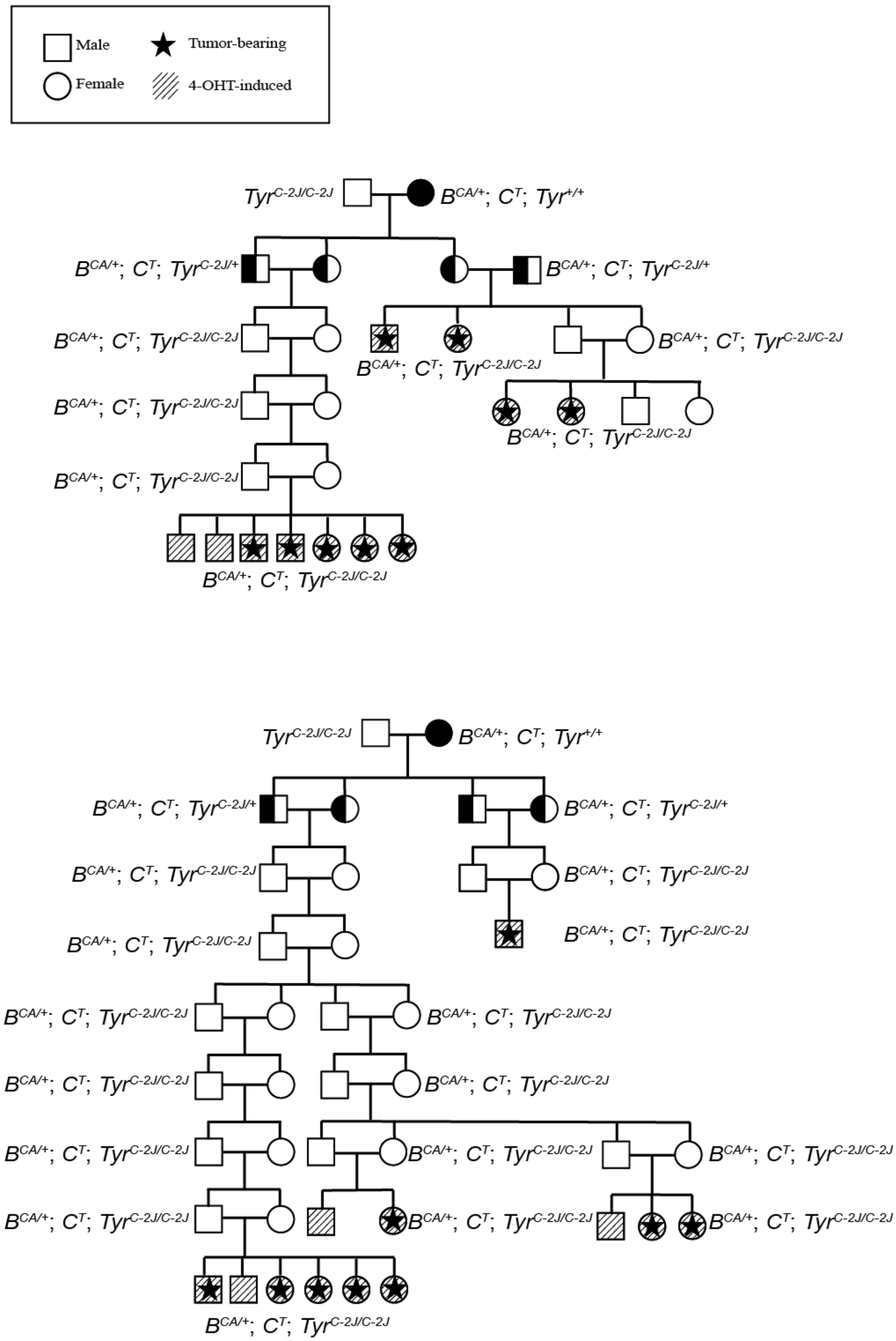
Male
Female
Tumor-bearing
4-OHT-induced
$Tyr^{C-2J/C-2J}$
$B^{CA/+}$; C^{T}; $Tyr^{+/+}$
$B^{CA/+}$; C^{T}; $Tyr^{C-2J/+}$
$B^{CA/+}$; C^{T}; $Tyr^{C-2J/C-2J}$

Figure 2.3. Mouse family tree depicting the breeding scheme used to generate the Albino *Braf*$^{CA/+}$ mice. B: *Braf*. CT: *Tyr::CreERT2*.

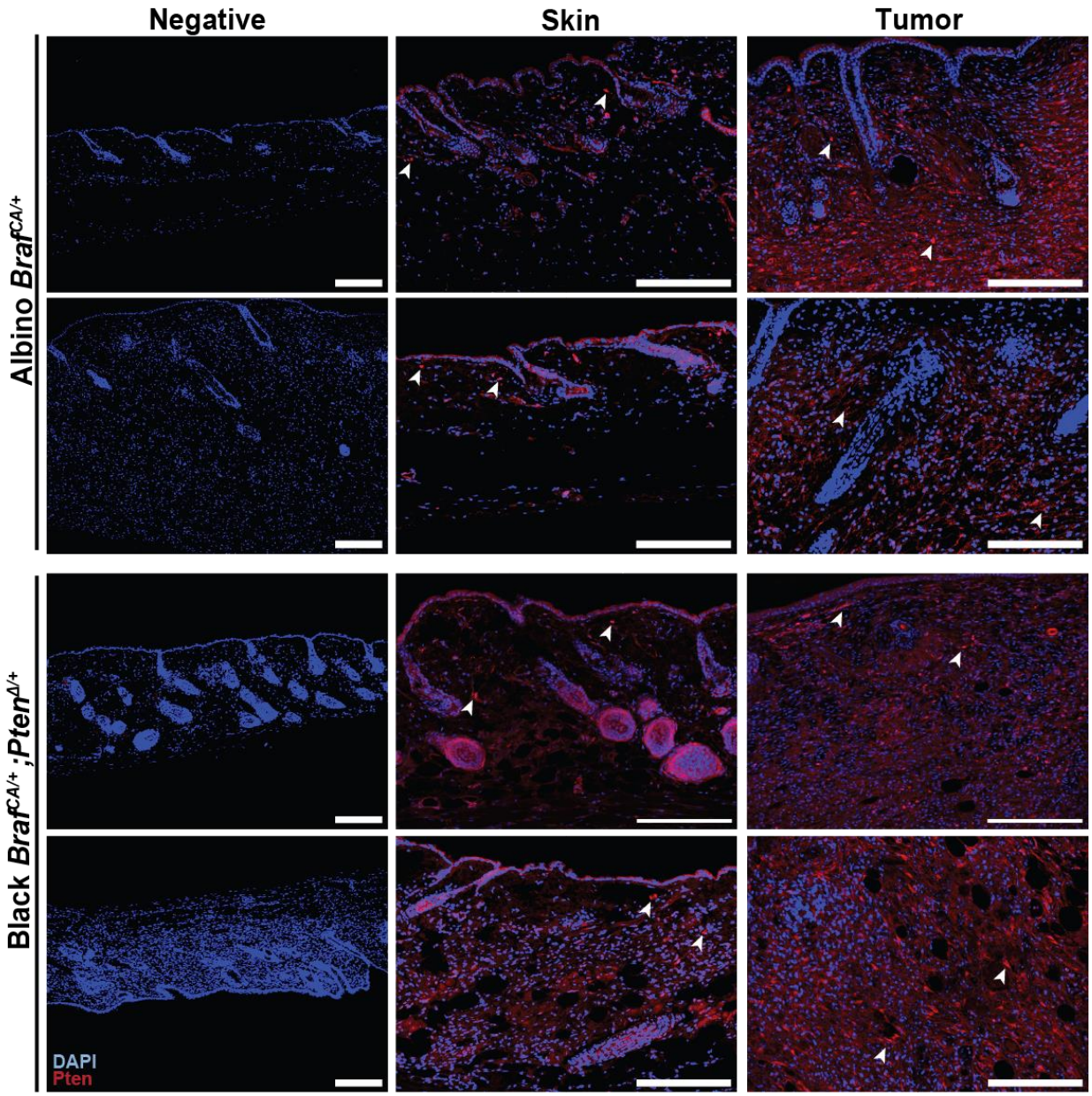
Negative
Skin
Tumor
Albino Braf^CA/+
Black Braf^CA/+;Pten^Δ/+
DAPI
Pten

Figure 2.4. Immunostaining showing *Braf*$^{CA/+}$ tumors retain Pten expression. Two representative albino *Braf*$^{CA/+}$and black *Braf*$^{CA/+}$;*Pten*$^{\Delta/+}$ tumors and adjacent skin were stained with a Pten antibody (red staining indicated by white arrows). Scale bar: 200um. B. The number of single base substitutions from three Albino *Braf*$^{CA/+}$ tumors subjected to whole genome sequencing were analyzed by SigProfiler to identify mutational signatures. The trinucleotide contexts of each mutation are shown in the x-axis. Mutations are categorized by the transcribed or untranscribed strand. Subs: substitutions.


C>A
C>G
C>T
T>A
T>C
T>G
Number of Single Base Substitutions
Tumor #1: 3,404 transcribed subs
Genic-transcribed Strand
Genic-untranscribed Strand
Tumor #2: 403 transcribed subs
Genic-transcribed Strand
Genic-untranscribed Strand
Tumor #3: 603 transcribed subs
Genic-transcribed Strand
Genic-untranscribed Strand

Figure 2.5. The number of single base substitutions from three Albino *Braf*$^{CA/+}$ tumors subjected to WGS were analyzed by SigProfiler to identify mutational signatures. The trinucleotide contexts of each mutation are shown in the x-axis. Mutations are categorized by the transcribed or untranscribed strand. Subs: substitutions.

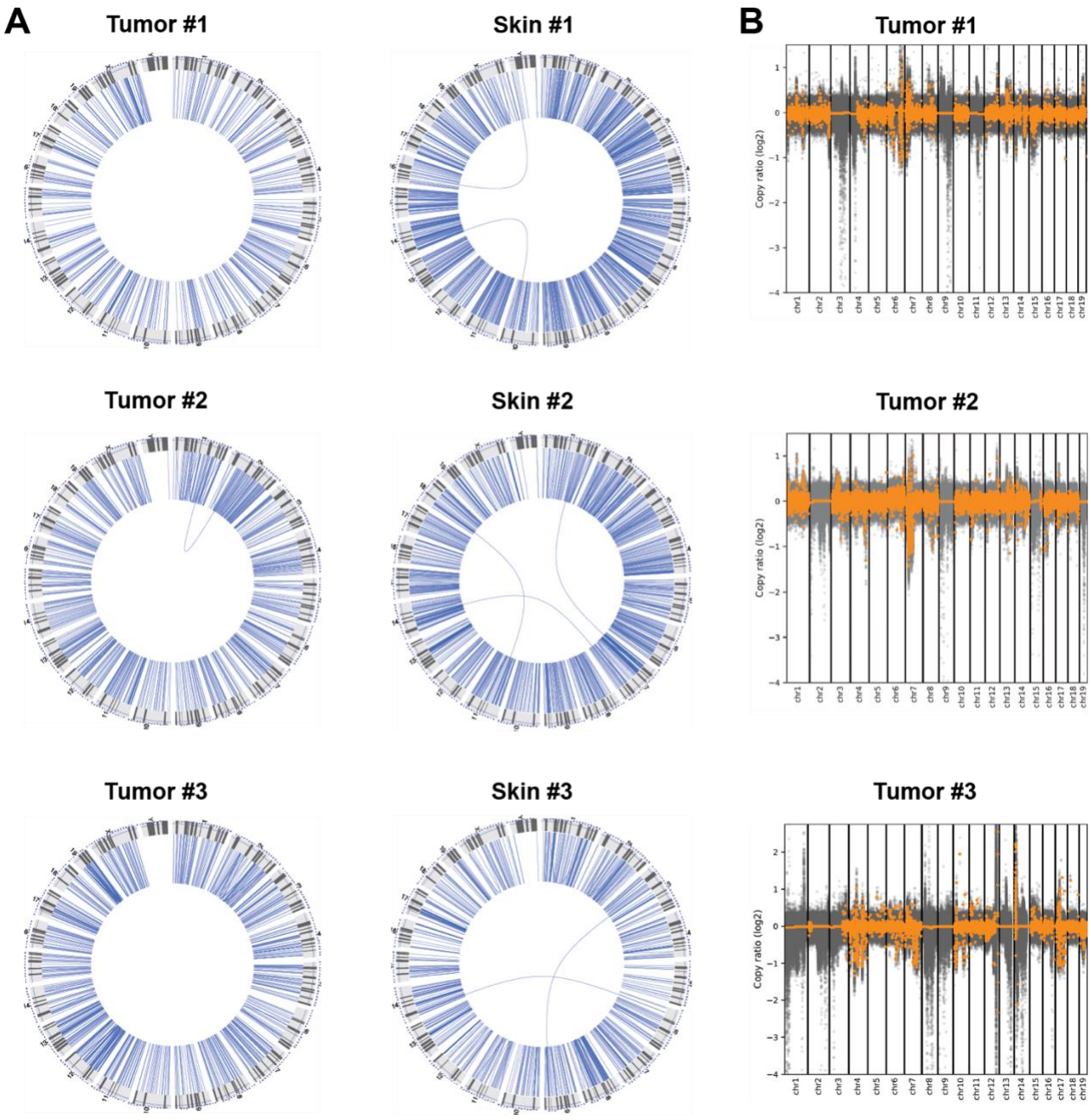
A
Tumor #1
Skin #1
B
Tumor #1
Tumor #2
Skin #2
Tumor #2
Tumor #3
Skin #3
Tumor #3
Copy ratio (log2)
chr1
chr2
chr3
chr4
chr5
chr6
chr7
chr8
chr9
chr10
chr11
chr12
chr13
chr14
chr15
chr16
chr17
chr18
chr19

Figure 2.6. A. Circos plots of structural variants identified by *BreakDancer* for the three albino *Braf*$^{CA/+}$ tumors subjected to WGS. Tumor sample structural variants were identified using both skin and spleen as control. Skin samples structural variants were identified using spleen as control. **B.** Whole genome profiles of log2 copy ratio by *CNVkit* for the three albino *Braf*$^{CA/+}$ tumors subjected to WGS. Grey dots denote bin level log coverages and orange dots denote segmentation calls by CNVkit.

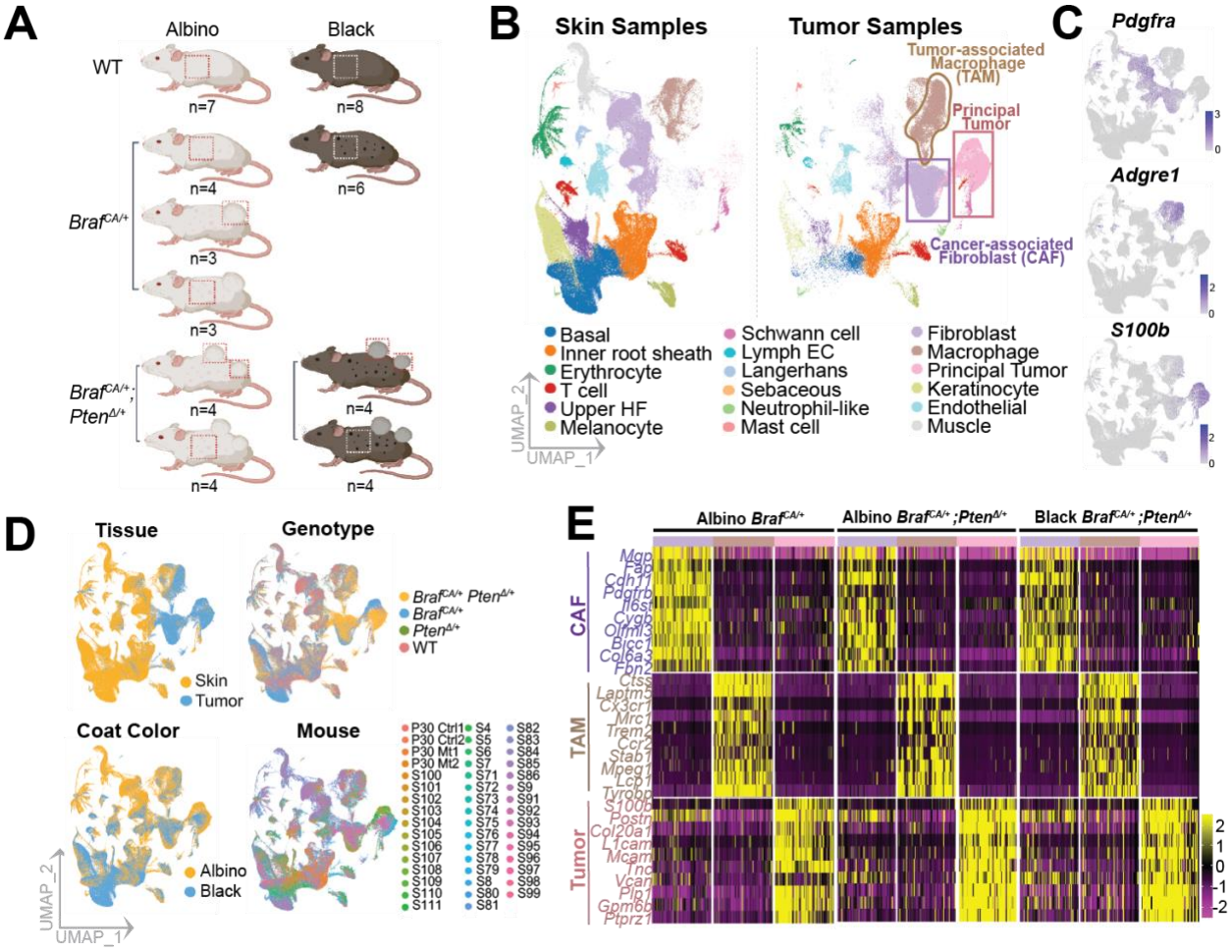
A
Albino
Black
WT
n=7
n=8
n=4
n=6
BrafCA/+
n=3
n=3
BrafCA/+;
PtenΔ/+
n=4
n=4
n=4
n=4
B
Skin Samples
Tumor Samples
Tumor-associated Macrophage (TAM)
Principal Tumor
Cancer-associated Fibroblast (CAF)
Basal
Inner root sheath
Erythrocyte
T cell
Upper HF
Melanocyte
Schwann cell
Lymph EC
Langerhans
Sebaceous
Neutrophil-like
Mast cell
Fibroblast
Macrophage
Principal Tumor
Keratinocyte
Endothelial
Muscle
UMAP_2
UMAP_1
C
Pdgfra
Adgre1
S100b
D
Tissue
Genotype
Skin
Tumor
BrafCA/+ PtenΔ/+
BrafCA/+
PtenΔ/+
WT
Coat Color
Mouse
Albino
Black
P30 Ctrl1
P30 Ctrl2
P30 Mt1
P30 Mt2
S100
S101
S102
S103
S104
S105
S106
S107
S108
S109
S110
S111
S4
S5
S6
S7
S71
S72
S73
S74
S75
S76
S77
S78
S79
S8
S80
S81
S82
S83
S84
S85
S86
S9
S91
S92
S93
S94
S95
S96
S97
S98
S99
UMAP_2
UMAP_1
E
Albino BrafCA/+
Albino BrafCA/+;PtenΔ/+
Black BrafCA/+;PtenΔ/+
CAF
TAM
Tumor
Mgp
Fabp
Cdh11
Pdgfrb
H6st1
Cygb
Olfml3
Bicc1
Col6a3
Fbn2
Ctss
Laptm5
Cx3cr1
Mrc1
Trem2
Ccr2
Stab1
Mpeg1
Lcp1
Tyrobp
S100b
Postn
Col20a1
L1cam
Mcam
Tnc
Vcan
Plp1
Gpm6b
Ptprz1
2
1
0
-1
-2

Figure 2.7. Single cell transcriptomics identifies tumor-enriched macrophage, and fibroblast populations in *Braf*$^{CA/+}$ and *Braf*$^{CA/+}$;*Pten*$^{\Delta/+}$ tumors. A. Coat colors, genotypes and numbers of mice subjected to single-cell RNA sequencing. **B.** 345,427 cells from 36 mice (47 normal, nevus-containing skin, and melanoma samples) from the genotypes in panel A were subjected to scRNAseq, jointly clustered, and projected onto a common UMAP. ScRNA-seq identified populations enriched in tumors, highlighted in the boxed areas. HF: Hair follicle. EC: Endothelial cell. **C.** Feature plots highlighting cell-types of interest based on known marker genes: Fibroblasts (*Pdgfra*), Macrophages (*Adgre1*) and Principal tumor cells (*S100b*). **D.**UMAP distribution labeled by tissue, coat color, genotype, and mouse in the whole-skin single-cell RNA-sequencing of 345,427 cells shown in Fig 2B. Detailed mouse metadata is included in Table 13.**E.** Gene expression profiles of tumor-enriched fibroblasts (purple), macrophages (brown) and tumor cells (pink) compared among the tumor genotypes. Each column in the heatmap represents a cell from the corresponding group.

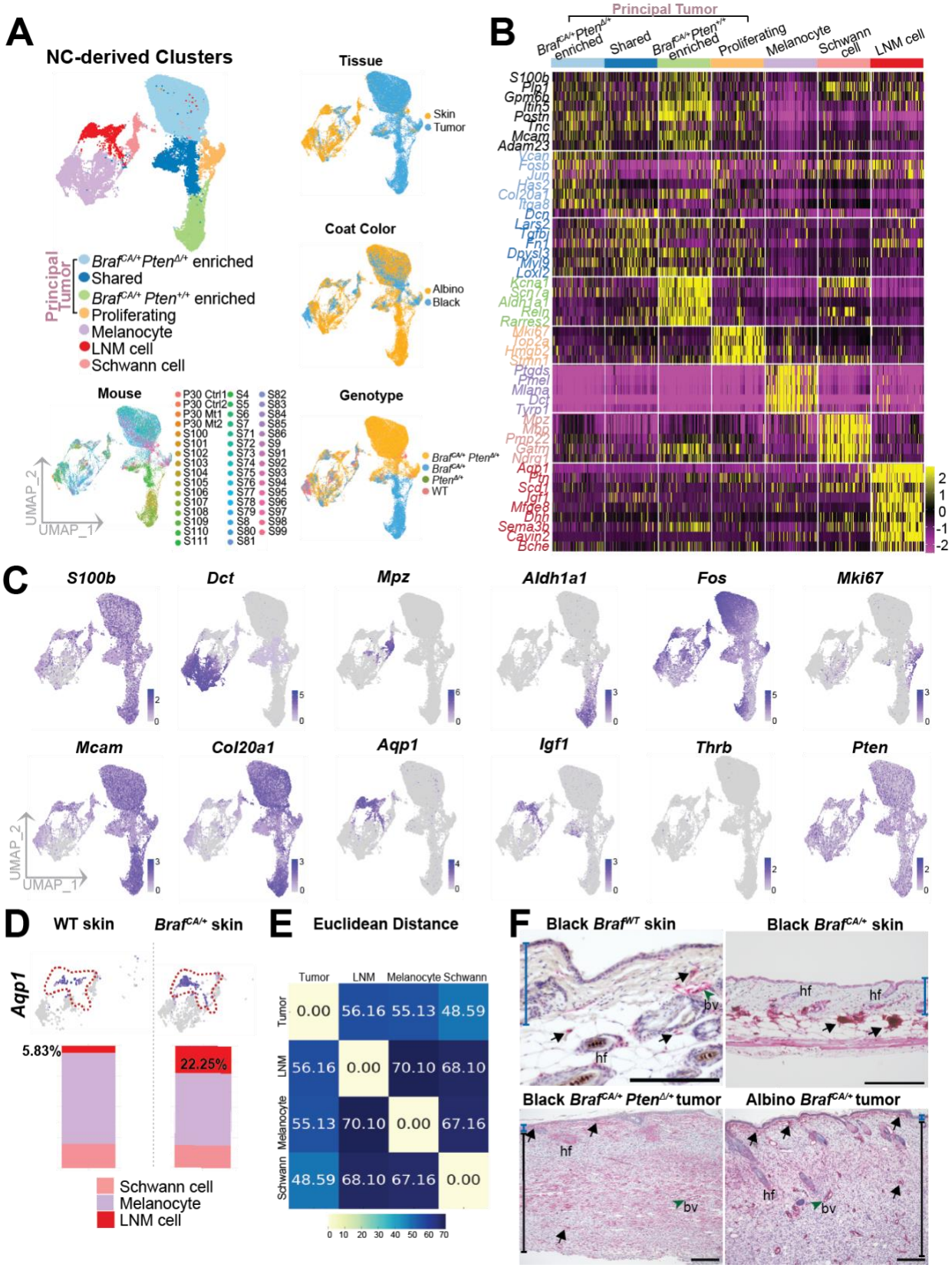
A
NC-derived Clusters
Principal Tumor
BrafCA/+Pten Δ/+ enriched
Shared
BrafCA/+ Pten+/+ enriched
Proliferating
Melanocyte
LNM cell
Schwann cell
Tissue
Skin
Tumor
Coat Color
Albino
Black
Mouse
Genotype
BrafCA/+ PtenΔ/+
BrafCA/+
PtenΔ/+
WT
UMAP_2
UMAP_1
B
Principal Tumor
Shared
Proliferating
Melanocyte
Schwann cell
LNM cell
S100b
Plp1
Gpm6b
Itih5
Postn
Tnc
Mcam
Adam23
Vcan
Fosb
Jun
Has2
Col20a1
Itga8
Dcn
Lars2
Tgfbi
Fn1
Dpysl3
Myl9
Loxl2
Kcna1
Scn1a
Aldh1a1
Rein
Rarres2
Mki67
Top2a
Hmgb2
Stmn1
Ptgds
Pmel
Mlana
Dct
Tyrp1
Mpz
Mbp
Pmp22
Gatm
Ndrg1
Aqp1
Ptn
Scd1
Igf1
Mfge8
Ehd1
Sema3b
Cavin2
Bche
C
S100b
Dct
Mpz
Aldh1a1
Fos
Mki67
Mcam
Col20a1
Aqp1
Igf1
Thrb
Pten
UMAP_2
UMAP_1
D
WT skin
BrafCA/+ skin
Aqp1
5.83%
22.25%
Schwann cell
Melanocyte
LNM cell
E
Euclidean Distance
Tumor
LNM
Melanocyte
Schwann
0.00 56.16 55.13 48.59
56.16 0.00 70.10 68.10
55.13 70.10 0.00 67.16
48.59 68.10 67.16 0.00
0 10 20 30 40 50 60 70
F
Black BrafWT skin
Black BrafCA/+ skin
Black BrafCA/+ PtenΔ/+ tumor
Albino BrafCA/+ tumor
hf
bv

Figure 2.8. Subclustering of the NC-derived cells identifies the LNM population present in WT skin and expands upon *Braf* mutation. A. NC-derived clusters (identified by the expression of *S100b*, *Dct*, *Mpz* [as well as a Cre-reporter gene in selected cases]) were further subsetted (35,527 cells in total) and populations specific to tissue, mouse, genotype and coat color were characterized. **B.** Differentially expressed genes associated with NC-derived clusters defined in panel A. Known melanoma markers are labeled in black; colored bars and other text colors correspond to labeling in C. **C.** Feature plots of the merged NC-derived clusters highlighting distinct cell-types. **D.** Feature plots of the LNM marker *Aqp1* and cell proportion plots in melanocyte cells across WT and *Braf*-mutant skin. Note the expansion of LNM cells in skin from black $Braf^{CA/+}$ mice (as tumors do not form in these mice, such cells cannot be tumor-derived) **E.** Heatmap of Euclidean distance between NC-derived clusters using embeddings from the top 10 principal components (PCs). **F.** Immunohistochemistry of LNM cells (pink staining of *Aqp1*+; black arrows). Samples were counterstained with hematoxylin. Note the strong staining in the nevi of skin samples. Note that *Aqp1* straining starts in the superficial dermis (blue bracket) and extends to the subcutis (black bracket) in tumors. hf: hair follicles. bv: blood vessels. Scale bar: 200um.

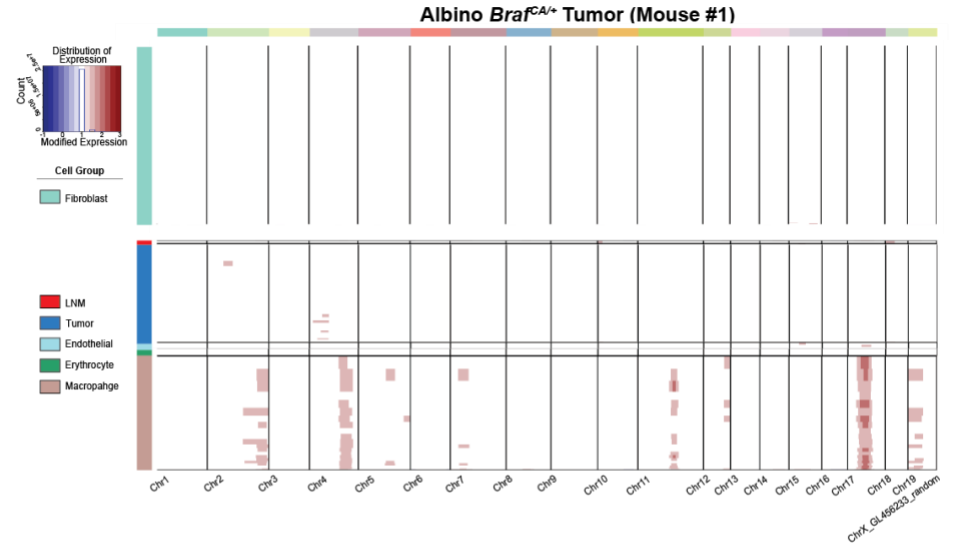
Albino Braf^CA/+ Tumor (Mouse #1)
Distribution of Expression
Count
Modified Expression
Cell Group
Fibroblast
LNM
Tumor
Endothelial
Erythrocyte
Macropahge
Chr1
Chr2
Chr3
Chr4
Chr5
Chr6
Chr7
Chr8
Chr9
Chr10
Chr11
Chr12
Chr13
Chr14
Chr15
Chr16
Chr17
Chr18
Chr19
ChrX_GL456233_random

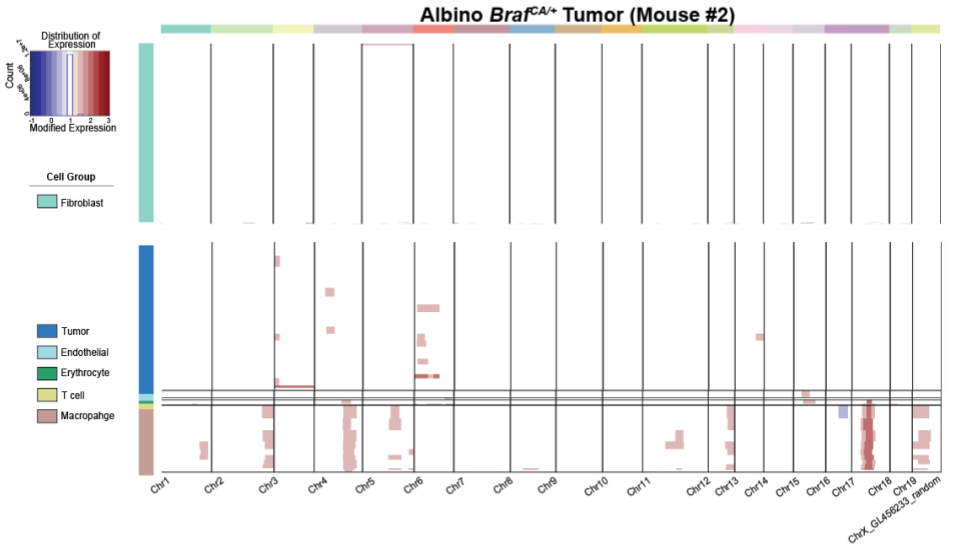
Albino Braf^CA/+ Tumor (Mouse #2)
Distribution of Expression
Count
Modified Expression
Cell Group
Fibroblast
Tumor
Endothelial
Erythrocyte
T cell
Macropahge
Chr1
Chr2
Chr3
Chr4
Chr5
Chr6
Chr7
Chr8
Chr9
Chr10
Chr11
Chr12
Chr13
Chr14
Chr15
Chr16
Chr17
Chr18
Chr19
ChrX_GL456233_random

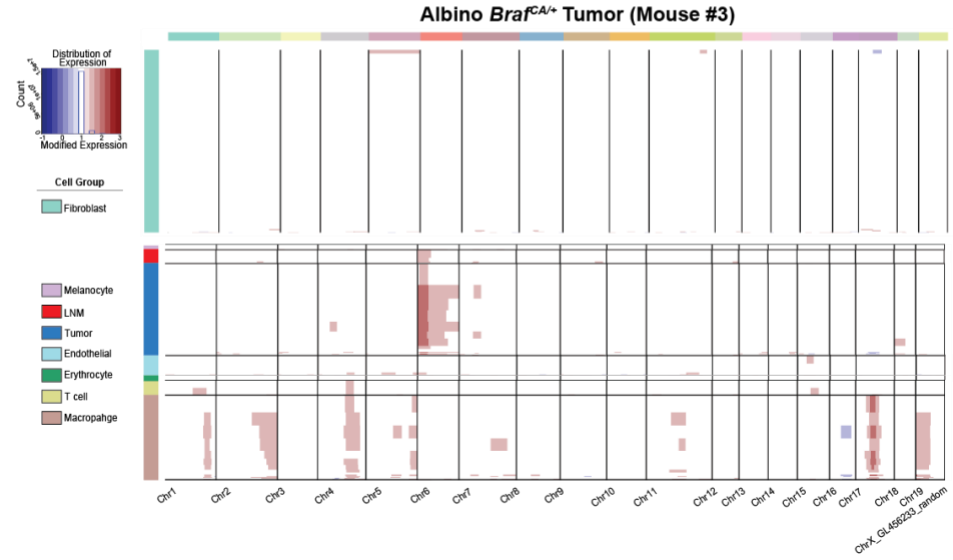
Albino Braf^CA/+ Tumor (Mouse #3)
Distribution of Expression
Count
Modified Expression
Cell Group
Fibroblast
Melanocyte
LNM
Tumor
Endothelial
Erythrocyte
T cell
Macropahge
Chr1
Chr2
Chr3
Chr4
Chr5
Chr6
Chr7
Chr8
Chr9
Chr10
Chr11
Chr12
Chr13
Chr14
Chr15
Chr16
Chr17
Chr18
Chr19
ChrX_GL456233_random

Figure 2.9. Heatmap of inferred large-scale copy number variations (CNVs) from three Albino *Braf*$^{CA/+}$ mouse tumors. InferCNV was used to identify copy number variants from single-cell RNA expression profiles. Fibroblasts were used as a normal reference, and compared with melanocytes, LNM cells, tumor cells, endothelial cells, erythrocytes, T cells, and macrophages. X-axis and Y-axis represent cell groups and chromosomes respectively. Red gradient denotes gains and blue denotes loss.

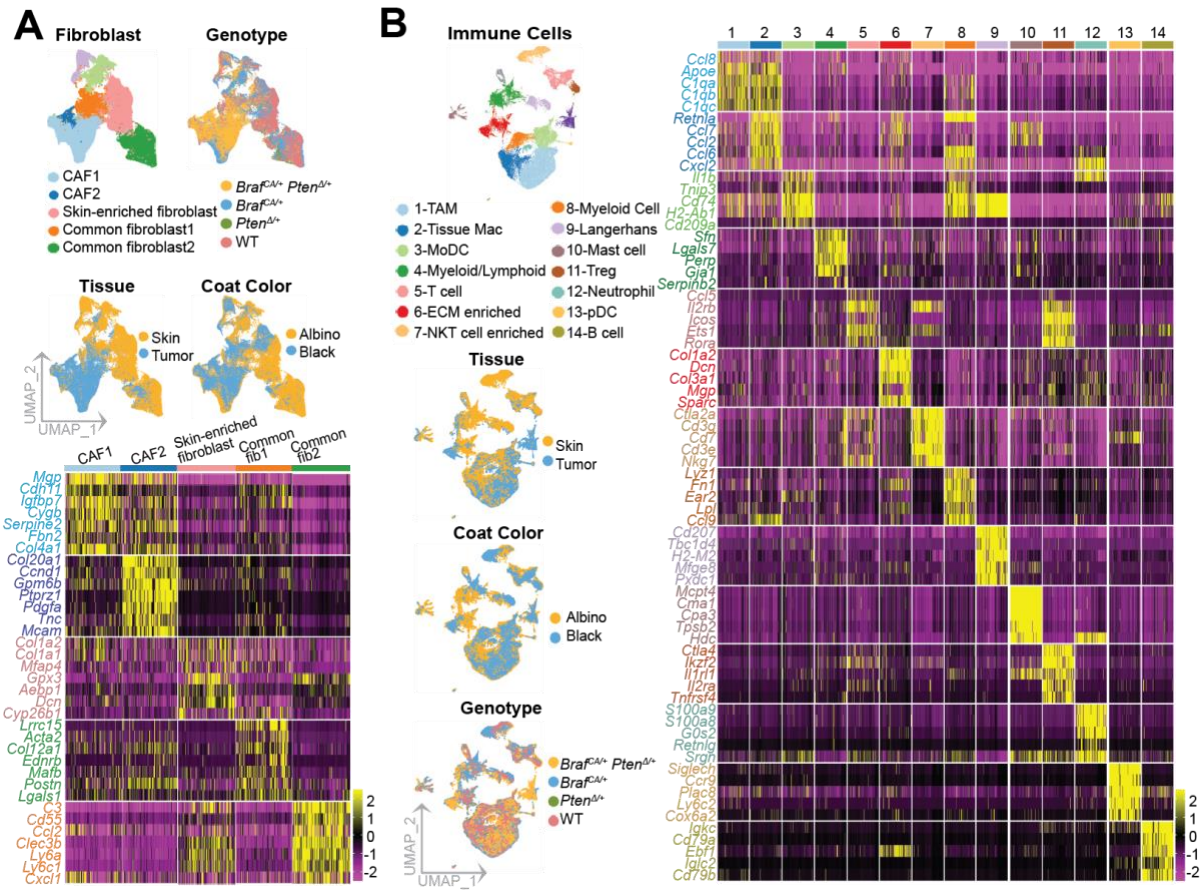
A
Fibroblast
Genotype
CAF1
CAF2
Skin-enriched fibroblast
Common fibroblast1
Common fibroblast2
Braf CA/+ Pten Δ/+
Braf CA/+
Pten Δ/+
WT
Tissue
Coat Color
Skin
Tumor
Albino
Black
UMAP_2
UMAP_1
CAF1
CAF2
Skin-enriched fibroblast
Common fib1
Common fib2
Mgp
Cdh11
Igfbp7
Cygb
Serpine2
Fbn2
Col4a1
Col20a1
Ccnd1
Gpm6b
Ptprz1
Pdgfa
Tnc
Mcam
Col1a2
Col1a1
Mfap4
Gpx3
Aebp1
Dcn
Cyp26b1
Lrrc15
Acta2
Col12a1
Ednrb
Mafb
Postn
Lgals1
C3
Cd55
Ccl2
Clec3b
Ly6a
Ly6c1
Cxcl1
2
1
0
-1
-2
B
Immune Cells
1-TAM
2-Tissue Mac
3-MoDC
4-Myeloid/Lymphoid
5-T cell
6-ECM enriched
7-NKT cell enriched
8-Myeloid Cell
9-Langerhans
10-Mast cell
11-Treg
12-Neutrophil
13-pDC
14-B cell
Tissue
Skin
Tumor
Coat Color
Albino
Black
Genotype
Braf CA/+ Pten Δ/+
Braf CA/+
Pten Δ/+
WT
UMAP_2
UMAP_1
1
2
3
4
5
6
7
8
9
10
11
12
13
14
Ccl8
Apoe
C1qa
C1qb
C1qc
Retnla
Ccl7
Ccl2
Ccl6
Cxcl2
Il1b
Tnip3
Cd74
H2-Ab1
Cd209a
Sfn
Lgals7
Perp
Gja1
Serpinb2
Ccl5
Il2rb
Icos
Ets1
Rora
Col1a2
Dcn
Col3a1
Mgp
Sparc
Ctla2a
Cd3g
Cd7
Cd3e
Nkg7
Lyz1
Fn1
Ear2
Lpl
Ccl9
Cd207
Tbc1d4
H2-M2
Mfge8
Cyb561
Mcpt4
Cma1
Cpa3
Tpsb2
Hdc
Ctla4
Ikzf2
Il1rl1
Il2ra
Tnfrsf4
S100a9
S100a8
G0s2
Retnlg
Srgn
Siglech
Ccr9
Plac8
Ly6c2
Cox6a2
Igkc
Cd79a
Ebf1
Iglc2
Cd79b
2
1
0
-1
-2

Figure 2.10. Subclustering of Immune and Fibroblast subsets. A-B. Gene expression profiles of (A) 86,536 fibroblasts and (B) 51,747 immune cells associated with the skin and tumor microenvironments, as described in Fig 6B. Cells were subclustered, visualized by UMAP, and labeled by tissue of origin, coat color, and genotype. Each column in the heatmap represents a cell from the corresponding group. CAF: cancer-associated fibroblast. Fib: fibroblast. TAM: tumor-associated macrophage. MoDC: Monocyte-derived dendritic cell. ECM: Extracellular matrix. Treg: Regulatory T cell. pDC: Plasmacytoid dendritic cell.

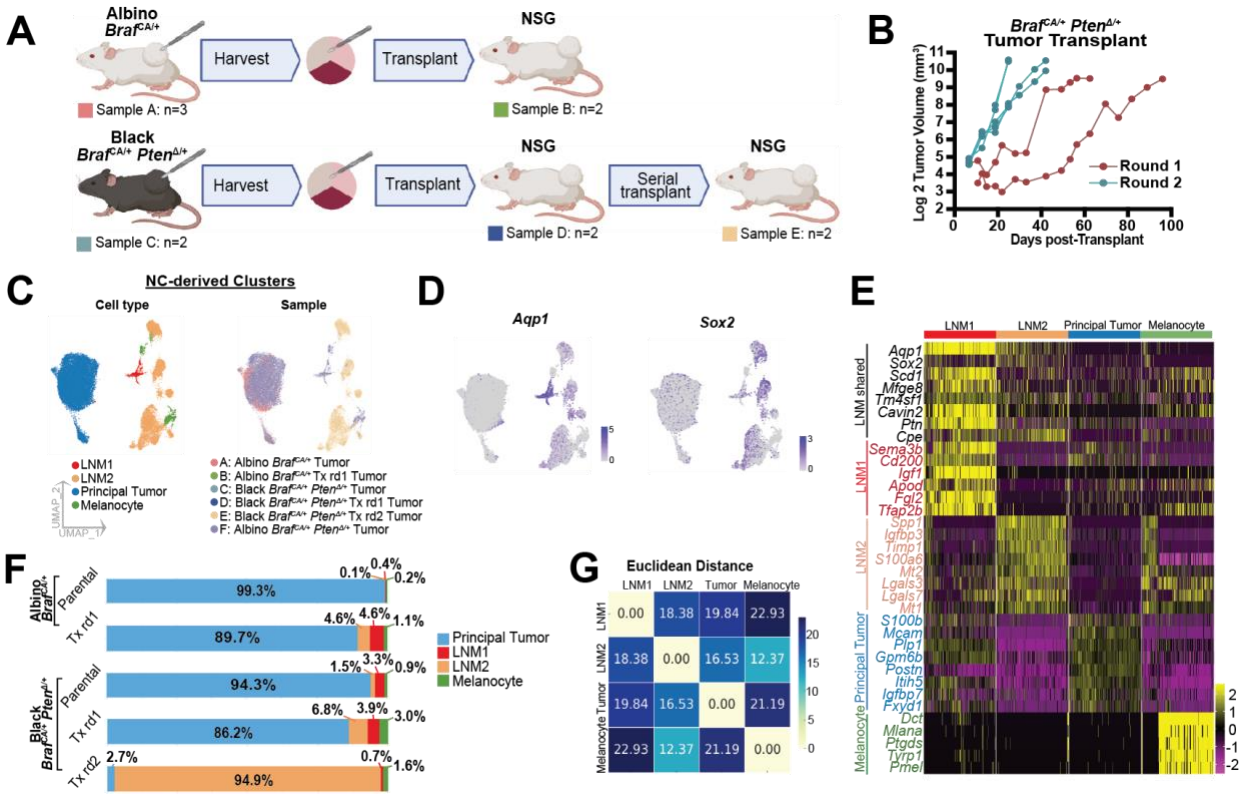
A
Albino
Braf^CA/+
Harvest
Transplant
NSG
Sample A: n=3
Sample B: n=2
Black
Braf^CA/+ Pten^Δ/+
Harvest
Transplant
NSG
Serial transplant
NSG
Sample C: n=2
Sample D: n=2
Sample E: n=2
B
Braf^CA/+ Pten^Δ/+
Tumor Transplant
Log 2 Tumor Volume (mm³)
Days post-Transplant
Round 1
Round 2
C
NC-derived Clusters
Cell type
Sample
LNM1
LNM2
Principal Tumor
Melanocyte
A: Albino Braf^CA/+ Tumor
B: Albino Braf^CA/+ Tx rd1 Tumor
C: Black Braf^CA/+ Pten^Δ/+ Tumor
D: Black Braf^CA/+ Pten^Δ/+ Tx rd1 Tumor
E: Black Braf^CA/+ Pten^Δ/+ Tx rd2 Tumor
F: Albino Braf^CA/+ Pten^Δ/+ Tumor
D
Aqp1
Sox2
E
LNM1
LNM2
Principal Tumor
Melanocyte
LNM shared
Aqp1
Sox2
Scd1
Mfge8
Tm4sf1
Cavin2
Ptn
Cpe
Sema3b
Cd200
Igf1
Apod
Fgl2
Tfap2b
Spp1
Igfbp3
Timp1
S100a6
Mt2
Lgals3
Lgals1
Mt1
S100b
Mcam
Plp1
Gpm6b
Postn
Ithh5
Igfbp7
Fxyd1
Dct
Mlana
Ptgds
Tyrp1
Pmel
F
Albino Braf^CA/+
Parental
Tx rd1
Black Braf^CA/+ Pten^Δ/+
Parental
Tx rd1
Tx rd2
99.3%
0.1%
0.4%
0.2%
89.7%
4.6%
4.6%
1.1%
94.3%
1.5%
3.3%
0.9%
86.2%
6.8%
3.9%
3.0%
2.7%
94.9%
0.7%
1.6%
Principal Tumor
LNM1
LNM2
Melanocyte
G
Euclidean Distance
LNM1
LNM2
Tumor
Melanocyte
0.00 18.38 19.84 22.93
18.38 0.00 16.53 12.37
19.84 16.53 0.00 21.19
22.93 12.37 21.19 0.00

Figure 2.11. LNM cells persist after transplantation. A. Tumors derived from *Braf*$^{CA/+}$ and *Braf*$^{CA/+}$; *Pten*$^{\Delta/+}$ mouse models were passaged by transplantation onto NSG (immune deficient) mice. **B.** Tumors were transplanted from one Black *Braf*$^{CA/+}$; *Pten*$^{\Delta/+}$ tumor into two NSG hosts and harvested (round 1). One tumor transplanted in the first round was harvested and re-transplanted into five NSG hosts (round 2). Growth curve for each tumor is recorded. Note the time delay for tumor initiation is shortened after re-transplantation. **C.** Single-cell gene expression profiles were used to subcluster NC-derived cell clusters (22,732 cells), among which both principal tumor and LNM clusters were identified. UMAP visualizations of cell-type and sample distribution are shown. Rd = Round of transplantation. Tx = transplant. **D.** Feature plots highlighting NC-derived cell types: Principal tumor cells (marked by *S100b*) and highly proliferating cells (marked by *Mki67*) are noted. **E.** Gene expression profiles of the NC-derived clusters identified in panel B. Gene signatures shared among LNM1 and LNM2 are labeled in black. Each column in the heatmap represents a cell from the corresponding group. **F.** Cell proportion plots in NC-derived clusters across sample types from two sets of transplantation experiments. Note both LNM1 and LNM2 populations are present in all samples and persist through transplantation rounds. Tx: transplant. Rd: round of transplantation. **G.** Heatmap of Euclidean distances calculated between NC-derived clusters in Fig 3B using embeddings from the top 10 principal components (PCs).

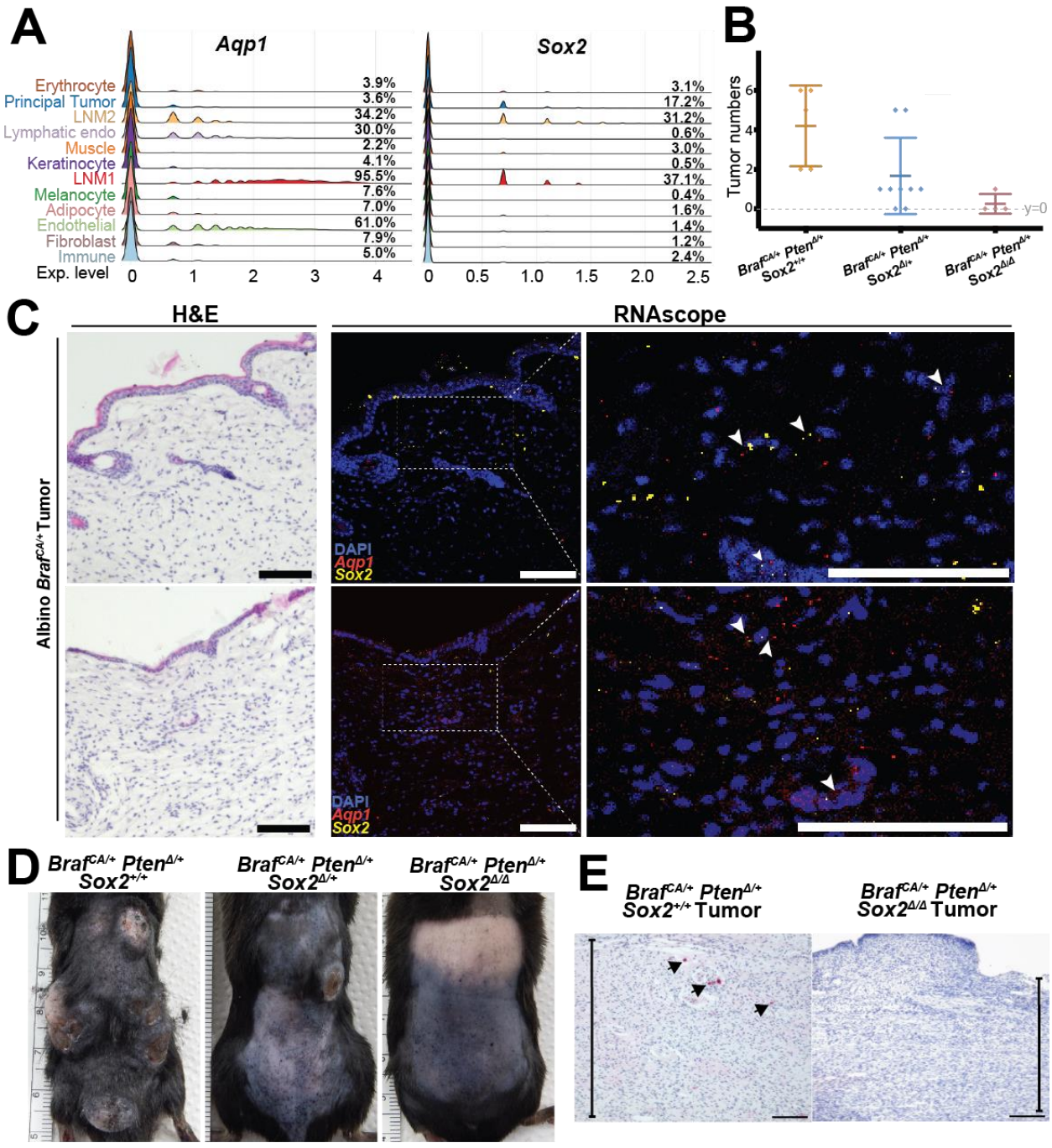
A
Aqp1
Sox2
Erythrocyte
Principal Tumor
LNM2
Lymphatic endo
Muscle
Keratinocyte
LNM1
Melanocyte
Adipocyte
Endothelial
Fibroblast
Immune
Exp. level
3.9%
3.6%
34.2%
30.0%
2.2%
4.1%
95.5%
7.6%
7.0%
61.0%
7.9%
5.0%
3.1%
17.2%
31.2%
0.6%
3.0%
0.5%
37.1%
0.4%
1.6%
1.4%
1.2%
2.4%
B
Tumor numbers
y=0
C
H&E
RNAscope
Albino BrafCA/+ Tumor
DAPI
Aqp1
Sox2
D
BrafCA/+ Pten Δ/+ Sox2+/+
BrafCA/+ Pten Δ/+ Sox2Δ/+
BrafCA/+ Pten Δ/+ Sox2Δ/Δ
E
BrafCA/+ Pten Δ/+ Sox2+/+ Tumor
BrafCA/+ Pten Δ/+ Sox2Δ/Δ Tumor

Figure 2.12. LNM cells are *Aqp1*+ and *Sox2*+, and deletion of the stem cell transcriptional factor *Sox2* inhibited tumor formation in *Braf*$^{CA/+}$; *Pten*$^{\Delta/+}$ mouse models. A. Ridge plots of *Aqp1* and *Sox2* expression across whole skin cell-types in whole skin . Note the high expression of Aqp1 and Sox2 in both LNM1 and LNM2, compared to other cell types. Percentages on the side denote the fraction of cells expressing Aqp1 and Sox2 in each cell type, respectively. Exp.: Expression. **B.** Conditional *Sox2* deletion in melanocytic/NC-derived cells inhibits tumor development. Tumor incidence in mice of the indicated genotypes is shown. **C.** RNAscope in-situ hybridization of *Aqp1* and *Sox2* in two representative Albino *Braf*$^{CA/+}$ tumors. Co-expression is marked by white arrows. Corresponding H&E staining is shown. Scale bar: 100um. **D.** Representative mice of the indicated genotypes are shown. Note the inhibition of tumor when *Sox2* is eliminated by *Tyr::CreERT2*. **E.** Tumors of the indicated genotypes were stained with a Sox2 antibody (pink staining). Note the staining indicating *Sox2* deletion in the sole *Braf*$^{CA/+}$; *Pten*$^{\Delta/+}$ *Sox2*$^{\Delta/\Delta}$ mouse tumor we found in our cohort, compared to the positive staining (indicated by arrows) in a *Sox2*-wildtype tumor. Samples are counterstained with hematoxylin. Black brackets denote tumor-containing regions. Scale bar: 100um.

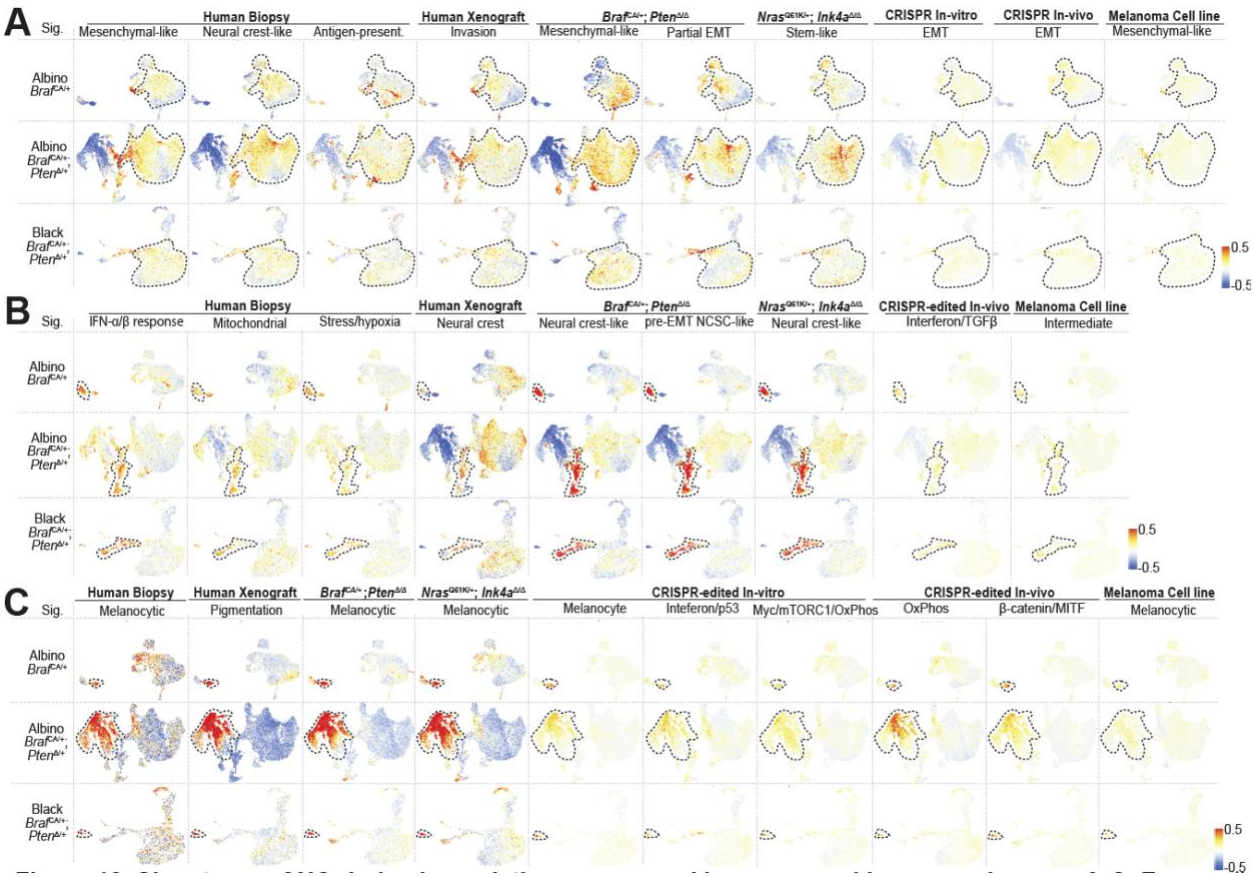
A
Sig.
Human Biopsy
Mesenchymal-like
Neural crest-like
Antigen-present.
Human Xenograft
Invasion
BrafCA/+; PtenΔ/Δ
Mesenchymal-like
Partial EMT
NrasQ61K/+; Ink4aΔ/Δ
Stem-like
CRISPR In-vitro
EMT
CRISPR In-vivo
EMT
Melanoma Cell line
Mesenchymal-like
Albino BrafCA/+
Albino BrafCA/+, PtenΔ/+
Black BrafCA/+, PtenΔ/+
0.5
-0.5
B
Sig.
Human Biopsy
IFN-α/β response
Mitochondrial
Stress/hypoxia
Human Xenograft
Neural crest
BrafCA/+; PtenΔ/Δ
Neural crest-like
pre-EMT NCSC-like
NrasQ61K/+; Ink4aΔ/Δ
Neural crest-like
CRISPR-edited In-vivo
Interferon/TGFβ
Melanoma Cell line
Intermediate
Albino BrafCA/+
Albino BrafCA/+, PtenΔ/+
Black BrafCA/+, PtenΔ/+
0.5
-0.5
C
Sig.
Human Biopsy
Melanocytic
Human Xenograft
Pigmentation
BrafCA/+; PtenΔ/Δ
Melanocytic
NrasQ61K/+; Ink4aΔ/Δ
Melanocytic
CRISPR-edited In-vitro
Melanocyte
Inteferon/p53
Myc/mTORC1/OxPhos
CRISPR-edited In-vivo
OxPhos
β-catenin/MITF
Melanoma Cell line
Melanocytic
Albino BrafCA/+
Albino BrafCA/+, PtenΔ/+
Black BrafCA/+, PtenΔ/+
0.5
-0.5

Figure 2.13. Signatures of NC-derived populations conserved in mouse and human melanoma. A-C. Every cell was assigned a score for how well its gene expression fit a published gene expression signature[18, 22, 55], relative to the other NC-derived cell types (see Methods and Table 10) and these were overlayed on the UMAPs for each of the tumor genotypes (red=strong agreement; blue=poor agreement). Gene signatures that aligned primarily with principal tumor cells are shown in A; those that aligned strongly with LNM cells are shown in B and those that aligned with melanocytes are shown in C. Black dashes outline cell-types in the individual datasets. EMT: Epithelial-mesenchymal transitions. NCSC: Neural crest stem-cell. OxPhos: Oxidative phosphorylation. Sig: signature.

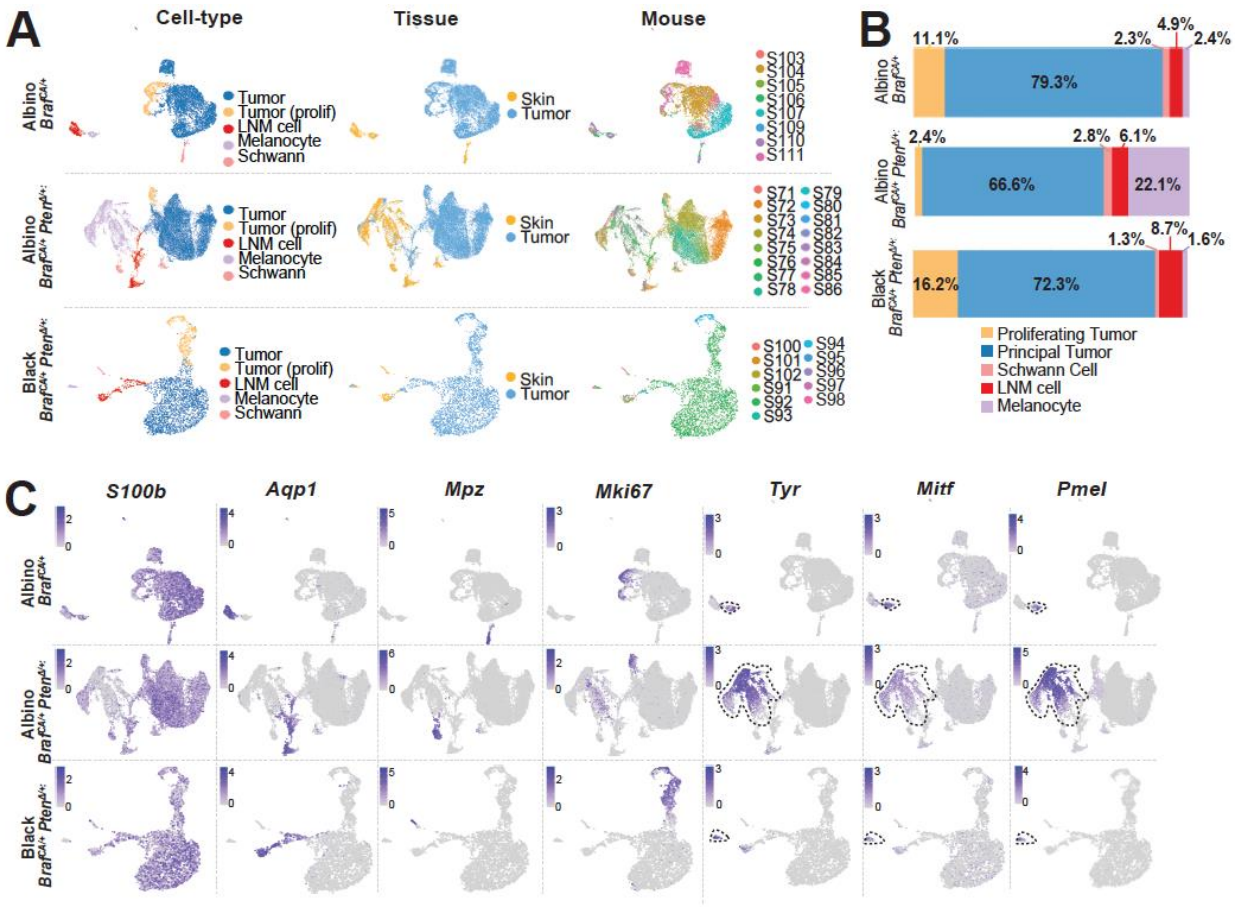
A
Cell-type
Tissue
Mouse
Albino Braf
Albino Braf Pten
Black Braf Pten
Tumor
Tumor (prolif)
LNM cell
Melanocyte
Schwann
Skin
Tumor
B
11.1%
79.3%
2.3%
4.9%
2.4%
2.4%
66.6%
2.8%
6.1%
22.1%
16.2%
72.3%
1.3%
8.7%
1.6%
Proliferating Tumor
Principal Tumor
Schwann Cell
LNM cell
Melanocyte
C
S100b
Aqp1
Mpz
Mki67
Tyr
Mitf
Pmel

Figure 2.14. NC-derived cells in Albino *Braf*$^{CA/+}$, Albino *Braf*$^{CA/+}$; *Pten*$^{\Delta/+}$, and Black *Braf*$^{CA/+}$; *Pten*$^{\Delta/+}$ tumor and skin datasets. A. The tissue and mouse source distribution of NC-derived clusters from three genotypes: Albino *Braf*$^{CA/+}$ (21,600 cells), Albino *Braf*$^{CA/+}$; *Pten*$^{\Delta/+}$ (5973 cells), and Black *Braf*$^{CA/+}$; *Pten*$^{\Delta/+}$ (3926 cells), is shown. Prolif: proliferating. **B.** Cell proportion plots of NC-derived clusters across three datasets in A. **C.** Feature plots of expression of selected pigmentation genes in the three tumor datasets.

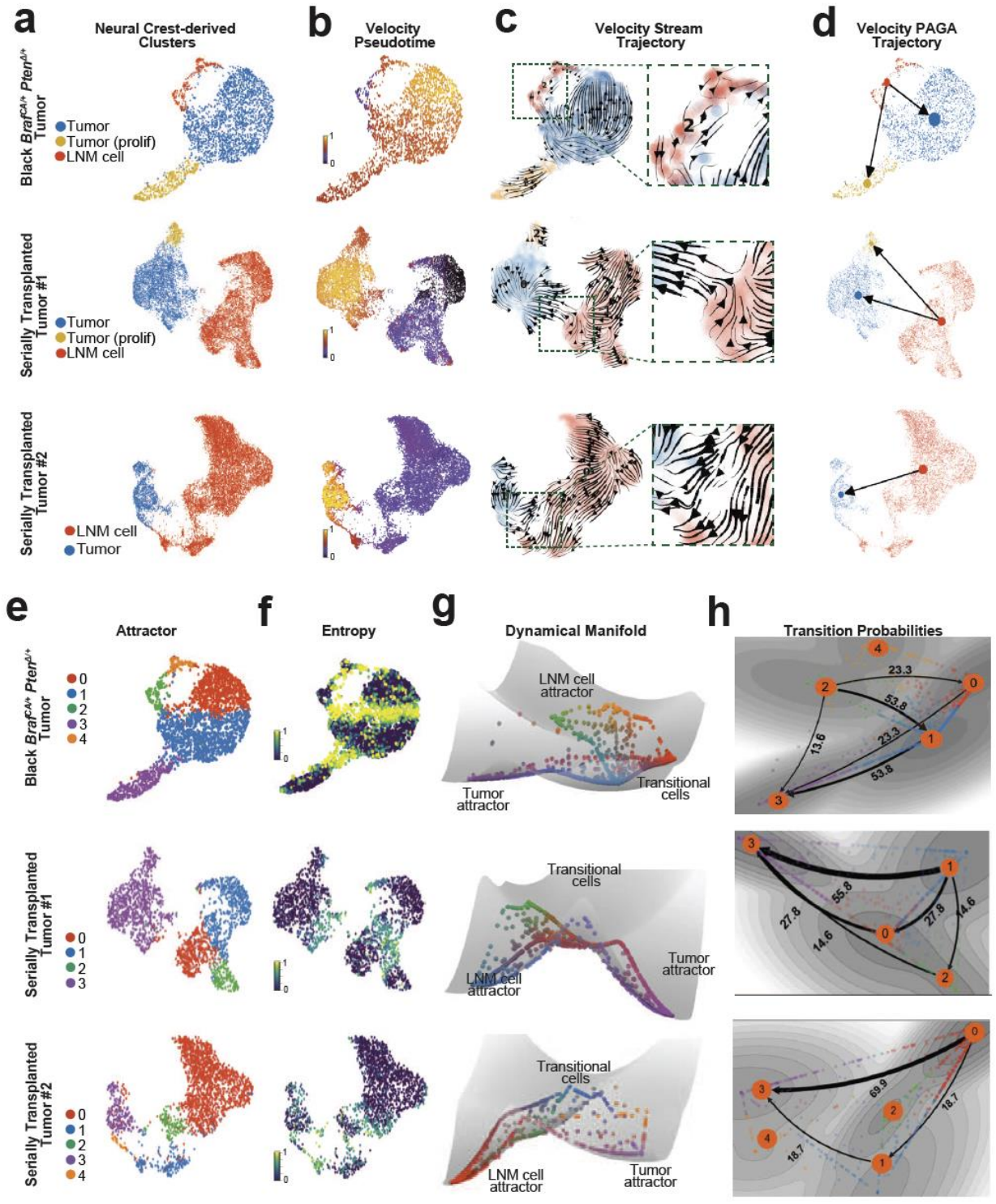
a
Neural Crest-derived Clusters
b
Velocity Pseudotime
c
Velocity Stream Trajectory
d
Velocity PAGA Trajectory
Black BrafCA/+ PtenΔ/+ Tumor
Tumor
Tumor (prolif)
LNM cell
Serially Transplanted Tumor #1
Tumor
Tumor (prolif)
LNM cell
Serially Transplanted Tumor #2
LNM cell
Tumor
e
Attractor
f
Entropy
g
Dynamical Manifold
h
Transition Probabilities
Black BrafCA/+ PtenΔ/+ Tumor
0
1
2
3
4
LNM cell attractor
Transitional cells
Tumor attractor
Serially Transplanted Tumor #1
Serially Transplanted Tumor #2
23.3
53.8
13.6
55.8
27.8
14.6
69.9
18.7

Figure 2.15. Evidence that LNM cells are transitional cells. A. As described in Fig 10A, tumors derived from Black *Braf*$^{CA/+}$; *Pten*$^{\Delta/+}$ were serially passaged by transplantation into NSG (immune deficient) mice. Tumors from one parental Black *Braf*$^{CA/+}$; *Pten*$^{\Delta/+}$ mouse and two tumors serially transplanted into NSG mice (derived from a single tumor) were subjected to scRNA-seq, analyzed separately, and the neural crest-derived cells were sub-clustered accordingly (parental black *Braf*$^{CA/+}$; *Pten*$^{\Delta/+}$ tumor: 2686 cells; serially transplanted NSG tumor #1 and #2: 10662 and 10965 cells respectively). **B-D.** RNA velocity analysis predicts fate decisions of individual cells in A using (B) Velocity pseudotime, (C) Velocity embedding stream trajectories (note the LNM-to-tumor transition in insets), and (D) Partition-based graph abstraction (PAGA), a topology clustering trajectory method with arrows summarizing directionality from LNM to tumor cells. **E.** Attractors (sTable tates) were identified by applying MuTrans to the same data sets. **F.** Larger entropy values suggest a more transient cell state. **G.** The dynamical manifold constructed by MuTrans, with potential wells representing stable attractors, and individual cells mapped onto the landscape **H.** Transition path analysis calculates predicted relative rates of transition between stable attractor states. Note the transition path from the LNM cell attractor to Tumor attractor. The numbers along paths indicate the proportion of total transition flux, with larger values suggesting higher likelihood of transition.

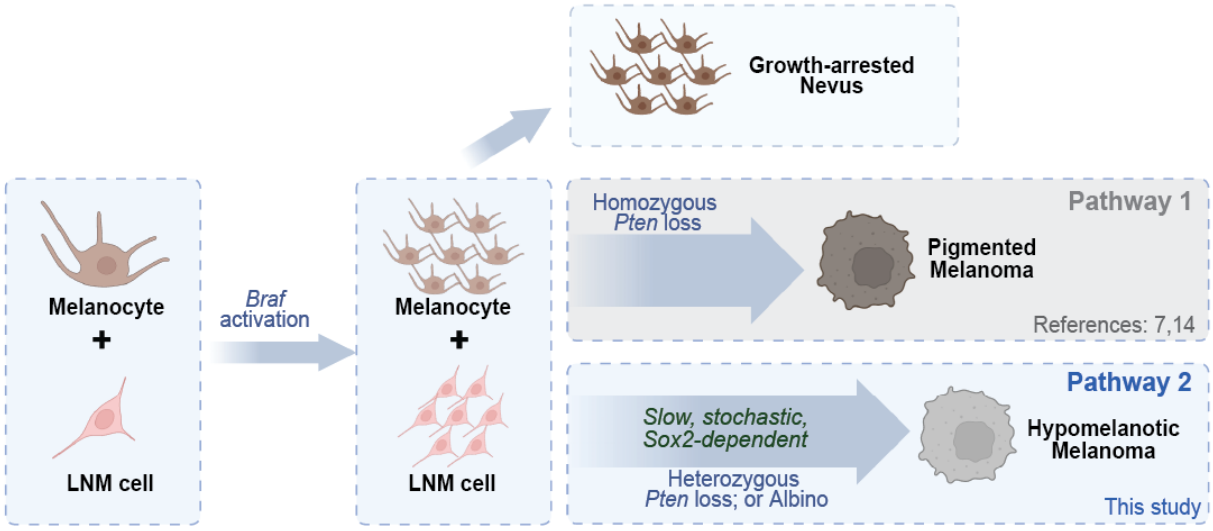
Growth-arrested Nevus
Melanocyte
+
LNM cell
Braf activation
Melanocyte
+
LNM cell
Homozygous Pten loss
Pathway 1
Pigmented Melanoma
References: 7,14
Slow, stochastic, Sox2-dependent
Heterozygous Pten loss; or Albino
Pathway 2
Hypomelanotic Melanoma
This study

Figure 2.16. Proposed pathways to melanomagenesis. Skin contains both pigmented melanocytes and rare, poorly-pigmented LNM cells. Upon *Braf* activation, both populations expand, but melanocytes arrest as nevi, unless loss-of-function mutation in tumor suppressor gene Pten allows them to develop rapidly into pigmented melanomas (Pathway 1). Otherwise, Braf-activated LNM cells can undergo rare, stochastic transitions to produce scantly pigmented melanomas (Pathway 2). The probability of such transitions depends on host pigmentation status, *Sox2* expression, and whether both alleles of *Pten* have become inactivated. LNM cells persist in both types of tumors.

Supplementary Table 1									
rafCA/+ Tumor #1 (estimated tumor fraction: 19%): annotation of all single nucleotide variants, identified by Mutect2, listed									
function	gene	chr	start	end	reference	alternative	coverage	counts	variant freq
intergenic	Tmem38b(dist=53303	chr4	54395049	54395049	A	G	76	46	0.61
intergenic	Capza3(dist=30473),Pl	chr6	140073310	140073310	C	T	23	14	0.61
intergenic	Cntn6(dist=100553),G	chr6	104963958	104963958	-	AA	43	26	0.6
intergenic	Scimp(dist=7320),Rab	chr11	70819881	70819881	T	C	59	34	0.58
ncRNA_intr	Gm38415	chr8	71196903	71196903	C	A	26	15	0.58
intergenic	NONE(dist=NONE),261	chr3	43911240	43911240	C	T	79	45	0.57
intronic	Zfp978	chr4	147140467	147140468	TA	AC	14	8	0.57
intronic	Nek10	chr14	14926515	14926515	T	C	63	35	0.56
intergenic	Platr27(dist=25753),Ct	chr2	157623073	157623073	C	A	9	5	0.56
intergenic	Sox5os3(dist=291304)	chr6	144985136	144985136	C	T	75	42	0.56
intergenic	Gm3985(dist=196851)	chr8	33146877	33146877	A	G	40	21	0.53
intergenic	Srrm4(dist=380239),Su	chr5	116972056	116972056	T	C	41	21	0.51
intergenic	Epha4(dist=156811),P	chr1	77671899	77671899	C	T	80	40	0.5
intergenic	2700089I24Rik(dist=31	chr19	59872595	59872596	AC	GA	8	4	0.5
intergenic	Dnajc1(dist=91080),Co	chr2	18483910	18483910	A	G	6	3	0.5
intronic	Lingo2	chr4	36340635	36340635	A	T	68	34	0.5
intergenic	Gm20756(dist=273434	chr6	26250661	26250661	C	T	10	5	0.5
intergenic	Fbxo8(dist=402509),H	chr8	56996448	56996448	G	A	8	4	0.5
intergenic	Btbd35f14(dist=19613	chrX	33898484	33898484	G	A	6	3	0.5
intronic	Tdrd5	chr1	156292718	156292718	G	A	70	34	0.49
intronic	Tdrd5	chr1	156292721	156292721	C	T	72	35	0.49
intronic	Synpr	chr14	13568769	13568769	C	T	51	25	0.49
ncRNA_intr	Zim3	chr7	6976148	6976148	G	A	53	26	0.49
intronic	Stard9	chr2	120678472	120678472	G	A	48	23	0.48
intergenic	NONE(dist=NONE),261	chr3	44087972	44087972	A	T	60	29	0.48

Supplementary Table 2						
afCA/+ Tumor #1: annotation of all single nucleotide variants located in exons, identified by Mutect2, listed						
function.	location	chr	start	end	ref	alt
nonframeshift deletion	Flna:NM_0102	chrX	74225159	74225167	TCCTGGCAA	-
nonframeshift insertion	Zfp111:NM_01	chr7	24199803	24199803	-	ATC
nonframeshift substituti	Myh8:NM_177	chr11	67297486	67297487	AT	CC
nonframeshift substituti	Ska1:NM_0255	chr18	74199952	74199953	TC	CT
nonsynonymous SNV	Cfhr3:NM_001	chr1	139660883	139660883	A	T
nonsynonymous SNV	Ush2a:NM_021	chr1	188826399	188826399	G	A
nonsynonymous SNV	Cdh23:NM_001	chr10	60379307	60379307	G	A
nonsynonymous SNV	Obscn:NM_199	chr11	59090747	59090747	T	C
nonsynonymous SNV	Krt13:NM_010	chr11	100117606	100117606	C	T
nonsynonymous SNV	Olfr739:NM_14	chr14	50424926	50424926	G	T
nonsynonymous SNV	Olfr742:NM_14	chr14	50515629	50515629	G	A
nonsynonymous SNV	Olfr742:NM_14	chr14	50515645	50515645	T	C
nonsynonymous SNV	Pnp2:NM_0011	chr14	50963153	50963153	C	G
nonsynonymous SNV	Prkdc:NM_011	chr16	15835192	15835192	A	G
nonsynonymous SNV	Pggt1b:NM_17	chr18	46280813	46280813	T	C
nonsynonymous SNV	Mbd2:NM_010	chr18	70568766	70568766	G	T
nonsynonymous SNV	Smc5:NM_153	chr19	23228972	23228972	T	C
nonsynonymous SNV	Smc5:NM_153	chr19	23228991	23228991	C	T
nonsynonymous SNV	G6pc2:NM_021	chr2	69220103	69220103	G	A
nonsynonymous SNV	Cyp7a1:NM_00	chr4	6271203	6271203	C	A
nonsynonymous SNV	Pramel27:NM_	chr4	143852861	143852861	T	G
nonsynonymous SNV	Nupl2:NM_153	chr5	24178021	24178021	G	A
nonsynonymous SNV	Pira6:NM_008	chr7	4281274	4281274	G	C
nonsynonymous SNV	Ptprh:NM_207	chr7	4564181	4564181	C	T
nonsynonymous SNV	Ptgir:NM_0089	chr7	16907397	16907397	G	A

Supplementary Table 3									
function	gene	chr	start	end	reference	alternative	coverage	counts	variant frequ
intronic	Cntn5	chr9	9973088	9973088	T	C	31	31	1.00
intronic	Cntn5	chr9	9973090	9973090	T	C	31	30	0.97
intronic	Rap1gds1	chr3	139069163	139069163	C	T	68	53	0.78
intergenic	Mtss1(dist=20367	chr15	59285699	59285699	-	GG	104	66	0.63
intergenic	2810404M03Rik(d	chr8	42123504	42123504	T	G	67	41	0.61
intergenic	Cd83(dist=238100	chr13	44041233	44041233	G	A	60	34	0.57
intergenic	Nog(dist=74984),A	chr11	89377543	89377543	G	T	76	42	0.55
intergenic	Vmn1r127(dist=18	chr7	21338148	21338148	A	C	11	6	0.55
intergenic	Ces1h(dist=3109),	chr8	93382886	93382886	G	A	103	57	0.55
intergenic	Olfr1087(dist=395	chr2	86730503	86730503	C	T	48	26	0.54
intergenic	Hmgcr(dist=37272	chr13	96708208	96708208	T	A	17	9	0.53
intergenic	Kcng1(dist=18808	chr2	168469618	168469619	TT	GC	60	32	0.53
intergenic	Gm30214(dist=24	chr14	53280178	53280178	T	A	21	11	0.52
intergenic	NONE(dist=NONE	chr14	83648384	83648384	A	T	95	49	0.52
intergenic	Gm41414(dist=42	chr16	5880252	5880252	T	C	75	39	0.52
intronic	Fbxw7	chr3	84842061	84842061	A	G	85	43	0.51
intronic	Rbpms	chr8	33919036	33919036	G	T	37	19	0.51
intergenic	Olfr1510(dist=112	chr14	52422149	52422149	A	G	64	32	0.50
intergenic	Gm30214(dist=24	chr14	53280150	53280150	C	A	18	9	0.50
intergenic	Kirrel(dist=72062)	chr3	87246599	87246599	A	G	34	17	0.50
intergenic	Hao2(dist=8160),(	chr3	98901390	98901390	T	C	18	9	0.50
intergenic	Mtpn(dist=26384	chr6	35803729	35803729	A	G	74	37	0.50
intronic	Kif13a	chr13	46882516	46882516	T	G	47	23	0.49
intronic	Rpgrip1	chr14	52128754	52128754	G	C	69	34	0.49

Supplementary Table 4						
function.	location	chr	start	end	ref	alt
nonframeshift deletion	Psg20:NM_054058:exon1:c.24_26del:p.8_9del,	chr7	18685967	18685969	AGA	-
nonframeshift substitution	Mrgpra3:NM_153067:exon2:c.891_892delinsGC,	chr7	47589285	47589286	TA	GC
nonsynonymous SNV	Nckap5:NM_172484:exon10:c.T4120G:p.C1374G,Nc	chr1	126024694	126024694	A	C
nonsynonymous SNV	Zfp808:NM_001039239:exon4:c.G1631T:p.R544I,	chr13	62172589	62172589	G	T
nonsynonymous SNV	Zfp729a:NM_183146:exon4:c.G1846A:p.V616I,	chr13	67620263	67620263	C	T
nonsynonymous SNV	Gm3752:NM_001374190:exon2:c.T67G:p.S23A,	chr14	3332591	3332591	T	G
nonsynonymous SNV	Olfr1248:NM_146791:exon1:c.A537G:p.I179M,	chr2	89617654	89617654	T	C
nonsynonymous SNV	Olfr1297:NM_146888:exon1:c.G22C:p.V8L,	chr2	111622051	111622051	C	G
nonsynonymous SNV	Rhd:NM_011270:exon4:c.G511C:p.G171R,	chr4	134884041	134884041	G	C
nonsynonymous SNV	Vmn2r129:NM_001384510:exon3:c.A819C:p.E273D,	chr4	156334243	156334243	A	C
nonsynonymous SNV	Gm9758:NM_198666:exon1:c.G110T:p.G37V,	chr5	14914720	14914720	C	A
nonsynonymous SNV	Vmn2r30:NM_009490:exon1:c.A64G:p.N22D,Vmn2r	chr7	7337430	7337430	T	C
nonsynonymous SNV	Vmn2r43:NM_198961:exon6:c.T2033A:p.V678E,	chr7	8245130	8245130	A	T
nonsynonymous SNV	Vmn2r43:NM_198961:exon6:c.C1988A:p.A663D,	chr7	8245175	8245175	G	T
nonsynonymous SNV	Mrgpra6:NM_001308537:exon2:c.G836A:p.S279N,	chr7	47185836	47185836	C	T
nonsynonymous SNV	Mrgpra6:NM_001308537:exon2:c.G800A:p.R267Q,	chr7	47185872	47185872	C	T
nonsynonymous SNV	Ubqln5:NM_027634:exon1:c.G592A:p.A198T,	chr7	104129024	104129024	C	T
nonsynonymous SNV	Gm4884:NM_183166:exon2:c.A83T:p.K28I,	chr7	41040764	41040764	A	T
nonsynonymous SNV	Gm4884:NM_183166:exon2:c.C88T:p.P30S,	chr7	41040769	41040769	C	T
nonsynonymous SNV	Olfr884:NM_001011798:exon1:c.C77T:p.P26L,	chr9	38047300	38047300	C	T
nonsynonymous SNV	Aasdhppt:NM_026276:exon6:c.A863G:p.D288G,Aas	chr9	4296742	4296742	T	C
nonsynonymous SNV	9530077C05Rik:NM_001378983:exon5:c.A790C:p.T2	chr9	22435187	22435187	A	C
nonsynonymous SNV	Flna:NM_001290421:exon21:c.G1577A:p.C526Y,Flna	chrX	74235871	74235871	C	T
synonymous SNV	Obscn:NM_001171512:exon12:c.A3804G:p.G1268G,	chr11	59112667	59112667	T	C
synonymous SNV	Olfr1248:NM_146791:exon1:c.T547C:p.L183L,	chr2	89617644	89617644	A	G
synonymous SNV	AA792892:NM_178894:exon3:c.G741A:p.Q247Q,	chr5	94383999	94383999	G	A
synonymous SNV	Gm5114:NM_177890:exon2:c.C768T:p.P256P,	chr7	39410656	39410656	G	A

Supplementary Table 5

variant_function	gene	chr	start	end	reference	alternative	coverage	counts	variant freq
intergenic	Zc3h12c(dist=	chr9	52316720	52316720	G	C	77	57	0.74
intronic	Rims1	chr1	22790449	22790449	-	AC	51	37	0.73
intergenic	Gm30948(dis	chr12	115388156	115388157	AT	TC	16	11	0.69
intronic	Sgpp2	chr1	78388641	78388641	A	G	54	36	0.67
intergenic	Mir7094-2(di	chr12	114680884	114680884	C	T	6	4	0.67
intergenic	Gm32209(dis	chr4	70756562	70756562	T	C	12	8	0.67
ncRNA_intronic	Gm30948	chr12	115279389	115279389	A	G	8	5	0.63
intergenic	Gm20755(dis	chr3	38197704	38197704	T	A	54	33	0.61
intergenic	Gm3752(dist=	chr14	4322345	4322346	AT	TG	5	3	0.60
intronic	Skint5	chr4	113597149	113597149	A	G	65	39	0.60
intergenic	Usp17ld(dist=	chr7	103292313	103292313	G	A	10	6	0.60
intergenic	Mir6343(dist=	chr1	77226332	77226332	T	G	34	20	0.59
intergenic	D830030K20I	chr14	3245203	3245203	G	A	17	10	0.59
ncRNA_intronic	Gm30948	chr12	115279387	115279387	T	A	7	4	0.57
intergenic	Vmn2r45(dist	chr7	8603755	8603755	C	A	14	8	0.57
intergenic	Gm20482(dis	chr7	9895869	9895869	G	T	7	4	0.57
intronic	Lrrfip1	chr1	91095171	91095171	T	C	79	44	0.56
intergenic	Enpp3(dist=1	chr10	24850214	24850214	A	G	41	23	0.56
intergenic	Mir7094-2(di	chr12	115141885	115141885	A	G	31	17	0.55
intergenic	Gm30948(dis	chr12	115388146	115388146	T	C	20	11	0.55
intergenic	Pkia(dist=341	chr3	7479552	7479552	T	A	11	6	0.55
intronic	St3gal3	chr4	118007447	118007447	C	A	40	22	0.55
intergenic	Zfp600(dist=4	chr4	146241040	146241040	T	C	11	6	0.55
intronic	Vmn2r36	chr7	7878099	7878099	T	A	20	11	0.55
intergenic	Prss32(dist=5	chr17	23865036	23865036	G	A	68	37	0.54
intergenic	Zfp869(dist=1	chr8	69735012	69735012	A	G	46	25	0.54

Supplementary Table 6						
function.	location	chr	start	end	ref	alt
frameshift insertion	Asah2:NM_018830:exon23:c.2	chr19	31992009	31992009	-	ATACTTTCTAAAATA
nonframeshift deletion	Chd9:NM_177224:exon32:c.64	chr8	91034067	91034069	TCT	-
nonframeshift substitution	Dcpp3:NM_001077633:exon3:	chr17	23918001	23918002	CA	TG
nonframeshift substitution	Olfr1033:NM_146578:exon3:c.	chr2	86042056	86042057	GC	TA
nonsynonymous SNV	Eef2:NM_007907:exon3:c.T37	chr10	81178211	81178211	T	C
nonsynonymous SNV	Rps6kb1:NM_001363162:exon	chr11	86504284	86504284	C	T
nonsynonymous SNV	Gm19428:NM_001384228:exo	chr13	65549595	65549595	G	A
nonsynonymous SNV	Gm3739:NM_001378725:exon	chr14	7299386	7299386	C	T
nonsynonymous SNV	Spopfm2:NM_001146107:exor	chr3	94175943	94175943	C	A
nonsynonymous SNV	Rex2:NM_001177767:exon5:c.	chr4	147058963	147058963	T	G
nonsynonymous SNV	Rex2:NM_001177767:exon5:c.	chr4	147058981	147058981	T	C
nonsynonymous SNV	Speer4e:NM_001122661:exon	chr5	14938276	14938276	C	T
nonsynonymous SNV	Gm21663:NM_001378637:exo	chr5	25938769	25938769	C	T
nonsynonymous SNV	Pira6:NM_008848:exon8:c.A15	chr7	4282375	4282375	A	C
nonsynonymous SNV	Gm5592:NM_001033782:exon	chr7	41289432	41289432	G	A
nonsynonymous SNV	Trpm1:NM_001039104:exon27	chr7	64268702	64268702	A	G
synonymous SNV	Dnah7c:NM_001310335:exon5	chr1	46777798	46777798	T	C
synonymous SNV	Serpina1f:NM_001164742:exo	chr12	103691796	103691796	T	C
synonymous SNV	Gm19428:NM_001384228:exo	chr13	65549590	65549590	G	A
synonymous SNV	Nr1d2:NM_011584:exon5:c.T1	chr14	18215006	18215006	A	G
synonymous SNV	Nr1d2:NM_011584:exon5:c.T1	chr14	18215009	18215009	A	G
synonymous SNV	Btnl6:NM_030747:exon9:c.T12	chr17	34508343	34508343	A	C
synonymous SNV	Gm5114:NM_177890:exon2:c.	chr7	39411232	39411232	A	G
synonymous SNV	Siah1a:NM_009172:exon2:c.T4	chr8	86725369	86725369	A	G
unknown	UNKNOWN	chr4	156335640	156335641	AC	GT

Supplementary Table 7					
Tumor 1		**Tumor 2**		**Tumor 3**	
nonframeshift deletion	Flna	nonframeshift deletion	Psg20	frameshift insertion	Asah2
nonframeshift insertion	Zfp111	nonframeshift substitution	Mrgpra3	nonframeshift deletion	Chd9
nonframeshift substitution	Myh8	nonsynonymous SNV	Nckap5	nonframeshift substitution	Dcpp3
nonframeshift substitution	Ska1	nonsynonymous SNV	Zfp808	nonframeshift substitution	Olfr1033
nonsynonymous SNV	Cfhr3	nonsynonymous SNV	Zfp729a	nonsynonymous SNV	Eef2
nonsynonymous SNV	Ush2a	nonsynonymous SNV	Gm3752	nonsynonymous SNV	Rps6kb1
nonsynonymous SNV	Cdh23	nonsynonymous SNV	Olfr1248	nonsynonymous SNV	Gm19428
nonsynonymous SNV	Obscn	nonsynonymous SNV	Olfr1297	nonsynonymous SNV	Gm3739
nonsynonymous SNV	Krt13	nonsynonymous SNV	Rhd	nonsynonymous SNV	Spopfm2
nonsynonymous SNV	Olfr739	nonsynonymous SNV	Vmn2r129	nonsynonymous SNV	Rex2
nonsynonymous SNV	Olfr742	nonsynonymous SNV	Gm9758	nonsynonymous SNV	Speer4e
nonsynonymous SNV	Pnp2	nonsynonymous SNV	Vmn2r30	nonsynonymous SNV	Gm21663
nonsynonymous SNV	Prkdc	nonsynonymous SNV	Vmn2r43	nonsynonymous SNV	Pira6
nonsynonymous SNV	Pggt1b	nonsynonymous SNV	Mrgpra6	nonsynonymous SNV	Gm5592
nonsynonymous SNV	Mbd2	nonsynonymous SNV	Ubqln5	nonsynonymous SNV	Trpm1
nonsynonymous SNV	Smc5	nonsynonymous SNV	Gm4884		
nonsynonymous SNV	G6pc2	nonsynonymous SNV	Olfr884		
nonsynonymous SNV	Cyp7a1	nonsynonymous SNV	Aasdhppt		
nonsynonymous SNV	Pramel27	nonsynonymous SNV	9530077C05Rik		
nonsynonymous SNV	Nupl2	nonsynonymous SNV (exon21)	Flna		
nonsynonymous SNV	Pira6				
nonsynonymous SNV	Ptprh				
nonsynonymous SNV	Ptgir				
nonsynonymous SNV	Scgb2b7				

Supplementary Table 8

Yellow cells denote mutations supported by 1 read, likely to be sequencing error. Green cells denote mutations supported by m

Animal ID	Sample	Genotype	Coat Colo	mor/skin ty	Gender	location	ral rea	total c	ref	mut	seq (b	codon	amino acid (b
Exon 21													
Skin with No Braf mutation (n=7)													
alt 850	S80	*Pten* $^{\Delta/+}$; *Cre* +; *m*	albino	Control skin	F	74236180	315	5	G (4)	C (1)	CGT	GCA	Alanine (A)
alt 852	S85	*Cre* +; *mTmG* +	albino	Control skin	M	74236088	285	4	C (3)	A (1)	CTC	GAG	Glutamic acid
						74236104		5	G (4)	T (1)	GGG	CCC	proline (P)
						74236189		2	C (1)	A (1)	CCC	GGG	Glycine (G)
						74236206		2	A (1)	G (1)	AAA	UUU	Phenylalanine
alt 856	S105	*Cre* +; *mTmG* +	albino	Control skin	M	74235853	146	2	G (1)	T(1)	CGA	GCU	Alanine (A)
						74235890		2	C (1)	A (1)	CCC	GGG	Glycine (G)
alt 857	S79	*Pten* $^{\Delta/+}$; *Cre* +; *m*	albino	Control skin	F	no mutations	325						
alt 856	S86	*Cre* +; *mTmG* +	albino	Control skin	M	no mutations	207						
alf 162	S108	*Cre+; mTmG-*	albino	Control skin	M	no mutations	149						
alf 161	S109	*Cre* +; *mTmG-*	albino	Control skin	F	no mutations	177						
Tumor matched-skin (n=7)													
alt 768	S103	*Braf* $^{CA/+}$; *Cre* +; *n*	albino	nor-adjacent	F	no mutations	174						
						no mutations							
alf 160	S106	*Braf* $^{CA/+}$; *Cre* +; *n*	albino	nor-adjacent	M	no mutations	140						
alf 165	S110	*Braf* $^{CA/+}$; *Cre* +; *n*	albino	nor-adjacent	F	no mutations	231						

Supplementary Table 9									
Chr1	Pos1	Orientation1	Chr2	Pos2	Orientation2	Type	Size	Score	num_Reads
chr1	5261032	11+10-	chr1	5262105	11+10-	ITX	-326	42	3
chr1	10729605	11+1-	chr1	10736987	1+22-	DEL	7332	33	2
chr1	24076120	5+3-	chr1	24076396	5+3-	ITX	-351	47	2
chr1	27336440	34+34-	chr1	27339031	34+34-	INV	213	32	3
chr1	42735381	56+55-	chr1	42740235	56+55-	INV	806	31	4
chr1	58370429	34+30-	chr1	58373287	34+30-	INV	242	32	3
chr1	63267497	9+9-	chr1	63268271	9+9-	ITX	-322	33	2
chr1	73332027	13+14-	chr1	73332882	13+14-	INV	-413	36	2
chr1	78383354	59+50-	chr1	78388234	59+50-	INV	964	31	4
chr1	85081508	14+8-	chr1	85499625	4+2-	INV	4E+05	39	2
chr1	85273741	90+60-	chr1	85274562	90+60-	ITX	-313	31	2
chr1	86476498	33+39-	chr1	86479117	33+39-	INV	344	34	3
chr1	91214301	29+25-	chr1	91215150	29+25-	ITX	-364	32	2
chr1	93112311	15+15-	chr1	93113632	15+15-	INV	-347	31	2
chr1	109315584	21+16-	chr1	109316778	21+16-	INV	-7	31	2
chr1	109521920	27+45-	chr1	109524634	27+45-	INV	407	31	3
chr1	111581393	12+8-	chr1	111581986	12+8-	ITX	-310	35	2
chr1	117821514	8+3-	chr1	117822224	3+4-	INV	822	31	2
chr1	118038831	6+7-	chr1	118039860	0+3-	INV	628	34	2
chr1	122689310	6+15-	chr1	122689863	6+15-	ITX	-313	38	2
chr1	125362250	2+2-	chr1	125362259	2+2-	ITX	-314	90	2
chr1	128225272	14+16-	chr1	128226233	14+16-	INV	496	34	2
chr1	136692334	3+7-	chr1	136694431	22+15-	INV	683	33	3
chr1	137038841	11+21-	chr1	137039975	11+21-	INV	71	33	2

Supplementary Table 10									
Chr1	Pos1	Orientation1	Chr2	Pos2	Orientation2	Type	Size	Score	num_Reads
chr1	3488216	22+16-	chr1	3489612	22+16-	INV	796	35	2
chr1	8491982	4+3-	chr1	8492218	6+5-	DEL	524	37	3
chr1	8741486	6+5-	chr1	8752461	2+16-	INV	10339	46	2
chr1	18114283	20+53-	chr1	18115219	20+53-	ITX	-350	93	6
chr1	26169666	5+4-	chr1	26170258	1+3-	DEL	472	35	2
chr1	27898707	2+2-	chr1	27899211	0+6-	DEL	505	40	2
chr1	32354462	10+6-	chr1	32355018	10+6-	INV	-109	48	2
chr1	38627092	6+4-	chr1	38627499	6+4-	ITX	-343	43	2
chr1	38824019	13+51-	chr1	60538772	7+2-	ITX	21713460	47	4
chr1	38990139	24+12-	chr1	38990415	3+16-	DEL	571	60	6
chr1	39344192	4+1-	chr1	39344651	1+5-	DEL	474	36	2
chr1	42434651	2+5-	chr1	87828402	10+13-	INV	45393232	33	2
chr1	42632116	14+15-	chr1	42633082	14+15-	ITX	-365	33	2
chr1	50022475	10+7-	chr1	50023198	10+7-	ITX	-305	35	2
chr1	51200393	6+7-	chr1	51201047	6+7-	ITX	-323	37	2
chr1	54814147	4+1-	chr1	54814419	2+6-	DEL	508	31	2
chr1	55607397	13+9-	chr1	55608422	13+9-	ITX	-308	33	2
chr1	59737748	9+12-	chr1	59738492	9+12-	INV	-180	44	2
chr1	60457586	3+0-	chr1	60457952	1+8-	DEL	456	34	2
chr1	62132196	14+12-	chr1	62133895	14+12-	INV	391	35	2
chr1	62779966	1+9-	chr1	141885393	15+11-	INV	79103760	31	2
chr1	66539828	2+0-	chr1	66540184	3+5-	DEL	505	31	2
chr1	67421731	6+2-	chr1	67422052	1+3-	DEL	475	31	2
chr1	69099581	3+8-	chr1	69100432	3+8-	ITX	-310	33	2

Supplementary Table 11

Albino BrafCA/+ Tumor #1:Copy number variants, listed in Fig 1E, identified by the CNVkit pipeline

cn: the absolute copy number for each segmented region
log2: log2-transformed copy number ratio for each segmented region
depth: the average sequencing depth (read coverage) across all bins or probes within that segment region
weight: sums the bin-level weights for each regment region
Bolded rows denote intervals containing genes with potential CNVs shared across the CNVkit analysis of all three tumors, as well as with a

chrom	start	end	gene	log2	ci_hi	ci_lo	cn	depth	probes	weight	p_ttest
chr1	5975184	6153465	-	-0.842847	-0.119765	-0.130352	1	65.2324	273	264.754	1.34874e-35
chr1	10145298	10225173	Arfgef1	0.418165	0.0942814	0.0841765	3	85.0318	123	122.178	6.7031e-22
chr1	10335081	10448823	Cpa6	-0.580749	-0.0885079	-0.0983628	1	68.1984	175	173.697	3.60845e-25
chr1	12154953	12284670	-	-0.530229	-0.0808676	-0.0904129	1	69.8574	201	198.677	2.40518e-22
chr1	14928213	15004893	-	-0.519615	-0.0798195	-0.0919263	1	68.9047	120	118.884	5.45801e-16
chr1	15460500	15544209	Kcnb2	-0.586127	-0.0888686	-0.101347	1	67.1119	130	128.718	1.27085e-20
chr1	20560998	20729694	Pkhd1,Mir20(	-0.502663	-0.0771191	-0.0867043	1	67.3124	264	261.07	3.92577e-27
chr1	22048590	22174473	-	-0.509993	-0.0768334	-0.0877593	1	69.3784	194	191.704	3.10599e-22
chr1	22392372	22502932	Rims1	0.489395	0.115849	0.100813	3	85.4919	108	107.305	1.47449e-21
chr1	23989246	24069760	1110058L19R	0.381754	0.086884	0.0773175	3	82.577	121	120.155	1.83829e-15
chr1	25756081	25828927	Bai3	0.469826	0.107957	0.094388	3	84.8499	105	104.281	5.14718e-19
chr1	27547836	27690333	-	0.337623	0.0769585	0.0653456	3	81.1765	183	181.744	1.15563e-16
chr1	28802832	29029038	-	0.397471	0.0889843	0.0801244	3	82.2627	287	284.682	6.33054e-37
chr1	30644429	30776702	-	-0.64514	-0.0979118	-0.10894	1	66.8735	207	204.553	6.57073e-29
chr1	35038831	35158963	-	-0.527268	-0.07951	-0.0914741	1	67.5365	187	185.27	1.98553e-20
chr1	45338869	45515872	Col3a1,Col5a	0.349536	0.0780047	0.0693331	3	81.7076	259	256.959	6.55604e-27
chr1	46423891	46501849	-	-0.832307	-0.118773	-0.130791	1	63.5209	122	120.394	1.63587e-23
chr1	46940842	47030301	-	-0.489352	-0.0750307	-0.0875666	1	70.0171	140	138.693	5.62385e-16

Supplementary Table 12									
Albino BrafCA/+ Tumor #2: Structural variants in tumor, listed in Fig 1E, identified by the BreakDancer pipeline,									
Chr1	Pos1	Orientatio	Chr2	Pos2	Orientation2	Type	Size	Score	num_Reads
chr1	5110163	3+2-	chr1	5110261	3+2-	ITX	-318	66	2
chr1	13502798	2+2-	chr1	100908280	15+8-	INV	87404968	46	2
chr1	15743508	6+4-	chr1	15743920	6+4-	ITX	-363	46	2
chr1	22301523	32+28-	chr1	22303551	32+28-	DEL	527	33	4
chr1	37583833	14+7-	chr1	37585332	21+17-	INV	1105	37	2
chr1	44015980	18+24-	chr1	44018177	18+24-	INS	-398	86	2
chr1	44375566	4+6-	chr1	44375617	4+6-	ITX	-345	74	2
chr1	45991173	13+14-	chr1	45994118	2+5-	INV	4519	33	2
chr1	50462014	22+17-	chr1	50464202	22+17-	INV	-197	32	2
chr1	54882123	13+16-	chr1	54883430	13+16-	ITX	-332	31	2
chr1	58474997	17+11-	chr1	58476588	17+11-	INV	356	36	2
chr1	62196355	10+12-	chr1	62197774	18+13-	INV	614	32	2
chr1	62492358	20+33-	chr1	62494829	20+33-	INV	-126	31	2
chr1	63309392	6+6-	chr1	63309951	6+6-	ITX	-351	42	2
chr1	65499319	18+9-	chr1	182977064	170+10-	INV	117477408	34	2
chr1	72653566	30+20-	chr1	72655798	30+20-	INS	-396	91	2
chr1	72653620	35+19-	chr1	72654979	35+19-	INS	-398	99	4
chr1	75312095	7+13-	chr1	75313299	7+13-	DEL	561	33	3
chr1	75643403	81+15-	chr1	156205820	12+11-	INV	80562360	31	2
chr1	77114560	21+14-	chr1	77116027	14+10-	INV	1479	56	4
chr1	80665152	11+12-	chr1	80666053	11+12-	INS	-396	99	2
chr1	85091293	241+68-	chr1	85620445	4+3-	INV	528735	43	2
chr1	85250554	48+52-	chr1	85251688	48+52-	DEL	480	34	3

Supplementary Table 13

Albino BrafCA/+ Skin #2: Structural variants in skin, identified by the BreakDancer pipeline, with spleen as control (skin - spleen)

Chr1	Pos1	Orientation1	Chr2	Pos2	Orientation2	Type	Size	Score	num_Read
chr1	6819986	4+0-	chr1	6820259	9+15-	DEL	543	32	3
chr1	7324977	3+0-	chr1	7325663	1+4-	DEL	579	44	2
chr1	11475103	3+8-	chr1	11475912	3+8-	ITX	-311	35	2
chr1	18813465	3+6-	chr1	60189639	2+1-	ITX	41375568	37	2
chr1	28587978	5+4-	chr1	28587991	5+4-	ITX	-386	99	4
chr1	28940356	2+0-	chr1	28940818	2+5-	DEL	578	35	2
chr1	29392172	12+4-	chr1	29392346	2+3-	DEL	514	40	3
chr1	30514248	7+6-	chr1	30514876	7+6-	ITX	-352	38	2
chr1	32049670	31+6-	chr1	32050377	2+2-	INV	761	41	2
chr1	36726640	11+12-	chr1	36727243	11+12-	ITX	-325	39	2
chr1	42765687	4+1-	chr1	42766246	1+6-	DEL	569	31	2
chr1	49702462	2+3-	chr1	49702924	5+6-	DEL	553	32	2
chr1	57062386	6+1-	chr1	57062832	0+3-	DEL	510	34	2
chr1	58421927	6+2-	chr1	58422123	2+3-	DEL	588	31	2
chr1	66685292	3+1-	chr1	66685691	4+6-	DEL	560	34	2
chr1	69021304	7+6-	chr1	69021510	3+8-	DEL	570	32	3
chr1	69984508	17+11-	chr1	69985494	17+11-	ITX	-350	46	3
chr1	74570421	11+5-	chr1	74570653	6+6-	DEL	547	31	3
chr1	82923684	8+2-	chr1	82923881	40+6-	DEL	551	32	3
chr1	85075795	13+14-	chr1	85635101	12+2-	INV	559437	49	2
chr1	85209258	3+0-	chr1	85307337	2+1-	INV	97659	83	2
chr1	85274568	40+25-	chr1	85597208	4+1-	INV	322695	44	2
chr1	85479453	3+3-	chr1	85479544	3+3-	ITX	-330	63	2

Supplementary Table 14

Albino BrafCA/+ Tumor #2:Copy number variants, listed in Fig 1E, identified by the CNVkit pipeline

cn: the absolute copy number for each segmented region
log2: log2-transformed copy number ratio for each segmented region
depth: the average sequencing depth (read coverage) across all bins or probes within that segment region
weight: sums the bin-level weights for each regment region
Bolded rows denote intervals containing genes with potential CNVs shared across the CNVkit analysis of all three tumors, as well as with a

chromos	start	end	gene	log2	ci_hi	ci_lo	cn	depth	probes	weight	p_ttest
chr1	30669989	30758171	-	-0.480518	-0.23886	-0.25251	1	67.1309	138	136.269	2.66057e-50
chr1	66356212	66439921	Map2	0.33729	0.200273	0.189905	3	100.463	129	127.865	5.75223e-49
chr1	89647252	89732878	Agap1,Agap1	0.462096	0.277502	0.268057	3	101.537	134	132.917	3.85094e-73
chr1	91897173	92060118	Hdac4	0.338873	0.200629	0.192172	3	96.996	255	252.989	2.17796e-93
chr1	97195765	97271167	-	-0.430843	-0.21276	-0.22822	1	69.1739	114	113.113	1.2549e-42
chr1	117800334	117976059	-	-0.593078	-0.29091	-0.30045	1	65.5505	271	268.563	6.65173e-126
chr10	4226507	4307017	Akap12	-0.555975	-0.27154	-0.28567	1	61.0923	126	124.154	1.03691e-58
chr10	62862258	62953635	Tet1,Slc25a1	-0.474304	-0.23517	-0.24802	1	63.165	142	140.232	1.41834e-60
chr10	75653763	75725331	Cabin1	0.345726	0.20625	0.193222	3	96.7218	112	111.129	5.7357e-48
chr10	78612972	78713295	Olfr1357,Cas	-0.536949	-0.26407	-0.27484	1	64.7417	157	155.463	7.56292e-66
chr10	128148261	128221107	Rbms2,Gls2,G	-0.422785	-0.20897	-0.22298	1	66.1102	113	111.855	1.02008e-39
chr11	7157002	7226653	Adcy1,Gm119	0.325165	0.1939	0.182434	3	95.3164	107	106.295	2.88353e-40
chr11	11943101	12062594	Grb10	0.355881	0.212178	0.201956	3	100.495	185	183.408	1.13607e-75
chr11	16751566	16929208	Egfr	0.329096	0.192579	0.186229	3	98.8251	276	273.735	5.40725e-101
chr11	57855621	58006425	-	-0.446639	-0.22399	-0.23205	1	64.2831	236	233.257	2.89626e-94
chr11	77617998	77698512	Nufip2	-0.612139	-0.29752	-0.3126	1	60.2236	125	123.427	9.41549e-64
chr11	107428022	107565407	Pitpnc1,Psmc	-0.494649	-0.24581	-0.25706	1	62.9087	215	212.225	1.74057e-79
chr12	29735562	29839718	Myt1l	0.387263	0.231256	0.221835	3	99.3077	163	161.93	6.93743e-78

Supplementary Table 15									
Albino BrafCA/+ Tumor #3: Structural variants in tumor, listed in Fig 1E, identified by the BreakDancer pipeline,									
Chr1	Pos1	Orientation1	Chr2	Pos2	Orientation2	Type	Size	Score	num_Reads
chr1	4766634	15+24-	chr1	4768113	15+24-	INV	33	38	2
chr1	5757190	10+9-	chr1	5758438	9+8-	INV	937	34	2
chr1	15784837	26+12-	chr1	15785818	26+12-	ITX	-339	59	4
chr1	16924195	9+8-	chr1	16925564	7+7-	INV	1466	38	2
chr1	21194610	2+3-	chr1	21284662	4+4-	INV	89265	56	2
chr1	21203953	6+10-	chr1	21281500	1+3-	INV	77185	53	2
chr1	29839751	10+4-	chr1	29840520	10+4-	ITX	-287	34	2
chr1	31306720	6+9-	chr1	31310909	16+13-	INV	4533	33	2
chr1	32095397	20+14-	chr1	32096921	20+14-	INV	-381	38	2
chr1	35048835	4+9-	chr1	35049240	4+9-	ITX	-312	42	2
chr1	41207428	8+11-	chr1	41208213	8+11-	ITX	-284	33	2
chr1	43448605	3+7-	chr1	43449107	3+7-	ITX	-284	39	2
chr1	46192822	22+27-	chr1	46581229	14+105-	INV	4E+05	35	2
chr1	46210972	1+7-	chr1	53539133	10+7-	INV	7E+06	47	2
chr1	46229022	7+3-	chr1	46661549	16+8-	DEL	4E+05	31	2
chr1	53040366	7+9-	chr1	53041281	7+9-	ITX	-283	31	2
chr1	55933385	37+31-	chr1	55936321	37+31-	INV	-325	31	2
chr1	55962677	18+71-	chr1	55964415	18+71-	INV	-346	36	2
chr1	59475324	10+5-	chr1	59475894	10+5-	ITX	-284	38	2
chr1	60510628	23+36-	chr1	60513544	23+36-	INV	-163	31	2
chr1	67340556	9+11-	chr1	67341226	9+11-	ITX	-283	35	2
chr1	67586648	78+9-	chr1	67587363	78+9-	ITX	-282	34	2
chr1	68373405	30+30-	chr1	68374932	30+30-	INV	-311	38	2
chr1	78022106	32+29-	chr1	78024803	32+29-	INV	-213	31	2
chr1	78800729	10+6-	chr1	78801178	10+6-	ITX	-284	41	2

Supplementary Table 16									
Albino BrafCA/+ Skin #3: Structural variants in skin, identified by the BreakDancer pipeline, with spleen as control (skin - spleen)									
Chr1	Pos1	Orientation1	Chr2	Pos2	Orientation2	Type	Size	Score	num_Re
chr1	7392728	35+28-	chr1	7393660	35+28-	ITX	-393	35	2
chr1	13821502	4+108-	chr1	15731205	10+15-	INV	1908179	32	2
chr1	16326761	13+10-	chr1	16327665	13+10-	INV	-126	42	2
chr1	16601818	12+6-	chr1	16602740	12+6-	INV	226	42	2
chr1	21213525	5+2-	chr1	21276252	5+1-	INV	62292	99	4
chr1	25840845	7+7-	chr1	25841131	9+10-	DEL	593	42	5
chr1	26520275	3+6-	chr1	26520673	3+6-	ITX	-330	44	2
chr1	28009201	10+27-	chr1	174447593	77+67-	INV	146438560	42	4
chr1	28587989	3+8-	chr1	28588592	3+8-	ITX	-409	40	2
chr1	28854587	24+6-	chr1	28855629	24+6-	ITX	-352	33	2
chr1	31019550	2+3-	chr1	31020079	2+3-	DEL	547	34	2
chr1	38652934	4+5-	chr1	38653387	4+5-	ITX	-356	42	2
chr1	44728532	6+0-	chr1	44729958	4+78-	DEL	1322	49	3
chr1	45026341	72+55-	chr1	45028112	72+55-	INV	-238	35	2
chr1	46090019	20+24-	chr1	53680361	7+4-	INV	7591500	52	3
chr1	46400724	5+4-	chr1	53733262	4+0-	INV	7332138	49	2
chr1	46429067	3+0-	chr1	53705197	23+6-	INV	7274261	37	2
chr1	47532892	18+20-	chr1	47534759	18+20-	INV	-171	34	2
chr1	47816812	8+16-	chr1	99355400	4+28-	INV	51537880	43	2
chr1	48656399	5+8-	chr1	50007637	9+9-	INV	1350628	65	3
chr1	48658261	7+61-	chr1	50007790	10+6-	INV	1350078	63	4
chr1	50672301	16+7-	chr1	50674581	16+7-	INV	-183	32	2
chr1	66242232	64+20-	chr1	66243160	27+56-	DEL	880	36	5

Supplementary Table 17

Albino BrafCA/+ Tumor #3:Copy number variants, listed in Fig 1E, identified by the CNVkit pipeline

cn: the absolute copy number for each segmented region
log2: log2-transformed copy number ratio for each segmented region
depth: the average sequencing depth (read coverage) across all bins or probes within that segment region
weight: sums the bin-level weights for each regment region
Bolded rows denote intervals containing genes with potential CNVs shared across the CNVkit analysis of all three tumors, as well

chromo	start	end	gene	log2	ci_hi	ci_lo	cn	depth	probes	weight
chr10	4220117	4310851	Akap12	-0.538135	-0.16435	-0.178405	1	54.8754	142	139.935
chr10	6176009	6280162	-	-0.423306	-0.132278	-0.145612	1	62.7764	160	158.258
chr10	6596453	6671212	-	-0.463692	-0.143608	-0.156837	1	72.3983	116	114.552
chr10	22148487	22242420	E030030I06	0.592005	0.266061	0.231579	3	88.678	147	143.871
chr10	52555916	52649849	-	-0.450463	-0.13819	-0.153586	1	61.3709	144	142.503
chr10	59885157	59977173	Dnajb12,Dc	-0.555693	-0.172603	-0.181492	1	56.6586	144	142.359
chr10	62492277	62589405	Srgn,25100	-0.518363	-0.160416	-0.170794	1	59.4659	152	150.791
chr10	62854590	62947884	Tet1,Slc25a	-0.486008	-0.150438	-0.16355	1	56.2854	145	143.233
chr10	69357056	69428624	-	-0.521372	-0.157843	-0.178417	1	54.7263	112	110.249
chr10	78027648	78115830	Aire,Aire,D	-0.442926	-0.138803	-0.150256	1	58.3459	138	136.8
chr10	78590607	78711378	Syde1,Olfr1	-0.512142	-0.158286	-0.169179	1	58.9118	189	187.236
chr10	81734488	81829699	Zfp781,Gm	-1.94862	-0.435627	-0.457845	1	54.0402	149	144.077
chr10	81888487	81967723	Zfp781	-0.751268	-0.220408	-0.236033	1	62.6567	124	120.917
chr10	82516624	82624615	1190007I07	-0.821013	-0.22995	-0.260419	1	61.9062	165	162.563
chr10	106787126	106924511	Ppfia2	0.328947	0.129271	0.120508	3	82.1248	184	182.254
chr10	117370885	117456511	Cpsf6	-0.484728	-0.148928	-0.162728	1	57.3835	134	132.489
chr10	127091355	127168035	Agap2,Os9,	-0.439178	-0.135531	-0.148276	1	60.1982	120	119.131

Supplementary Table 18								
Metadata for all samples subjected to scRNA-seq, that were described in Fig 2A and Fig3A								
ALBINO SAMPLES (n=29)								
Sample	**Coat Col**	**Tissue s**	**Sample location**	**Tumor/skin type**	**Gender**	**Animal ID**	**Genotype**	**Age**
S71	albino	skin	depilated back	tumor-adjacent skin	M	alt 839	*Braf* $^{CA/+}$; *Pten* $^{\Delta/+}$; *Cre* +; *mTmG* +	P72
S72	albino	tumor	depilated back	Spontaneous tumor	M	alt 839	*Braf* $^{CA/+}$; *Pten* $^{\Delta/+}$; *Cre* +; *mTmG* +	P72
S73	albino	skin	depilated back	Tumor-adjacent skin	M	alt 835	*Braf* $^{CA/+}$; *Pten* $^{\Delta/+}$; *Cre* +; *mTmG* +	P72
S74	albino	tumor	depilated back	Spontaneous tumor	M	alt 835	*Braf* $^{CA/+}$; *Pten* $^{\Delta/+}$; *Cre* +; *mTmG* +	P72
S75	albino	skin	depilated back	Tumor-adjacent skin	F	alt 858	*Braf* $^{CA/+}$; *Pten* $^{\Delta/+}$; *Cre* +; *mTmG* +	P56
S76	albino	tumor	depilated back	Spontaneous tumor	F	alt 858	*Braf* $^{CA/+}$; *Pten* $^{\Delta/+}$; *Cre* +; *mTmG* +	P56
S77	albino	skin	depilated back	Tumor-adjacent skin	M	alt 819	*Braf* $^{CA/+}$; *Pten* $^{\Delta/+}$; *Cre* +; *mTmG* +	P76
S78	albino	tumor	depilated back	Spontaneous tumor	M	alt 819	*Braf* $^{CA/+}$; *Pten* $^{\Delta/+}$; *Cre* +; *mTmG* +	P76
S79	albino	skin	depilated back	Control skin	F	alt 857	*Pten* $^{\Delta/+}$; *Cre* +; *mTmG* +	P56
S80	albino	skin	depilated back	Control skin	F	alt 850	*Pten* $^{\Delta/+}$; *Cre* +; *mTmG* +	P56
S81	albino	skin	depilated back	Nevus skin	M	alt 855	*Braf* $^{CA/+}$; *Cre* +; *mTmG* +	P56
S82	albino	skin	depilated back	Nevus skin	F	alt 854	*Braf* $^{CA/+}$; *Cre* +; *mTmG* +	P56
S83	albino	skin	depilated back	Nevus skin	M	alt 818	*Braf* $^{CA/+}$; *Cre* +; *mTmG* +	P76
S84	albino	skin	depilated back	Nevus skin	M	alt 820	*Braf* $^{CA/+}$; *Cre* +; *mTmG* +	P76
S85	albino	skin	depilated back	Control skin	M	alt 852	*Cre* +; *mTmG* +	P56
S86	albino	skin	depilated back	Control skin	M	alt 856	*Cre* +; *mTmG* +	P56
S103	albino	skin	depilated back	Tumor-adjacent skin	F	alt 768	*Braf* $^{CA/+}$; *Cre* +; *mTmG-*	P282
S104	albino	tumor	depilated back	Spontaneous tumor	F	alt 768	*Braf* $^{CA/+}$; *Cre* +; *mTmG-*	P282
S105	albino	skin	depilated back	Control skin	M	alt 856	*Cre* +; *mTmG* +	P282
S106	albino	skin	depilated back	Tumor-adjacent skin	M	alf 160	*Braf* $^{CA/+}$; *Cre* +; *mTmG* +; *Fucci* +	P164

Supplementary Table 19							
Top 30 differentially expressed genes for each cell type that are depicted in the UMAP plot in Fig 2B							
	p_val	avg_log2FC	pct.1	pct.2	p_val_adj	cluster	gene
1	0	3.42078455	0.963	0.33	0	Basal	Krt14
2	0	3.30321008	0.93	0.28	0	Basal	Krt15
3	0	2.80058527	0.986	0.334	0	Basal	Krt5
4	0	2.36526574	0.749	0.148	0	Basal	Ccl27a
5	0	2.06550422	0.99	0.552	0	Basal	Sfn
6	0	1.76013173	0.732	0.112	0	Basal	Col17a1
7	0	1.73546377	0.928	0.304	0	Basal	Fxyd3
8	0	1.67362794	0.522	0.15	0	Basal	Serpinb2
9	0	1.52298097	0.766	0.29	0	Basal	Cxcl14
10	0	1.46903532	0.834	0.647	0	Basal	Atf3
11	0	1.46502226	0.638	0.389	0	Basal	Thbs1
12	0	1.38388261	0.998	0.594	0	Basal	Lgals7
13	0	1.38381233	0.493	0.048	0	Basal	Fcgbp
14	0	1.28688625	0.789	0.529	0	Basal	Dnajb1
15	0	1.26863228	0.995	0.851	0	Basal	Apoe
16	0	1.25775674	0.353	0.072	0	Basal	Ifi202b
17	0	1.2450638	0.663	0.274	0	Basal	Krt17
18	0	1.24197868	0.913	0.697	0	Basal	Mt2
19	0	1.23138487	0.931	0.597	0	Basal	Hspb1
20	0	1.21728973	0.929	0.651	0	Basal	Sdc4
21	0	1.21115222	0.51	0.159	0	Basal	Plet1
22	0	1.2102919	0.704	0.173	0	Basal	Urah
23	0	1.19300757	0.973	0.461	0	Basal	Perp
24	0	1.15119506	0.659	0.248	0	Basal	Ly6d
25	0	1.1017418	0.586	0.243	0	Basal	Avpi1

Supplementary Table 20							
Top 30 differentially expressed genes for each cell type that are depicted in the UMAP plot in Fig 2C							
	p_val	avg_log2FC	pct.1	pct.2	p_val_adj	cluster	gene
Vcan	0	1.55830516	0.954	0.643	0	BcaPfl_enriched_tumor	Vcan
Hspa1a	0	1.38330174	0.806	0.712	0	BcaPfl_enriched_tumor	Hspa1a
Itga1	0	1.27292618	0.967	0.727	0	BcaPfl_enriched_tumor	Itga2
Klf6	0	1.14857107	0.974	0.895	0	BcaPfl_enriched_tumor	Klf7
Has2	0	1.09052216	0.509	0.095	0	BcaPfl_enriched_tumor	Has3
Itga8	0	1.06935965	0.642	0.285	0	BcaPfl_enriched_tumor	Itga9
Col20a1	0	1.06708456	0.979	0.709	0	BcaPfl_enriched_tumor	Col20a2
Hsph1	0	1.06645114	0.74	0.489	0	BcaPfl_enriched_tumor	Hsph2
Tnfaip6	0	1.04037205	0.862	0.525	0	BcaPfl_enriched_tumor	Tnfaip7
Hspa1b	0	1.04015575	0.772	0.732	0	BcaPfl_enriched_tumor	Hspa1b
Creb5	0	1.0247889	0.925	0.755	0	BcaPfl_enriched_tumor	Creb6
Nfkbiz	0	1.02466704	0.805	0.627	0	BcaPfl_enriched_tumor	Nfkbiz
Fosb	0	1.01939571	0.947	0.791	0	BcaPfl_enriched_tumor	Fosb
Cpm	0	1.01835576	0.43	0.066	0	BcaPfl_enriched_tumor	Cpm
Col4a1	0	0.97544624	0.987	0.804	0	BcaPfl_enriched_tumor	Col4a2
Igsf9b	0	0.96470078	0.696	0.293	0	BcaPfl_enriched_tumor	Igsf9b
Sema6d	0	0.96320988	0.835	0.571	0	BcaPfl_enriched_tumor	Sema6d
Col4a2	0	0.95708163	0.968	0.752	0	BcaPfl_enriched_tumor	Col4a3
Ccn1	0	0.94161207	0.763	0.61	0	BcaPfl_enriched_tumor	Ccn2
Spry2	0	0.93949624	0.869	0.651	0	BcaPfl_enriched_tumor	Spry3
Serpine2	0	0.93506658	0.993	0.776	0	BcaPfl_enriched_tumor	Serpine3
S1pr3	0	0.92725347	0.635	0.256	0	BcaPfl_enriched_tumor	S1pr4
Rab27b	0	0.92708123	0.556	0.067	0	BcaPfl_enriched_tumor	Rab27b
Ptprz1	0	0.92487322	0.977	0.749	0	BcaPfl_enriched_tumor	Ptprz2
Armh4	0	0.92083962	0.79	0.446	0	BcaPfl_enriched_tumor	Armh5
Thbs2	0	0.91128758	0.745	0.424	0	BcaPfl_enriched_tumor	Thbs3
Jun	0	0.90866129	0.961	0.906	0	BcaPfl_enriched_tumor	Jul

Supplementary Table 21						
Top 30 Differentially expressed genes for each cell type that are depicted in the UMAP plot in Fig 3D						
p_val	avg_log2FC	pct.1	pct.2	p_val_adj	cluster	gene
0	3.68293596	0.752	0.301	0	Immune	Cd74
0	3.28166638	0.87	0.309	0	Immune	Lyz2
0	3.19616742	0.685	0.35	0	Immune	Ccl8
0	3.07951229	0.568	0.172	0	Immune	H2-Aa
0	2.97850778	0.72	0.216	0	Immune	C1qa
0	2.96516586	0.532	0.14	0	Immune	H2-Ab1
0	2.76619879	0.501	0.099	0	Immune	H2-Eb1
0	2.75662828	0.793	0.251	0	Immune	Wfdc17
0	2.68998349	0.683	0.17	0	Immune	C1qb
0	2.62303192	0.879	0.178	0	Immune	Fcer1g
0	2.54836579	0.913	0.822	0	Immune	Apoe
0	2.48548645	0.865	0.156	0	Immune	Tyrobp
0	2.39040309	0.624	0.09	0	Immune	C1qc
0	2.38726993	0.805	0.353	0	Immune	Ifi27l2a
0	2.36359081	0.783	0.163	0	Immune	Srgn
0	2.35482562	0.636	0.09	0	Immune	Ccl6
0	2.30462643	0.774	0.096	0	Immune	Ctss
0	2.1407552	0.545	0.306	0	Immune	Cxcl2
0	2.09899883	0.616	0.061	0	Immune	Cd52
0	2.07982795	0.481	0.072	0	Immune	Pf4
0	2.03565297	0.342	0.046	0	Immune	Il1b
0	2.02337836	0.596	0.07	0	Immune	Mrc1
0	1.91776951	0.816	0.154	0	Immune	Laptm5
0	1.91085666	0.582	0.058	0	Immune	Cd14
0	1.88118974	0.346	0.047	0	Immune	Ccl4

Supplementary Table 22			
Euclidean distances calculated between NC-derived cell clusters (35, 527 cells from Fig 2B) using the average embeddings from the top 10 Principal Components (PCs) (Fig S3F)			
LNM cell vs. Principal Tumor			
	colMeans(pca_LNM)	colMeans(pca_principalTumor)	distance
PC_1	-2.58	-10.67	65.37
PC_2	-45.87	4.85	2572.26
PC_3	22.91	0.92	483.38
PC_4	-4.16	1.01	26.76
PC_5	-0.60	0.21	0.66
PC_6	-1.14	-0.05	1.20
PC_7	0.81	-0.42	1.51
PC_8	1.06	0.09	0.94
PC_9	2.07	0.79	1.63
PC_10	0.71	0.08	0.39
sum			3154.10
sqrt of sum			**56.16**

LNM cell vs. Melanocyte			
	colMeans(pca_LNM)	colMeans(pca_melanocyte)	distance
PC_1	-2.58	43.21	2096.62
PC_2	-45.87	-2.01	1923.98
PC_3	22.91	-5.25	792.95
PC_4	-4.16	0.46	21.38
PC_5	-0.60	4.97	31.04
PC_6	-1.14	1.02	4.68
PC_7	0.81	1.01	0.04

Supplementary Table 23				
Euclidean distances calculated between NC-derived clusters (32,611 cells from transplanted and parental tumors in Fig 3B) using the average embeddings from the top 30 Harmony space (Fig S6D)				
Embedding Centroids (Harmony space)				
	Tumor	LNM2	Melanocyte	LNM1
harmony_1	-5.755839279	8.180652719	5.87739392	0.436564532
harmony_2	2.226402232	-5.476176899	-14.39018371	-5.543085716
harmony_3	-2.887676999	-0.613538611	-5.123973875	-2.730824944
harmony_4	0.141775937	0.546186212	-1.847632548	1.659375824
harmony_5	-0.255361815	1.664692829	-3.212048256	13.00981173
harmony_6	0.096196295	-0.108621786	3.036570616	-0.593386843
harmony_7	0.361885451	-0.894919676	-0.386151494	8.627403551
harmony_8	0.676817334	-0.081596037	0.999704596	4.247580459
harmony_9	-0.670831765	0.948857014	0.807088046	3.394573222
harmony_10	0.289079563	-0.259543024	0.798021103	-1.915939894
harmony_11	-0.544771647	-0.590416628	-1.734143501	-1.642440188
harmony_12	-0.08910151	-0.261483926	-0.266779027	1.261061911
harmony_13	0.41678401	-0.412440712	-0.023845174	0.205696272
harmony_14	0.453944502	-0.233885409	0.309603848	0.659882819
harmony_15	0.235973037	-0.673559911	-0.42726117	1.249569661
harmony_16	-0.20274014	0.222389094	0.193447486	0.285156247
harmony_17	0.287674367	0.567034465	0.283870778	-0.158045345
harmony_18	0.306077516	0.439961751	0.505390579	-0.300685401
harmony_19	-0.078504653	0.402364209	0.449058705	-0.00753465
harmony_20	0.280988274	0.245196582	-0.1822045	0.107108357
harmony_21	-0.074540132	0.048320482	0.781180901	0.829998937
harmony_22	0.234008968	0.113517714	0.200900674	0.91715802

Supplementary Table 24						
Gene signature sets used for determining the comparative "membership scores" in Fig 4						
Human Biopsy (Pozniak et al. 2022)						
Mesenchymal-like signature	NC-like signature	Antigen-presentation signature	IFN alpha beta response signature	Mitochondiral signature	Stress signature	Melanocytic signature
Pdgfrb	St8sia5	H2-Ea	Dpp6	Mgp	Vegfa	Rps7
Nrp1	Dcstamp	Gbp2b	Pkhd1	Apoe	Ndufa4l2	Rps18
Filip1l	Col8a1	H2-Eb1	Pcsk2	mt-Atp8	Flnb	Rps23
Col5a1	Ngfr	H2-Aa	Ifit1	mt-Nd6	Nxph4	Rpl7a
Col1a1	Axl	H2-DMa	Oas2	Dst	Slc16a3	Rpl12
Tshz2	Mrc2	H2-Ab1	Tfap2b	App	Eno2	Rps6
Col3a1	Bmp8b	Ciita	Ctxnd1	Pcdh7	Ak4	Rps13
Lum	Ece1	H2-DMb1	Apcdd1	Nfia	Pgk1	Rps14
Thy1	Ntm	Tap1	Lgi3	Kcnj10	P4ha1	Rps3
Tcf4	Tnc	Plaat4	Eif1ax	Rnase1	Igfbp5	Rpl41
Id3	Pmepa1	Psmb9	Angpt2	mt-Nd5	Adm	Rps15a
Pmepa1	Itgb8	Stat1	Mx1	Ptprz1	Pdk1	Rpl9
Mrc2	Col4a1	Il18bp	Slc1a4	Moxd1	Gstm5	Rps8
Tpbg	Slc20a1	Apol6	Ly6e	Ddx17	Aldoc	Rpl8
Dcn	Loxl3	B2m	Gng11	Nes	Pfkfb4	Naca
Col1a2	Olfml3	Gbp3	Isg15	Gm8091	Gapdh	Rpl32l
Col4a1	Col5a2	Gbp2	Ifit3	Spp1	Bhlhe40	Rpl30
Mxra8	Itga3	Cd74	Oas1f	Tbx2	Angptl4	Rpl37
Tmem176a	Il1rap	Irf1	Ramp1	Xist	Eno1	Rpl6
Tmsb4x	Itih5	Wars1	Abhd2	Zeb2	Stxbp1	Rpl19
Col6a2	Igfbp3	Ifih1	Hr	mt-Nd4l	Slc2a1	Rpl35
Rarres2	Col12a1	Tapbp	Ifi27	Zbtb20	Spp1	Prl29

Supplementary Table 25				
Additional gene signature sets used to dtermine "membership scores" depicted in Fig S7E-G				
Top 125 genes were used for Hodis et al. datasets, and top 100 genes were used for Wouters 2020 dataset				
CRISPR-edited In-vivo (Hodis et al. 2022)				
Program 1 (Ribosomal)	***Program 2 (OxPhos)***	***Program 3 (Interferon/TGFb)***	***Program 4 (EMT)***	***Program 5 (beta-catenin/***
Fabp7	Ubb	Selenon	Loxl1	Ctnnb1
Eef1a1	Capg	Gal3st1	Tgfbi	Nbl1
Bcan	Gstp1	Vat1l	Dcbld2	mt-Nd1
Apoe	Ctsl	Gpc1	Rcan1	Guk1
Rpl23a	Pmel	Frem2	Meg3	Mif
Gng7	Rab38	Col22a1	Cnn1	Rps7
Rps4x	Igfbp7	Ank	Slc9a3r2	Bri3
Rbp7	Fdps	Aqp1	Kcnma1	mt-Co1
Cirbp	Skp1a	Sdc3	Ptges	Prl29
Rps24	Gsto1	Slc20a1	Rtn1	Mitf
Spp1	Paep	Lama4	Lmo4	Scd1
Tpt1	Qpct	Dag1	Tagln	Prkd3
Fxyd1	Tpi1	Pcdh9	Pmepa1	Rps2
Serpinf1	Nqo1	Thbs2	Tagln2	Myo5a
Naca	Mgst3	Slco1b2	Pdlim7	Tdrd3
Dbi	Prdx2	Mpz	Dbndd1	Trpm1
Hhatl	Prdx1	Rbp1	Myl9	Zc3h13
Rpl7	Cd63	Olfml3	Col1a2	Sema5a
Rpl23	Actb	Mt2	Scx	Ttyh3
Rpl24	Anxa5	Cdh19	Col1a1	Yjefn3
Uqcrb	Psma7	Slc5a3	Tuba1a	Nme4
Pfdn5	Atp5b	Dcstamp	Crabp1	Slc7a5

	Supplementary Table 26						
velocity analysis of three individual tumors using the software scvelo, shown in Fig 5B-D							
tumor	Black BrafCA/+ PtenΔ/+ Tumor (S92)			Serially Transplanted Tumor #1 (S113)			Serially Transplanted T
cell-type	Tumor	Tumor(prolif)	LNM	tumor	LNM	tumor(prolif)	LNM
	Fosb	Mis18bp1	St8sia6	Stk32a	S100a6	Atp8a1	Hmga2
	Col20a1	Kif11	Fosb	Tcf4	Tes	Cdh19	Glipr1
	Rab27b	Fosb	Col20a1	Ptprz1	Lgals1	Itih5	Dync1i2
	Scn7a	Col20a1	Kcnq3	Itih5	Pde3b	Sox6	Sec62
	Actb	Mki67	Col13a1	Sox6	Pam	Adam23	Cp
	Itih5	Top2a	Ablim3	Atp8a1	Rai14	Ptprz1	Ndufv3
	Sbno2	Cdk1	Cavin2	Itga1	Zbtb20	Slc35f1	Klra4
	Baz1b	Prr11	Tnfrsf23	Chl1	Flnb	Pde8a	S100a6
	Ccnl1	Shcbp1	Scn7a	Slc35f1	Hmga2	Qk	Snrpd1
	Abl2	Scn7a	Rab27b	Moxd1	Zfand5	Zfp536	S100a10
	Hsph1	Pbk	Sbno2	Gulp1	P4ha1	Itga1	Rbp1
	Vgll3	Iqgap3	Ppl	Sorbs1	Sqstm1	Sorbs1	S100a11
	Ifrd1	Knl1	Frem2	Gpm6b	Alcam	Stk32a	AA467197
	Itga8	Cep55	Palmd	Cdh19	Tcf4	Tcf4	Mrpl33
	Prkg1	Cenpe	Gpx1	Adam23	Peak1	Gulp1	Tbcb
	Tm4sf1	Kif15	Aqp1	Igfbp7	Aig1	Ptpn13	Csrp2
	Nrp1	Itga8	Medag	Il1rap	Celf2	Igfbp7	H2afj
	Pak3	Stil	Hs3st3b1	Tmtc2	Cpe	Chl1	Pdgfra
	Gap43	Cdca3	Npy	Gas7	Eps8	Il1rap	Esd
	Lbh	Kif4	Baz1b	Zfp536	Anxa2	Mcam	Psma2
	Itga1	Ccnb2	Fam135b	Shc4	Prkcb	Ndst3	Cnih4
	Klf9	Cdca2	Nppb	Grb10	Fndc3a	Gas7	Sin3b
	Arl5a	Klf9	Osr2	Qk	Ackr3	Plpp1	Fam162a

Supplementary Table 27						
Differentially expressed gene (DEG) list from Mutrans transitional analysis of three tumors, shown in Fig 5E.. MetaState = stable sta						
Black *BrafCA/+ PtenΔ/+* Tumor (S92)					Serially Transplanted Tumor #1 (S1	
cluster 2		cluster 0			cluster 1	
LNM_metaState	LNM_hybrid	tumor_metaState	tumor_hybrid	transition-driver genes	LNM-metastate (	LNM-hybrid
Sept11	S100a6	Zfp287	Scara5	Kcnk13	ms1	Nmt2
Scd1	Tmsb4x	Rbl1	Stard8	Mxd3	S100a6	Ccng1
Col6a2	Lgals1	Hspa1b	Pcp4l1	Tmem196	Tmsb4x	Ctsd
Cav1	H2afj	Tmod2	Aqp1	Cacng5	Lgals1	Flnb
Igf1	Cycs	Gpc3	B2m	Fignl1	H2afj	Tes
Cav2	S100a11	Zfp703	Hmcn1	Serpind1	Cycs	Dcxr
Atp6v0e	Cd63	Hspa1a	Ckb	Mlip	S100a11	Podxl
Frem2	Cox7b	Ccnd2	Col13a1	Nrxn1	Cd63	Mmd
Sema3d	Nefl	Cadm3	Kctd1	Pif1	Cox7b	Crhbp
Wwc1	2200002D01Rik	Ednrb	Ctsd	Dtna	Nefl	Crabp2
Samd5	Anxa2	Chaf1a	Pkm	Tmprss5	2200002D01Rik	Btc
Chst11	Atp5l	Aldh1a1	Rapgef5	Cdc25c	Anxa2	Ghr
Nebl	Mif	Alms1	St8sia6	Rarb	Atp5l	Mt2
Gapdh	Pla2g7	Neb	6430548M08Rik	Neto1	Mif	Uchl1
Etv1	S100a10	Kcna1	Pgk1	Sfrp5	Pla2g7	Cacybp
Acly	1110008P14Rik	Col4a1	Ablim3	Slc6a15	S100a10	Nhp2
Tfap2b	Capg	Marcks	Lurap1l	Sorcs1	1110008P14Rik	Nrcam
Tnfrsf21	Timp1	Inava	Btbd3	Tmem26	Capg	A630023A22Rik
Moxd1	Lgals7	Abcb8	Rgs7bp	Nrap	Timp1	Sprr1a
Nes	Nppb	Scn7a	Aplp1	Nkain2	Lgals7	Clcf1
Sdc2	Igfbp3	Ccne1	Elovl5	eGFP	Nppb	Sec61b
Gpx1	Spp1	Klhl13	Gng12	Scn9a	Igfbp3	Rgs17

REFERENCES

1. Hodis E, et al. A landscape of driver mutations in melanoma. Cell 150, 251-263 (2012).

2. Huang FW, Hodis E, Xu MJ, Kryukov GV, Chin L, Garraway LA. Highly recurrent TERT promoter mutations in human melanoma. Science 339, 957-959 (2013).

3. Hayward NK, et al. Whole-genome landscapes of major melanoma subtypes. Nature 545, 175-180 (2017).

4. Shain AH, et al. The Genetic Evolution of Melanoma from Precursor Lesions. N Engl J Med 373, 1926-1936 (2015).

5. Davies H, et al. Mutations of the BRAF gene in human cancer. Nature 417, 949-954 (2002).

6. Kiuru M, et al. Improving classification of melanocytic nevi: Association of BRAF V600E expression with distinct histomorphologic features. J Am Acad Dermatol 79, 221-229 (2018).

7. Dankort D, et al. Braf(V600E) cooperates with Pten loss to induce metastatic melanoma. Nat Genet 41, 544-552 (2009).

8. Patton EE, et al. Melanoma models for the next generation of therapies. Cancer Cell 39, 610-631 (2021).

9. Dhomen N, et al. Oncogenic Braf induces melanocyte senescence and melanoma in mice. Cancer Cell 15, 294-303 (2009).

10. Gray-Schopfer VC, et al. Cellular senescence in naevi and immortalisation in melanoma: a role for p16? Br J Cancer 95, 496-505 (2006).

11. Peeper DS. Oncogene-induced senescence and melanoma: where do we stand? Pigment Cell Melanoma Res 24, 1107-1111 (2011).

12. Ruiz-Vega R, et al. Dynamics of nevus development implicate cell cooperation in the growth arrest of transformed melanocytes. Elife 9, (2020).

13. McNeal AS, et al. BRAF(V600E) induces reversible mitotic arrest in human melanocytes via microrna-mediated suppression of AURKB. Elife 10, (2021).

14. Rebecca VW, Somasundaram R, Herlyn M. Pre-clinical modeling of cutaneous melanoma. Nat Commun 11, 2858 (2020).

15. Koga Y, et al. Genome-wide screen of promoter methylation identifies novel markers in melanoma. Genome Res 19, 1462-1470 (2009).

16. Moran B, Silva R, Perry AS, Gallagher WM. Epigenetics of malignant melanoma. Semin Cancer Biol 51, 80-88 (2018).

17. Arozarena I, Wellbrock C. Phenotype plasticity as enabler of melanoma progression and therapy resistance. Nat Rev Cancer 19, 377-391 (2019).

18. Karras P, et al. A cellular hierarchy in melanoma uncouples growth and metastasis. Nature 610, 190-198 (2022).

19. Wouters J, et al. Robust gene expression programs underlie recurrent cell states and phenotype switching in melanoma. Nat Cell Biol 22, 986-998 (2020).

20. Shaffer SM, et al. Rare cell variability and drug-induced reprogramming as a mode of cancer drug resistance. Nature 546, 431-435 (2017).

21. Hugo W, et al. Non-genomic and Immune Evolution of Melanoma Acquiring MAPKi Resistance. Cell 162, 1271-1285 (2015).

22. Rambow F, et al. Toward Minimal Residual Disease-Directed Therapy in Melanoma. Cell 174, 843-855 e819 (2018).

23. Rambow F, Marine JC, Goding CR. Melanoma plasticity and phenotypic diversity: therapeutic barriers and opportunities. Genes Dev 33, 1295-1318 (2019).

24. Bosenberg M, et al. Characterization of melanocyte-specific inducible Cre recombinase transgenic mice. Genesis 44, 262-267 (2006).

25. Ruiz R, et al. The RhoJ-BAD signaling network: An Achilles' heel for BRAF mutant melanomas. PLoS Genet 13, e1006913 (2017).

26. Ochi S, et al. Pathological role of osteoclast costimulation in arthritis-induced bone loss. Proc Natl Acad Sci U S A 104, 11394-11399 (2007).

27. Viros A, et al. Ultraviolet radiation accelerates BRAF-driven melanomagenesis by targeting TP53. Nature 511, 478-482 (2014).

28. Bowman RL, et al. UVB mutagenesis differs in Nras- and Braf-mutant mouse models of melanoma. Life Sci Alliance 4, (2021).

29. Nakamura F, et al. Molecular basis of filamin A-FilGAP interaction and its impairment in congenital disorders associated with filamin A mutations. PLoS One 4, e4928 (2009).

30. Horn S, et al. TERT promoter mutations in familial and sporadic melanoma. Science 339, 959-961 (2013).

31. Khandekar A, et al. Visualizing and exploring patterns of large mutational events with SigProfilerMatrixGenerator. bioRxiv, (2023).

32. Fan X, Abbott TE, Larson D, Chen K. BreakDancer: Identification of Genomic Structural Variation from Paired-End Read Mapping. Curr Protoc Bioinformatics 45, 15 16 11-11 (2014).

33. Talevich E, Shain AH, Botton T, Bastian BC. CNVkit: Genome-Wide Copy Number Detection and Visualization from Targeted DNA Sequencing. PLoS Comput Biol 12, e1004873 (2016).

34. Gordeeva V, Sharova E, Babalyan K, Sultanov R, Govorun VM, Arapidi G. Benchmarking germline CNV calling tools from exome sequencing data. Sci Rep 11, 14416 (2021).

35. Rambow F, et al. New Functional Signatures for Understanding Melanoma Biology from Tumor Cell Lineage-Specific Analysis. Cell Rep 13, 840-853 (2015).

36. Colombo S, et al. Stabilization of beta-catenin promotes melanocyte specification at the expense of the Schwann cell lineage. Development 149, (2022).

37. Muzumdar MD, Tasic B, Miyamichi K, Li L, Luo L. A global double-fluorescent Cre reporter mouse. Genesis 45, 593-605 (2007).

38. Bennett DC, Lamoreux ML. The color loci of mice--a genetic century. Pigment Cell Res 16, 333-344 (2003).

39. Neubauer E, et al. Comparative evaluation of three proliferation markers, Ki-67, TOP2A, and RacGAP1, in bronchopulmonary neuroendocrine neoplasms: Issues and prospects. Oncotarget 7, 41959-41973 (2016).

40. Mo Y, et al. MicroRNA-329 upregulation impairs the HMGB2/beta-catenin pathway and regulates cell biological behaviors in melanoma. J Cell Physiol 234, 23518-23527 (2019).

41. Zhou H, Gao J, Lu ZY, Lu L, Dai W, Xu M. Role of c-Fos/JunD in protecting stress-induced cell death. Cell Prolif 40, 431-444 (2007).

42. Luo Y, et al. ALDH1A isozymes are markers of human melanoma stem cells and potential therapeutic targets. Stem Cells 30, 2100-2113 (2012).

43. Liu T, Zhou L, Li D, Andl T, Zhang Y. Cancer-Associated Fibroblasts Build and Secure the Tumor Microenvironment. Front Cell Dev Biol 7, 60 (2019).

44. Wang G, et al. Macrophagic Extracellular Vesicle CXCL2 Recruits and Activates the Neutrophil CXCR2/PKC/NOX4 Axis in Sepsis. J Immunol 207, 2118-2128 (2021).

45. Nair MG, et al. Alternatively activated macrophage-derived RELM-alpha is a negative regulator of type 2 inflammation in the lung. J Exp Med 206, 937-952 (2009).

46. Erickson A, et al. Spatially resolved clonal copy number alterations in benign and malignant tissue. Nature 608, 360-367 (2022).

47. Stables MJ, et al. Transcriptomic analyses of murine resolution-phase macrophages. Blood 118, e192-208 (2011).

48. Krepler C, et al. A Comprehensive Patient-Derived Xenograft Collection Representing the Heterogeneity of Melanoma. Cell Rep 21, 1953-1967 (2017).

49. Korsunsky I, et al. Fast, sensitive and accurate integration of single-cell data with Harmony. Nat Methods 16, 1289-1296 (2019).

50. Verkman AS. Aquaporin water channels and endothelial cell function. J Anat 200, 617-627 (2002).

51. Laga AC, Zhan Q, Weishaupt C, Ma J, Frank MH, Murphy GF. SOX2 and nestin expression in human melanoma: an immunohistochemical and experimental study. Exp Dermatol 20, 339-345 (2011).

52. Santini R, et al. SOX2 regulates self-renewal and tumorigenicity of human melanoma-initiating cells. Oncogene 33, 4697-4708 (2014).

53. Cesarini V, et al. Sox2 is not required for melanomagenesis, melanoma growth and melanoma metastasis in vivo. Oncogene 36, 4508-4515 (2017).

54. Schaefer SM, et al. Sox2 is dispensable for primary melanoma and metastasis formation. Oncogene 36, 4516-4524 (2017).

55. Pozniak J, et al. A TCF4-dependent gene regulatory network confers resistance to immunotherapy in melanoma. Cell 187, 166-183 e125 (2024).

56. Hodis E, et al. Stepwise-edited, human melanoma models reveal mutations' effect on tumor and microenvironment. Science 376, eabi8175 (2022).

57. Mitra D, et al. An ultraviolet-radiation-independent pathway to melanoma carcinogenesis in the red hair/fair skin background. Nature 491, 449-453 (2012).

58. Bergen V, Lange M, Peidli S, Wolf FA, Theis FJ. Generalizing RNA velocity to transient cell states through dynamical modeling. Nat Biotechnol 38, 1408-1414 (2020).

59. Zhou P, Wang S, Li T, Nie Q. Dissecting transition cells from single-cell transcriptome data through multiscale stochastic dynamics. Nat Commun 12, 5609 (2021).

60. Tang J, et al. The genomic landscapes of individual melanocytes from human skin. Nature 586, 600-605 (2020).

61. Martincorena I, et al. Tumor evolution. High burden and pervasive positive selection of somatic mutations in normal human skin. Science 348, 880-886 (2015).

62. Gong HZ, Zheng HY, Li J. Amelanotic melanoma. Melanoma Res 29, 221-230 (2019).

63. Iyengar B, Singh AV. Patterns of neural differentiation in melanomas. J Biomed Sci 17, 87 (2010).

64. Armitage P. Multistage models of carcinogenesis. Environ Health Perspect 63, 195-201 (1985).

65. Chernoff J. The two-hit theory hits 50. Mol Biol Cell 32, rt1 (2021).

66. Marin-Bejar O, et al. Evolutionary predictability of genetic versus nongenetic resistance to anticancer drugs in melanoma. Cancer Cell 39, 1135-1149 e1138 (2021).

67. Furlan A, Adameyko I. Schwann cell precursor: a neural crest cell in disguise? Dev Biol 444 Suppl 1, S25-S35 (2018).

68. Siegel RL, Miller KD, Jemal A. Cancer statistics, 2020. CA Cancer J Clin 70, 7-30 (2020).

69. Carrera C, Marghoob AA. Discriminating Nevi from Melanomas: Clues and Pitfalls. Dermatol Clin 34, 395-409 (2016).

70. Bauer J, Bastian BC. Distinguishing melanocytic nevi from melanoma by DNA copy number changes: comparative genomic hybridization as a research and diagnostic tool. Dermatol Ther 19, 40-49 (2006).

71. Bolger AM, Lohse M, Usadel B. Trimmomatic: a flexible trimmer for Illumina sequence data. Bioinformatics 30, 2114-2120 (2014).

72. Li H, Durbin R. Fast and accurate short read alignment with Burrows-Wheeler transform. Bioinformatics 25, 1754-1760 (2009).

73. Cibulskis K, et al. Sensitive detection of somatic point mutations in impure and heterogeneous cancer samples. Nat Biotechnol 31, 213-219 (2013).

74. Danecek P, et al. Twelve years of SAMtools and BCFtools. Gigascience 10, (2021).

75. Tattini L, D'Aurizio R, Magi A. Detection of Genomic Structural Variants from Next-Generation Sequencing Data. Front Bioeng Biotechnol 3, 92 (2015).

76. Stuart T, et al. Comprehensive Integration of Single-Cell Data. Cell 177, 1888-1902 e1821 (2019).

77. Fischer AH, Jacobson KA, Rose J, Zeller R. Hematoxylin and eosin staining of tissue and cell sections. CSH Protoc 2008, pdb prot4986 (2008).

78. Wang F, et al. RNAscope: a novel in situ RNA analysis platform for formalin-fixed, paraffin-embedded tissues. J Mol Diagn 14, 22-29 (2012).

79. Silkwood K, Dollinger E, Gervin J, Atwood S, Nie Q, Lander AD. Leveraging gene correlations in single cell transcriptomic data. BMC Bioinformatics (2023).

CHAPTER 3:

Summary, Future Directions, and Conclusions

Karen Hui Xiao, Jessica Shiu, Sahil S. Telang, Chi-Fen Chen, Anand K. Ganesan

Summary

In our study, we first demonstrate that *Braf* mutation alone is sufficient to generate tumors, in the albino background, without needing a secondary mutation. Tumors can also be formed by having a heterozygous mutation in the *Pten* tumor suppressor gene. Given this observation, we propose an alternative pathway for melanoma development—via a transitional state. Using these minimally mutated mouse models, we identified a Lowly pigmented, Neural, and Matrix-enriched (LNM) state in the Neural Crest (NC)-derived lineage, which serves as a potential intermediate step toward tumor formation. We found that LNM cells are present in wild-type skin but are significantly expanded in *Braf*-mutant skin. Moreover, LNM cells persisted when *Braf* -mutant tumors were transplanted, suggesting that this population is selectively maintained and plays a critical role in melanoma tumorigenesis. If this transitional state indeed acts as a pre-malignant marker, it could provide a new therapeutic target by preventing its formation, offering an alternative to the traditional targeted-therapy melanoma treatment. While this study establishes the significance of the LNM population, the underlying signaling networks regulating this state remain unclear. Unraveling these mechanisms will be a promising future direction.

Future Directions

Our transplantation experiments established an efficient and practical approach to study tumorigenesis, as tumor-promoting or tumor-initiating cell populations are likely selected during the passaging process, as transplantation efficiency increased with successive passage. While we established that tumors can be successfully transplanted into immunocompromised NSG mice, whether the host immune system influences transplantation efficiency is still not yet clear. To answer this question, we conducted additional transplantations using various donor tumor genotypes and recipient types, including NSG mice (albino coat color), black C57Bl/6, and albino C57Bl/6 mice.

We have so far transplanted tumors from black *Braf*$^{CA/+}$ *Pten*$^{\Delta/+}$ albino *Braf*$^{CA/+}$ *Pten*$^{\Delta/+}$ and albino *Braf*$^{CA/+}$ mice onto the flanks of both black and albino (congenic) C57/Bl6 mice, as well as immune-deficient NSG mice (which are also albino). The results of 95 transplantation experiments are summarized in Figure 3.1. Engraftment efficiency, defined as the fraction of transplants in which tumors successfully grew, ranged from 23% to 100% depending on the donor and host genotypes.

Notably, all donor genotypes showed 100% engraftment efficiency in NSG hosts. However, in immune-competent wildtype mice, efficiency was lower and showed significant difference between black and albino hosts. This difference was particularly notable for tumors from albino *Braf*$^{CA/+}$ donors, which engrafted more than twice as efficiently into albino hosts compared to black hosts (Fig 3.1). These findings indicate that variations in tumor incidence between black and albino skin may be primarily influenced by the recipient host environment, rather than solely by the cell-intrinsic effects of pigmentation in the donor tumor cells.

However, whether the environment fully explains this difference remains unclear. Notably, within the same host genotype, albino *Braf*$^{CA/+}$ *Pten*$^{\Delta/+}$ tumors demonstrate higher engraftment efficiency compared to black *Braf*$^{CA/+}$ *Pten*$^{\Delta/+}$ tumors ($p < 0.005$ in black hosts; $p = 0.16$ in albino hosts, Fig 3.1). This suggests that cell-intrinsic factors from donor tumors may contribute to engraftment differences. However, distinguishing these intrinsic effects from environmental influences is complicated by the fact that transplanted tumor cells carry donor-derived environmental cells, potentially confounding the interpretation of host-tumor microenvironment interactions. These complications trigger more compelling questions regarding melanoma tumor initiation: What sub-population in the immune system is affecting the tumor formation? What is the signaling network in the TME contributing to tumorigenesis? Answering these questions will help recapitulate the essential melanoma networks.

To examine the immune system in the TME more closely, we further examined our scRNA-seq data containing tumors, wildtype skin and nearby skin. Among the immune populations, we did not identify any significant increase in T cell enriched in the tumor samples, but macrophages enriched in tumor samples (Fig. 2.7B, 2.10B). Macrophages, particularly tumor-associated macrophages (TAMs), exhibit significant plasticity in melanoma, adopting either pro-inflammatory M1-like or immunosuppressive M2-like phenotypes[1]. More specifically, M1-like macrophages contribute to anti-tumor immunity by producing cytokines such as TNF-α and IL-12, enhancing T-cell responses[1]. Conversely, M2-like TAMs promote tumor progression by secreting anti-inflammatory cytokines like IL-10 and TGF-β, supporting angiogenesis, and suppressing immune responses[1].

In our data, tumor-associated macrophages (TAMs) consist of at least two distinct types: one exhibiting an M1-like signature with markers linked to tumor suppression, such as *Tnf*, and another characterized by the expression of the receptors *Cx3cr1*. (Fig. 2.10B, 3.2B). Next, we carried out preliminary experiments highlighting the involvement of the innate immune system in tumorigenesis. More specifically, in $Braf^{CA/+}$ $Pten^{\Delta/+}$ melanoma models, inhibition of macrophage function using clodronate liposomes led to a significant increase in tumor incidence and growth rate, indicating depleting tissue macrophages inhibit tumor formation(Fig. 3.2A).

CX3CR1, a chemokine receptor, plays a dual role in melanoma by influencing both tumor progression and immune response within the tumor microenvironment. In melanoma cells, *CX3CR1* facilitates metastasis by interacting with its ligand *CX3CL1*, guiding cancer cells to *CX3CL1*-rich sites and promoting tumor spread[2].In immune cells, particularly $CD8^+$ T cells, varying levels of *CX3CR1* expression define different functional states, with *CX3CR1*-high cells displaying strong cytolytic activity but reduced proliferative capacity [3]. Higher *CX3CR1* expression in $CD8^+$ T cells has also been associated with improved responses to PD-1 blockade immunotherapy, suggesting its role in enhancing anti-tumor immunity [4]. Additionally, the

CX3CL1-CX3CR1 axis recruits M2-like macrophages, contributing to an immunosuppressive environment that supports tumor growth[5].

Building on previous studies, we first investigated whether the *Cx3cl1-Cx3cr1* signaling axis is present within our minimally mutated mouse melanoma signaling networks. Feature plots of scRNA-seq data revealed that the ligand *Cx3cl1* is predominantly expressed in cancer-associated fibroblasts (CAFs), while its receptor *Cx3cr1* is highly expressed in tumor-associated macrophages (TAMs) (Fig. 3.2B). This ligand-receptor interaction between *Cx3cl1*-positive CAFs and *Cx3cr1*-positive TAMs was further confirmed using the bioinformatics pipeline CellChat[6], a computational tool designed to infer and analyze intercellular communication networks from single-cell transcriptomic data (Fig. 3.2C). Having validated the presence of this axis in our dataset, we next aimed to determine whether this pathway plays a critical role in reprogramming the tumor microenvironment (TME) during melanoma initiation, given that this axis may play an important role for a paracrine, stromal-macrophage axis in the immune regulation of our tumors.

To study this, we next injected the rapidly growing *Braf*$^{CA/+}$*; Pten*$^{\Delta/+}$ *Cdkn2a*$^{\Delta/\Delta}$ melanoma cells *YUMM1.7*[7], which harbor multiple mutations and consistently generate reproducible tumors, into *Cx3cr1* knockout mice. Tumors in *Cx3cr1*$^{\Delta/\Delta}$ mice grew significantly slower compared to those in wild-type controls (Fig. 3.2D). In contrast, *Cx3cr1*$^{\Delta/+}$ heterozygous knockout mice exhibited tumor growth patterns similar to wild-type mice, suggesting a dose-dependent effect of *Cx3cr1*. These findings indicate that *Cx3cr1*+ macrophages contribute to tumor progression, compared to the previously described clodronate macrophage depletion experiment that promoted tumor growth. These two experimental results also suggest that distinct macrophage populations within the tumor microenvironment may have opposing roles in regulating tumor growth.

For future directions, we plan to perform the same tumor injection experiments in *Cx3cl1* knockout mice to determine whether disrupting the *Cx3cl1-Cx3cr1* ligand-receptor interaction affects the tumor formation process. Through this approach, we aim to clarify the role of this signaling axis and the impact of diverse macrophage populations in reprogramming the TME during melanoma tumorigenesis.

Conclusions

Melanoma tumorigenesis is a complex process involving diverse cell states, transitions, and cell types. More importantly, these complex processes might differ in different melanoma types, such as the fast-growing pigmented ones with multiple mutations in other studies and the slow-growing hypomelanotic ones with minimal mutations in our study[8-9] (Fig. 2.16). With the minimally mutated models, we uncovered only a small part of this mechanism by focusing specifically on the neural crest-derived population and the immune compartment. First, we identified the LNM cell state within the neural crest-derived lineage, which may serve as a precursor state to tumor cells (Fig. 2.16). Secondly, we then demonstrated that macrophages play diverse roles in shaping the TME: in one case pro-tumor growth, and the other case anti-tumor growth (Fig 3.1, 3.2). Despite these findings, many aspects of melanoma TME signaling networks remain unexplored, representing key future directions for the study.

On the other hand, tumor formation can be affected by both genetic and non-genetic factors[10]. Genetically, cancer develops when mutations in oncogenes or tumor suppressor genes drive the formation, proliferation, and metastasis of cancer cells. In melanoma, the traditional paradigm posits that multiple mutations, acquired in a sequential manner, are necessary for tumor formation[11]. For instance, Shain et al. showed that the *BRAF* oncogene mutation, commonly found in benign nevus lesions, is insufficient alone to induce melanoma[11]. Instead, a second mutation in other driver genes is thought to be required for tumorigenesis[12]. However, the necessity of a secondary mutation remains uncertain. Given that mutations are irreversible, this

model suggests that melanoma prevention would depend solely on stopping initial driver mutations, severely limiting clinical treatment options.

Here, based on our study, we propose an alternative route for the development of *Braf*-mutant melanocytes into *Braf*-mutant melanoma—one that does not rely solely on genetic mutations. Instead, we suggest that a non-genetic pathway may facilitate this tumorigenic transition, potentially modulated by factors such as the immune system (Fig. 3.3). If we can further elucidate the essential signaling networks governing these non-genetic transitions, it may open new avenues for alternative clinical treatments, ultimately expanding the hope for a definitive cure for melanoma.

MATERIALS AND METHODS

Reagent type/resource	Designation	Source or reference	Identifiers	Additional information
Cell line	YUMM1.7	ATCC	CRL-3362	
Software	CellChat	Jin et al., 2021	RRID:SCR_021946	
Mouse strain	*CX$_3$CR-1* ^{GFP} KI/KO	The Jackson Laboratory	005582	Genetic Background: 000664 C57BL/6J
Mouse strain	C57Bl/6	The Jackson Laboratory	000664	

Congenic Tumor Transplantation

The tumor transplantation procedure in this chapter followed the same methodology as described in Chapter 2, including tumor collection, preparation, transplantation, and post-surgical care. Briefly, tumors from melanoma-bearing donor mice were excised, prepared in a sterile environment, and transplanted into recipient mice using a Matrigel-assisted implantation method. Mice were monitored for tumor growth, and transplantation shams were included as

controls. A total of 95 recipient mice were transplanted with tumors from three donor genotypes, including Albino *Braf* $^{CA/+}$, Black *Braf* $^{CA/+}$*; Pten*$^{\Delta/+}$, and Albino *Braf* $^{CA/+}$*; Pten*$^{\Delta/+}$. Each donor genotype was transplanted into black C57Bl/6, albino C57Bl/6, and NSG recipients. Specifically, tumors from Albino *Braf* $^{CA/+}$ donors were transplanted into 10 black C57Bl/6, 12 albino C57Bl/6, and 10 NSG mice. Tumors from Black *Braf* $^{CA/+}$*; Pten*$^{\Delta/+}$ donors were transplanted into 13 black C57Bl/6, 13 albino C57Bl/6, and 14 NSG mice. Tumors from Albino *Braf* $^{CA/+}$*; Pten*$^{\Delta/+}$ donors were transplanted into 10 black C57Bl/6, 10 albino C57Bl/6, and 3 NSG mice.

Ligand-receptor Interaction Analysis using CellChat

To investigate the ligand-receptor relationships in our scRNA-seq data, R package "CellChat"[6] (v1.1.3) was utilized, with annotated merged Seurat mouse tumor tissue object as input. CellChatDB.mouse was used. Signaling pathways were examined and visualized with netVisual_aggregate function.

***Cx3Cr1*^{GFP} KI/KO mouse model**

Cx3Cr1^{GFP} KI/KO mouse models around 8 weeks were purchased from JAX (005582) and were crossed with C57Bl/6 (JAX 000664) for *Cx3cr1*$^{\Delta/+}$ heterozygous models. All mouse protocols were conducted in accordance with IACUC guidelines.

YUMMM1.7 Tumor Cell Transplantation

YUMM1.7 mouse melanoma cell lines (*Braf* $^{CA/+}$ *Pten*$^{\Delta/\Delta}$ *Cdkn2a*$^{\Delta/\Delta}$) were purchased from ATCC (CRL-3362) and maintained in DMEM/F12 media supplemented with 10% FBS and 1% non-essential amino acids under standard conditions. Cells were trypsinized, washed twice with sterile 1× PBS, and counted using cell counter. After centrifugation at 1200 rpm for 5 minutes, cells were resuspended in sterile PBS for injection. Recipient mice were shaved with a razor at the injection site and anesthetized with Isoflurane. A suspension of 250,000 cells in 200 μL of sterile PBS was injected subcutaneously into the shaved flank using a 1000 μL insulin syringe.

200 μL of PBS was also transplanted into shaved flank as control. Mice were monitored regularly, and tumor size was measured three times per week. All mouse procedures were conducted in accordance with IACUC guidelines.

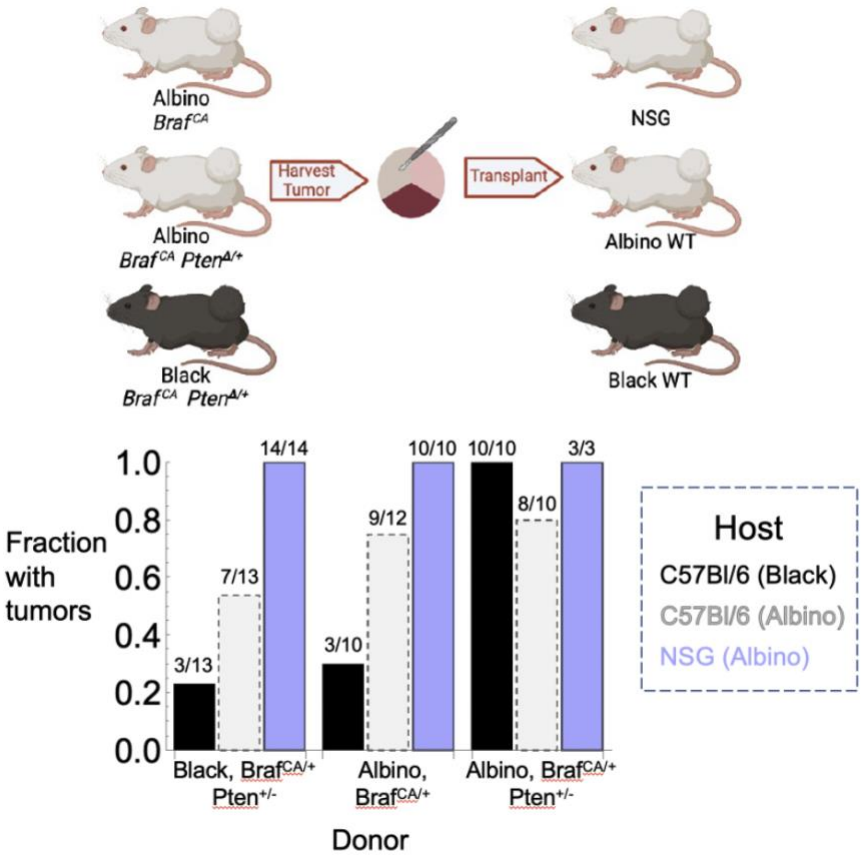
Albino
Braf^CA
NSG
Harvest Tumor
Transplant
Albino
Braf^CA Pten^Δ/+
Albino WT
Black
Braf^CA Pten^Δ/+
Black WT
Fraction with tumors
1.0
0.8
0.6
0.4
0.2
0.0
3/13
7/13
14/14
3/10
9/12
10/10
10/10
8/10
3/3
Black, Braf^CA/+ Pten^+/-
Albino, Braf^CA/+
Albino, Braf^CA/+ Pten^+/-
Donor
Host
C57Bl/6 (Black)
C57Bl/6 (Albino)
NSG (Albino)

Figure 3.1. Engraftment efficiency of tumors of different genotypes ("donor") into host mice of different pigment backgrounds or immune status. Tumors derived from *Braf* $^{CA/+}$and *Braf* $^{CA/+}$*; Pten* $^{\Delta/+}$ mouse models were passaged by xeno-transplantation onto C57/Bl6 and NSG (immune deficient) mice (n=95). Transplanted tumor counts and engraftment success rate are reported. Note that black mice are generally poorer hosts than white, while engraftment to NSG mice occurs at 100% efficiency.

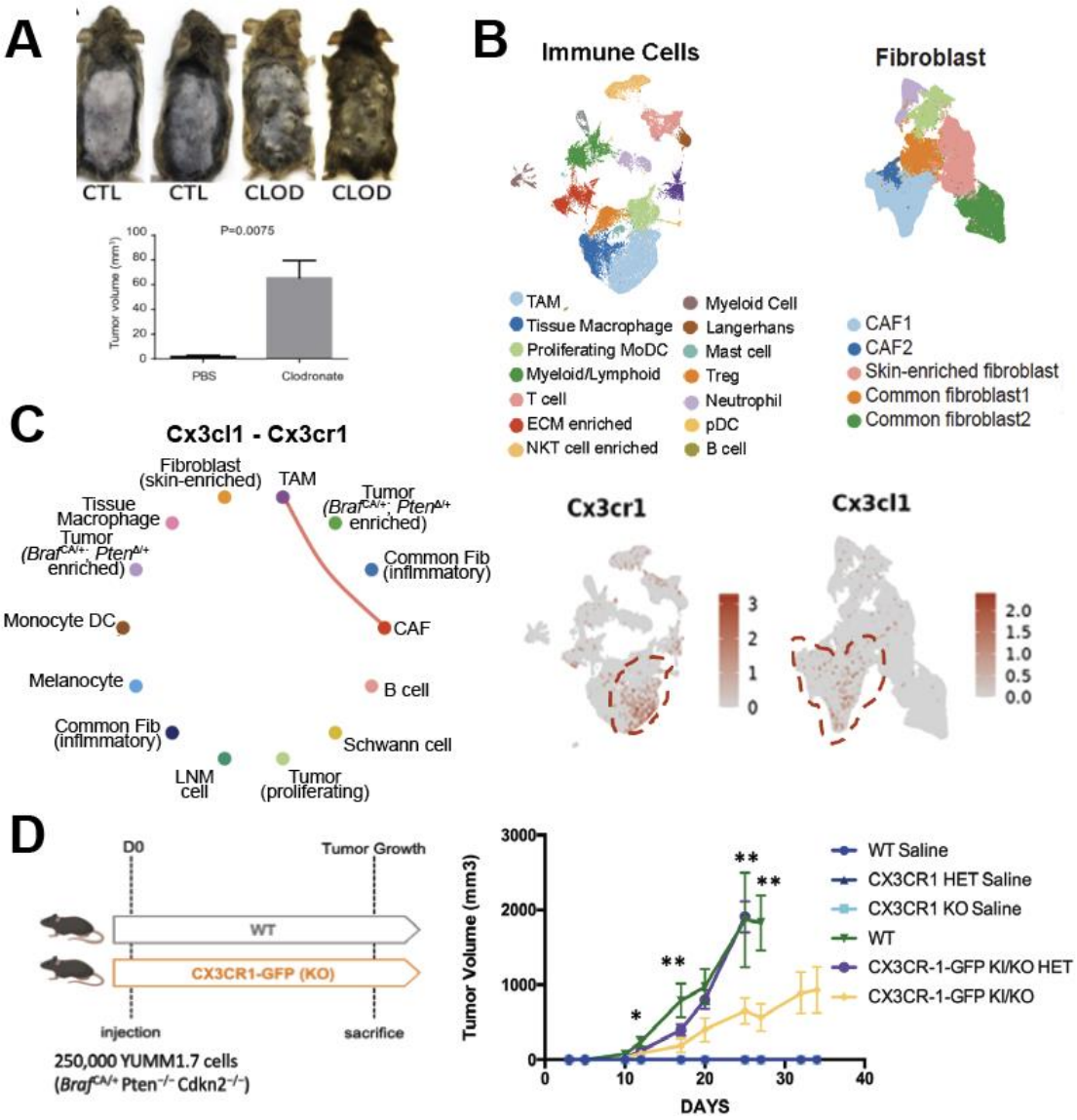
A
CTL
CTL
CLOD
CLOD
P=0.0075
Tumor volume (mm³)
PBS
Clodronate
B
Immune Cells
Fibroblast
TAM
Tissue Macrophage
Proliferating MoDC
Myeloid/Lymphoid
T cell
ECM enriched
NKT cell enriched
Myeloid Cell
Langerhans
Mast cell
Treg
Neutrophil
pDC
B cell
CAF1
CAF2
Skin-enriched fibroblast
Common fibroblast1
Common fibroblast2
C
Cx3cl1 - Cx3cr1
Fibroblast (skin-enriched)
TAM
Tissue Macrophage
Tumor (Braf CA/+; Pten Δ/+ enriched)
Tumor (Braf CA/+; Pten Δ/+ enriched)
Common Fib (inflmmatory)
CAF
Monocyte DC
Melanocyte
B cell
Common Fib (inflmmatory)
Schwann cell
LNM cell
Tumor (proliferating)
Cx3cr1
Cx3cl1
D
D0
Tumor Growth
WT
CX3CR1-GFP (KO)
injection
sacrifice
250,000 YUMM1.7 cells
(Braf CA/+ Pten -/- Cdkn2 -/-)
Tumor Volume (mm3)
DAYS
WT Saline
CX3CR1 HET Saline
CX3CR1 KO Saline
WT
CX3CR-1-GFP KI/KO HET
CX3CR-1-GFP KI/KO

Figure 3.2. Identification of a macrophage populations affecting tumor growth. A. Tissues macrophages suppress tumor growth. *Braf*^{CA} *Pten*$^{\Delta/+}$ mice treated with clodronate (+) to deplete tissue macrophages develop many more tumors than control (-) *Braf*^{CA} *Pten*$^{\Delta/+}$ mice. **B**. scRNA-seq of Immune and fibroblast subsets visualized in UMAP showing different sub-populations (top panel), with feature plots (bottom panel) showing that the ligand *Cx3cl1* is enriched in the cancer-associated fibroblast (CAF) while the receptor *Cx3cr1* is enriched in tumor-associated macrophage (TAM). **C.** The *Cx3cl1-Cx3cr1* ligand-receptor interaction between TAM and CAF identified by CellChat. **D.** *Cx3cr1*+ macrophages promote tumor growth. YUMM 1.7 cells were transplanted into wild type mice. Growth curves compare *Cx3cr1*-KO hosts with C57Bl/6 and sham-transplanted controls.

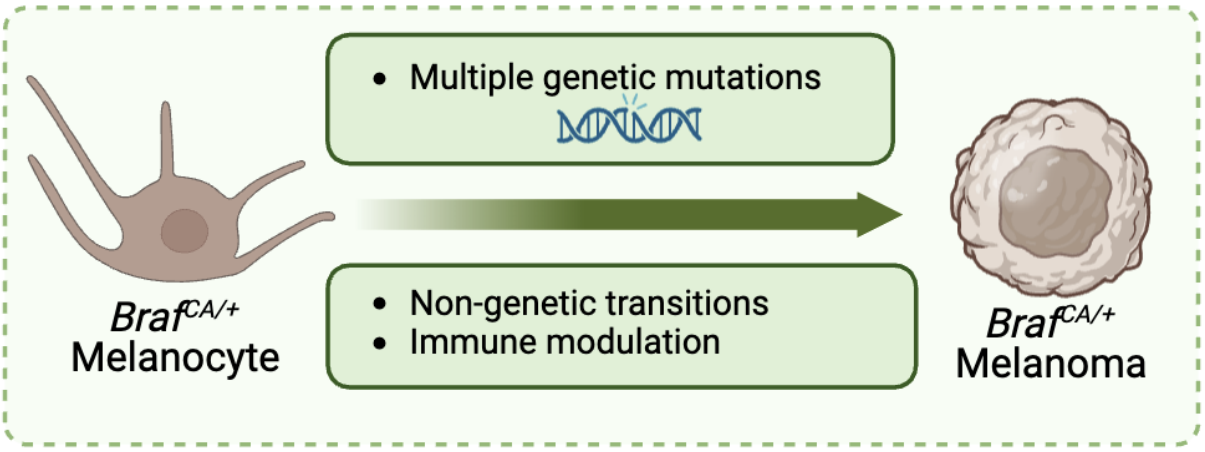
Multiple genetic mutations
Non-genetic transitions
Immune modulation
BrafCA/+
Melanocyte
BrafCA/+
Melanoma

Figure 3.3. Alternative proposed model of *Braf*$^{CA/+}$ melanocytes transitioning to *Braf*$^{CA/+}$ melanoma. While melanoma development can be driven by the accumulation of multiple genetic mutations, it can also be driven by non-genetic mechanisms—such as immune system modulation.

REFERENCES

1. Subhra K. Biswas, Antonio Sica, Claire E. Lewis; Plasticity of Macrophage Function during Tumor Progression: Regulation by Distinct Molecular Mechanisms[1]. *J Immunol* 15 February 2008; 180 (4): 2011–2017. https://doi.org/10.4049/jimmunol.180.4.2011

2. Chaudhri, A., Lizee, G., von Andrian, U. H., Hwu, P., & Freeman, G. J. (2023). *The CX3CL1-CX3CR1 chemokine axis can contribute to tumor immune evasion*. *Frontiers in Immunology*, 14, Article 1237715. https://doi.org/10.3389/fimmu.2023.1237715

3. Yamauchi, T., Hoki, T., Tabor, S. J., Dickson, M. A., Fan, L., Ramachandran, R., ... & Ito, F. (2020). *CX3CR1–CD8+ T cells are critical in antitumor efficacy but functionally suppressed in the tumor microenvironment*. *JCI Insight*, 5(8), e133920. https://doi.org/10.1172/jci.insight.133920

4. Yan, Y., Cao, S., Liu, X., Harrington, S. M., Bindeman, W. E., Adjei, A. A., ... & Dong, H. (2018). *CX3CR1 identifies PD-1 therapy–responsive CD8+ T cells that withstand chemotherapy during cancer chemoimmunotherapy*. *JCI Insight*, 3(8), e97828. https://doi.org/10.1172/jci.insight.97828

5. Ishida, Y., Kimura, A., Nosaka, M., Kuninaka, Y., Inui, M., Mukaida, N., & Kondo, T. (2020). *Pivotal involvement of the CX3CL1-CX3CR1 axis for the recruitment of M2 macrophages in skin carcinogenesis*. *Journal of Investigative Dermatology*, 140(10), 1951–1960.e6. https://doi.org/10.1016/j.jid.2020.02.011

6. Jin, S., Guerrero-Juarez, C. F., Zhang, L., Chang, I., Ramos, R., Kuan, C.-H., Myung, P., Plikus, M. V., & Nie, Q. (2021). Inference and analysis of cell-cell communication using CellChat. *Nature Communications*, 12, 1088. https://doi.org/10.1038/s41467-021-21246-

7. Meeth K, Wang JX, Micevic G, Damsky W, Bosenberg MW. The YUMM lines: a series of congenic mouse melanoma cell lines with defined genetic alterations. Pigment Cell & Melanoma Research. 2016 Sep;29(5):590-597. DOI: 10.1111/pcmr.12498. PMID: 27287723; PMCID: PMC5331933.

8. Dankort D*, et al*. Braf(V600E) cooperates with Pten loss to induce metastatic melanoma. *Nat Genet* **41**, 544-552 (2009).

9. Rebecca VW, Somasundaram R, Herlyn M. Pre-clinical modeling of cutaneous melanoma. *Nat Commun* **11**, 2858 (2020).

10. Laguillaumie, MO., Titah, S., Guillemette, A. *et al*. Deciphering genetic and nongenetic factors underlying tumour dormancy: insights from multiomics analysis of two syngeneic MRD models of melanoma and leukemia. *Biol Res* **57**, 59 (2024). https://doi.org/10.1186/s40659-024-00540-y

11. Osborne, C., Wilson, P., & Tripathy, D. (2004). Oncogenes and tumor suppressor genes in breast cancer: potential diagnostic and therapeutic applications. *The oncologist*, *9*(4), 361–377. https://doi.org/10.1634/theoncologist.9-4-361

12. Shain, A. H., Yeh, I., Kovalyshyn, I., Sriharan, A., Talevich, E., Gagnon, A., Dummer, R., North, J., Pincus, L., Ruben, B., Rickaby, W., D'Arrigo, C., Robson, A., & Bastian, B. C. (2015). The Genetic Evolution of Melanoma from Precursor Lesions. *The New England journal of medicine*, *373*(20), 1926–1936. https://doi.org/10.1056/NEJMoa1502583